ON ION PROBES AND TRAPS: BARIUM TAGGING FOR THE EXO DOUBLE BETA DECAY DETECTOR

A DISSERTATION
SUBMITTED TO THE DEPARTMENT OF PHYSICS
AND THE COMMITTEE ON GRADUATE STUDIES
OF STANFORD UNIVERSITY
IN PARTIAL FULFILLMENT OF THE REQUIREMENTS
FOR THE DEGREE OF
DOCTOR OF PHILOSOPHY

Matthew P. Green
June 2010

I certify that I have read this dissertation and that, in my opinion, it is fully adequate in scope and quality as a dissertation for the degree of Doctor of Philosophy.

Giorgio Gratta, Primary Adviser

I certify that I have read this dissertation and that, in my opinion, it is fully adequate in scope and quality as a dissertation for the degree of Doctor of Philosophy.

Mark Kasevich

I certify that I have read this dissertation and that, in my opinion, it is fully adequate in scope and quality as a dissertation for the degree of Doctor of Philosophy.

Ralph DeVoe

Approved for the Stanford University Committee on Graduate Studies.

Patricia J. Gumport, Vice Provost Graduate Education

Abstract

The Enriched Xenon Observatory seeks to measure neutrino mass through observation of neutrinoless double beta decay ($0\nu\beta\beta$). A new generation of ton-scale experiments are being developed, which aim to probe $0\nu\beta\beta$ half-lives on the order of 10^{27}–10^{28} years. The keys to reaching these sensitivities are large source mass and reduction of radioactive backgrounds; this thesis details efforts to develop a system for tagging the ^{136}Ba^{+} daughter of the double beta decay of ^{136}Xe, for the purposes of background elimination in a large experiment.

Acknowledgements

I'd like to thank all those with whom I've had lengthly discussions on the proper use of semicolons; without these essential punctuation marks this thesis could not have been written.

Contents

List of Tables

List of Figures

Chapter 1

Introduction

The last couple of decades have been a boon to the field of neutrino physics. Atmospheric neutrinos have been observed to undergo flavor mixing as they traverse the earth [12][13], the Solar Neutrino Problem has been solved [14][15], and oscillations of neutrinos emitted by nuclear reactors and neutrino beams have been verified [16][17], to name a few of the recent successes. Neutrino oscillation experiments have shown neutrinos to be massive particles, and provided measurements of the mass differences between the different mass eigenstates [18]. The absolute scale of the masses, however, remains unknown. The implications of a neutrino mass measurement would be far-reaching; these lightest fermions may provide much sought-after insight to new physics beyond the Standard Model. Limits on the mass scale have been set by kinematic measurements of nuclear β-decays [19] and observation of astrophysical phenomena [20], but neutrinoless double beta decay may prove to be the most sensitive probe of neutrino mass.

Neutrinoless double beta decay ($0\nu\beta\beta$) is an as yet unobserved second-order weak interaction. It's only allowed in the case that neutrinos are their own anti-particles, and has a decay amplitude proportional to an effective neutrino mass [21]. Studies of several candidate nuclei have so far yielded no widely accepted detection of $0\nu\beta\beta$, and as a result an effective mass upper limit of $m_\nu < 0.68$ eV has been set [2]. Mass splittings measured by neutrino oscillation experiments suggest $\mathrm{m}_\nu \leq 50$ meV to be an interesting scale, and several $0\nu\beta\beta$ experiments are currently being designed to push limits to this level [3].

The Enriched Xenon Observatory (EXO) is being designed to probe $0\nu\beta\beta$ in ^{136}Xe. As a source material ^{136}Xe has several advantageous properties, foremost amongst these being that the daughter atom of the double beta decay of ^{136}Xe, ^{136}Ba, can potentially be tagged using laser-induced fluorescence spectroscopy. By verifying the existence of a ^{136}Ba at the site of an observed candidate event, it would be possible to virtually eliminate background events in a ^{136}Xe-based neutrinoless double beta decay detector [22][23]. Several schemes which could potentially achieve this have been proposed. This dissertation details efforts to build an extraction probe and ion trap system, for the extraction, storage, and detection of a of a ^{136}Ba-ion daughter of the double beta decay of ^{136}Xe in a liquid Xenon time projection chamber.

Chapter 2 provides a discussion of the nature of neutrino mass and flavor mixing, $0\nu\beta\beta$ and its use as a probe of the absolute neutrino mass scale, and the status of current neutrino mass searches. Chapter 3 details the physics of ion storage in RF quadrupole traps, and Chapter 4 laser-induced fluorescence spectroscopy in the Ba^+ system. Chapters 5-6 describe experimental apparatus for the storage, manipulation, and detection of single Ba^+ ions for the purposes of background elimination in a ton-scale ^{136}Xe neutrinoless double beta decay experiment, and Chapter 7 details future prospects for the R&D program.

Chapter 2

Neutrino mass

The neutrino oscillation experiments of the past two decades have provided compelling evidence that neutrinos are indeed massive particles, and undergo flavor mixing not unlike that observed in the quark sector. While these oscillation experiments have probed the splittings between the different neutrino mass eigenstates, the absolute scale of the neutrino masses remains unknown. The search for neutrinoless double beta decay seeks to confirm the Majorana nature of neutrinos, and measure neutrino masses in a regime inaccessible to kinematic searches.

2.1 Majorana neutrinos

At present, the upper limit on the neutrino mass scale, as set by the Mainz and Troitsk β-spectrometers, is $\mathrm{m}_\nu \leq 2$ eV [19]. That this number is five orders of magnitude smaller than that of the next lightest fermion suggests that neutrino mass is derived from physics fundamentally different from that of the rest of the of the standard model fermions. Should neutrinos be found to be indistinguishable from their own anti-particles – that is, that they are Majorana particles – it would help to explain the large mass difference, and point to new physics at large energy scales [24].

There are additional motivating factors that suggest neutrinos to be Majorana particles. The weak interaction, the only interaction by which these neutral leptons are detected, violates parity conservation. Charged-current weak interactions involve only neutrinos of left-handed helicity (ν_L), and anti-neutrinos of right-handed helicity ($\overline{\nu_R}$). These are the CPT mirror images of each other. Since neutrinos are massive particles, it is possible to Lorentz boost each of these to a frame where the helicity is reversed, $\nu_L \rightarrow \nu_R$ and $\overline{\nu_R} \rightarrow \overline{\nu_L}$. In the case where neutrinos are Dirac particles, distinguishable from their own anti-particles, this leaves us with four distinct neutrino states with the same mass: ν_L; ν_R; $\overline{\nu_L}$; $\overline{\nu_R}$, only the first and last detectable. In the Majorana case, these four states can be reduced to two: ν and $\bar{\nu}$ respectively being the left- and right-handed representations of the same particle. Both a Lorentz boost and CPT take each of these states into the other. The two non-interacting states are elegantly swept away [21].

If neutrinos were shown to be Majorana, this would help explain their low mass with respect to the rest of the Standard Model fermions. To see this, the mass terms of the neutrino Lagrangian must be examined, as is described by Kayser [21]. From a chirally left-handed neutrino field ν_L^0 and a chirally right-handed neutrino field ν_R^0, the following Lorentz-invariant mass terms can be generated:

$$\mathcal{L}_D = -m_D\overline{\nu_R^0}\nu_L^0 + h.c. \tag{2.1}$$

$$\mathcal{L}_{mL} = -\frac{m_L}{2}\overline{(\nu_L^0)^C}\nu_L^0 + h.c. \tag{2.2}$$

$$\mathcal{L}_{mR} = -\frac{m_R}{2}\overline{(\nu_R^0)^C}\nu_R^0 + h.c. \tag{2.3}$$

Combining these, we can express the neutrino mass Lagrangian as:

$$\mathcal{L}_{m_\nu} = -\frac{1}{2}\left[\overline{(\nu_L^0)^C}, \overline{\nu_R^0}\right]\begin{bmatrix} m_L & m_D \\ m_D & m_R \end{bmatrix}\begin{bmatrix} \nu_L^0 \\ (\nu_R^0)^C \end{bmatrix} + h.c. \tag{2.4}$$

The neutrino mass matrix in Equation 2.4 can be diagonalized by an appropriate change of basis, and the resulting eigenvalues of this matrix are found to be:

$$\lambda_\pm = \frac{1}{2}\left[(m_R + m_L) \pm \sqrt{(m_R - m_L + 4m_D^2}\right]. \tag{2.5}$$

Assuming $m_L << m_D << m_R$, neglecting m_L, and expanding Equation 2.5 in small

m_D/m_R, we are left with two mass eigenvalues of very different scales:

$$\lambda_- \simeq m_D^2/m_R \tag{2.6}$$

$$\lambda_+ \simeq m_R \tag{2.7}$$

If we associate the lighter of these two mass states with the light neutrinos observed in experiment, then m_R could be the mass of a heavy neutrino. The lighter the light neutrino mass, λ_-, is determined to be, the heavier λ_+ becomes. Furthermore, it is reasonable to assume that the neutrino's Dirac mass is of the same scale as the masses of the quarks and charged leptons, Dirac particles whose masses contain only Dirac components. If this is the case, then the neutral lepton associated with m_R would be quite heavy indeed. For $m_R \sim 10^{15}$ GeV, a mass approaching the scale of Grand Unifying Theories, and $m_D \sim 10^2$ GeV, the mass of the top quark, then $m_D^2/m_R \sim 10^{-2}$ eV, a mass scale predicted by neutrino oscillation experiments, and a target sensitivity for neutrinoless double beta decay experiments. This "Seesaw Mechanism" only works for Majorana neutrinos; should this be the underlying physics, it would explain the large differences between the masses of the neutrinos and those of the quarks and charged leptons, and point to new physics beyond the Standard Model at large energy scales [24] [25].

2.2 Neutrinoless double beta decay

Neutrinoless double beta decay ($0\nu\beta\beta$),

$$(Z, A) \rightarrow (Z + 2, A) + e^- + e^- \tag{2.8}$$

is a second-order electroweak process, predicted to occur should neutrinos indeed be Majorana in nature. An example of this process is shown in Figure 2.1. In the process shown, two neutrons undergo β-decay, converting *down* quarks to *up* through the emission of charged virtual W^- bosons in the usual way, with each W^- yielding an e^- and a $\overline{\nu_e}$. What is unusual about this process is the absorption of the $\overline{\nu_e}$

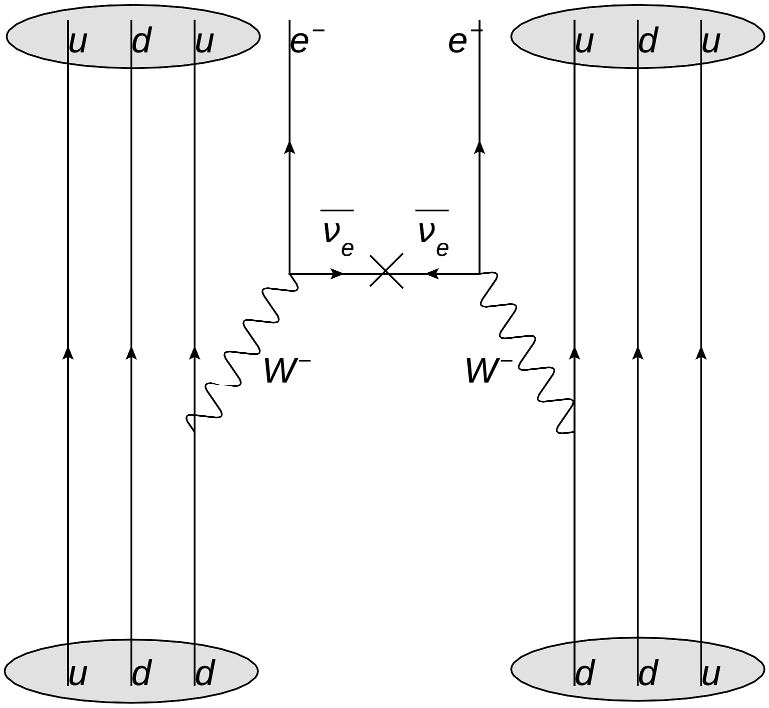

Figure 2.1: Feynman diagram of neutrinoless double beta decay: Annihilation of virtual $\overline{\nu_e}$s require neutrinos to be their own antiparticles, and the emission of two e^-s demonstrate lepton number violation.

emitted at one vertex as a ν_e at another, requiring the $\overline{\nu_e}$ to be its own anti-particle, and violating lepton number conservation, with $\Delta L_e = +2$ [21]. The Standard Model doesn't require the conservation of lepton number, yet the violation of lepton number conservation has not yet been observed [26]. Moreover, if the neutrinos were massless, the $\overline{\nu_e}$ created would be completely right handed, but the absorbed ν_e must be left handed. The amplitude of the projection of a neutrino onto a wrong-handed helicity is proportional to m_ν/E_ν, and the half-life of this process is dependent on mass in the following way:

$$\left(T_{1/2}^{0\nu\beta\beta}\right)^{-1} = \langle m_{\beta\beta}\rangle^2 \, G^{0\nu\beta\beta}(Q,Z) \left| M_{GT}^{0\nu\beta\beta} - \frac{g_V^2}{g_A^2} M_F^{0\nu\beta\beta} \right|^2 , \tag{2.9}$$

where, $\langle m_{\beta\beta}\rangle$ is the effective Majorana mass, $G^{0\nu\beta\beta}(Q,Z)$ is a phase-space factor, dependent on decay end-point energy and nuclear charge, $M_{GT}^{0\nu\beta\beta}$ and $M_F^{0\nu\beta\beta}$ are nuclear matrix elements, and g_V^2 and g_A^2 are vector and axial-vector coupling constants, respectively [21]. While the process shown in Figure 2.1 is thought to be the most likely mode by which $0\nu\beta\beta$ could occur, it's important to note that even if this is not the process responsible, confirmation of $0\nu\beta\beta$ by *any* process implies that neutrinos are Majorana particles, lepton number can be violated, and that new physics beyond the Standard Model is at work [27].

The confirmation of the existence of neutrino oscillations demonstrated not only that neutrinos have mass, but also that neutrinos created in a definite flavor eigenstate, $|\nu_\alpha\rangle$, are not produced in a single mass eigenstate $|\nu_i\rangle$, but in a linear combination as described by the neutrino mixing matrix $U_{\alpha,i}$:

$$|\nu_\alpha\rangle = \sum_i U_{\alpha,i}^* \, |\nu_i\rangle \, . \tag{2.10}$$

Electron neutrinos are produced in vertices involving W^- as shown in Figure 2.1. The calculation of the $0\nu\beta\beta$ amplitude then involves taking the coherent sum of the mass states from which the ν_e is derived. Each vertex contributes a factor proportional to

$U_{e,i}$, yielding:

$$\langle m_{\beta\beta} \rangle = \left| \sum_i m_i U_{e,i}^2 \right| = \left| \sum_i \left| U_{e,i}^2 \right| e^{\alpha_i} m_i \right|^2 . \tag{2.11}$$

The PMNS[1] matrix, $U_{\alpha,i}$, is unitary in the case of three flavor and three mass states, with six independent parameters: three mixing angles, a CP violating phase, and two so-called Majorana phases: the e^{α_i} in Equation 2.11. The Majorana phases influence the $0\nu\beta\beta$ decay rates, but are inaccessible by neutrino oscillation experiments. Additionally, these phases may conspire to suppress the effective Majorana mass, or bring it to zero [21].

The possible range of $\langle m_{\beta\beta} \rangle$ values is a function of the lightest neutrino mass, and the hierarchy of the mass splittings measured through oscillations. If the mass states are ordered so as to coincide with their associated charged leptons, (i.e. the m_1 state, which is mostly ν_e, should prove to be the lightest), it is said that the mass states follow the "normal" hierarchy, $m_1 < m_2 < m_3$, with the solar neutrino mass splitting below the atmospheric. It's possible that the mass splittings are reversed, yielding the "inverted" hierarchy, $m_3 < m_1 < m_2$. In the case that the magnitudes of the splittings are small compared to the absolute scale on which they sit, the hierarchy is referred to as "degenerate." As shown in Figure 2.2, measurements or limits set near 10^{-2} eV, combined with information on $m_{\nu_{min}}$ from kinematic measurements would give valuable information in disentangling the hierarchies.

2.2.1 Measurement of neutrinoless double beta decay

Neutrinoless double beta decay can only be observed in source nuclei in which β-decay is energetically forbidden. If this were not the case any $0\nu\beta\beta$ signal would be lost in an overwhelming β-decay background. Take as an example the case of ^{136}Xe as shown in Figure 2.3. ^{136}Xe is energetically stable against β-decay, but double beta decay is allowed, and can proceed in either of two distinct ways. The $0\nu\beta\beta$ mode previously discussed competes with a second second, vastly more common — and vastly less interesting — double beta decay mode. $2\nu\beta\beta$ is the following Standard

---

[1] Pontecorvo, Maki, Nakagawa and Sakata

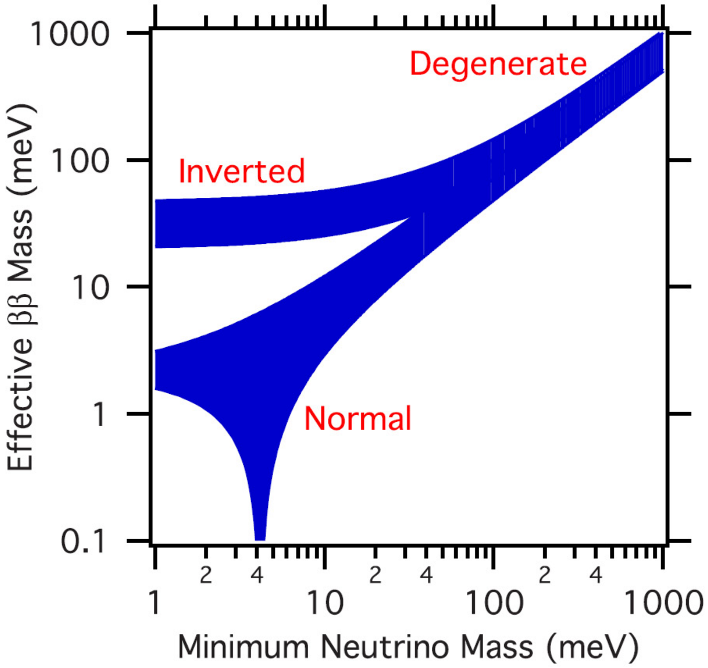

Figure 2.2: Effective Majorana mass $\langle m_{\beta\beta} \rangle$ vs. mass of the lightest neutrino state $m_{\nu_{min}}$ for normal, inverted and degenerate hierarchies. Figure credit: [7].

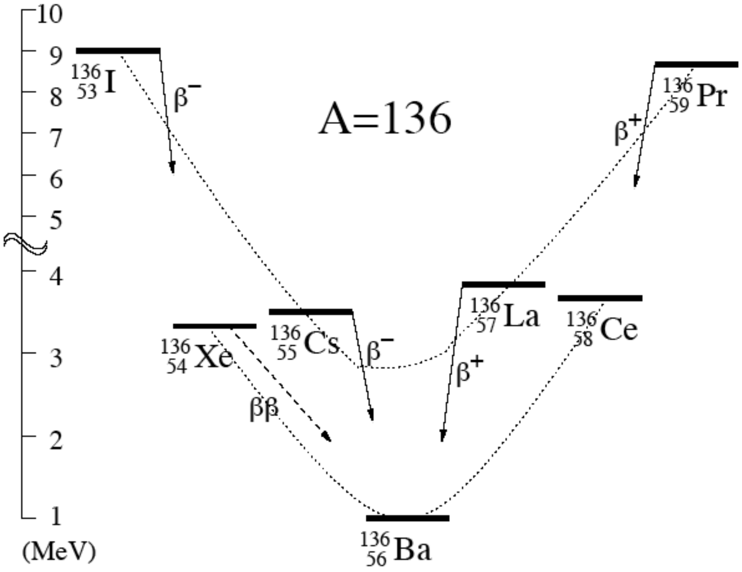

Figure 2.3: Binding energies of nuclei with $A = 136$. ^{136}Xe→^{136}Cs β-decay is energetically forbidden, but ^{136}Xe→^{136}Ba $\beta\beta$-decay is not.

Model process:

$$(Z, A) \rightarrow (Z + 2, A) + 2e^- + 2\overline{\nu_e}, \tag{2.12}$$

which differs from $0\nu\beta\beta$ in that the two expected anti-neutrinos are emitted with the electrons, in accordance with lepton-number conservation. $2\nu\beta\beta$ does not require neutrinos to be Majorana particles, and its occurrence has been experimentally verified in several nuclei (not including ^{136}Xe). In any attempt to detect neutrinoless double beta decay, the two-neutrino mode presents a background which must be mitigated. Direct detection of the neutrinos emitted in $2\nu\beta\beta$ is an impractical task, but their presence can be inferred kinematically. In the case of $2\nu\beta\beta$, the emitted anti-neutrinos are given an indeterminate amount of the energy of the decay, and if the energy of the emitted electrons is summed, the spectrum forms a continuum between zero and the Q-value of the decay. On the other hand, in $0\nu\beta\beta$ decays, all of the energy is in the electrons, and so the energy spectrum is a delta-function spike at the Q-value[2]. As seen in Figure 2.4, the energy resolution of the detector must be

---

[2] The kinetic energy of the recoiling nucleus has a negligible effect on the electron kinematics

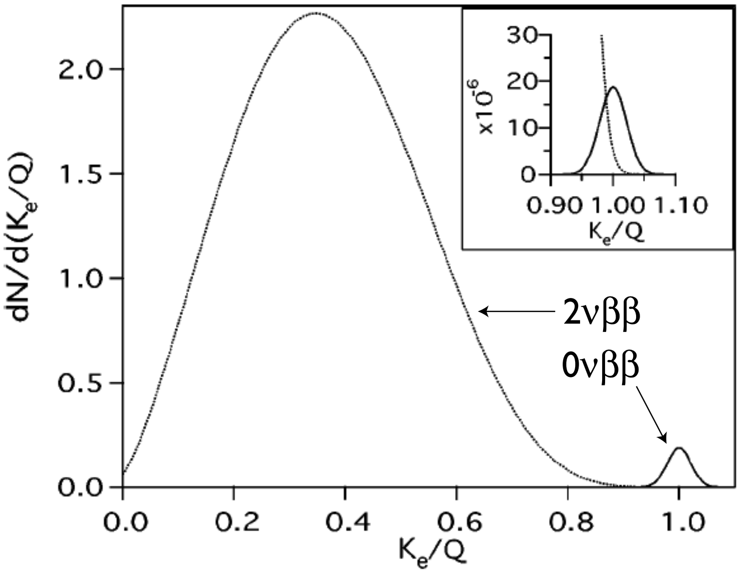

Figure 2.4: Combined $0\nu\beta\beta$ and $2\nu\beta\beta$ energy spectra. The $2\nu\beta\beta$ events are normalized to 1; $0\nu\beta\beta$ events are normalized to 10^{-2} (10^{-6} in the inset). Figure credit: [3].

sufficient to separate these two signals, and the relative rate of $2\nu\beta\beta$ determines the resolution required for a given $0\nu\beta\beta$ lifetime sensitivity.

2.2.2 Current lifetime and effective mass limits

Table 2.1 shows the Q-values, current $0\nu\beta\beta$ half-life limits and $2\nu\beta\beta$ measured or limited half-lives for several candidate source nuclei. The nuclear matrix elements and phase space factors for each nucleus is different, so the half-lives are not exactly comparable in terms of effective Majorana mass. Applying Equation 2.9 to the $0\nu\beta\beta$ limits will yield effective double beta decay mass limits, with one caveat — the nuclear matrix elements $M_{GT}^{0\nu\beta\beta}$ and $M_{F}^{0\nu\beta\beta}$ vary from species to species, and without measuring neutrinoless double beta decay in a nucleus there is no experimental method for obtaining their values. They have been estimated through theoretical calculations for a variety of species, including those listed above, using two differing methods: the Quasiparticle Random Phase Approximation (QRPA) and the Interacting Shell Model (ISM). These two methods give differing values, but as calculations have been

Isotope	Abundance [%]	$T_{1/2}^{2\nu\beta\beta}$ [yr]	$T_{1/2}^{0\nu\beta\beta}$ [$\times 10^{21}$ yr]
^{48}Ca	0.19	$(4.3^{+2.4}_{-1.1} \pm 1.4) \times 10^{19}$	>14
^{76}Ge	7.61	$(1.74^{+0.18}_{-0.16} \pm 0.01) \times 10^{21}$	>15700
^{76}Ge			$15000^{+168000}_{-7500}$
^{82}Se	8.73	$(1.03 \pm 0.03 \pm 0.07) \times 10^{20}$	>140
^{96}Zr	2.80	$(2.1^{+0.8}_{-0.4} \pm 0.2) \times 10^{19}$	>1.0
^{100}Mo	9.63	$(7.68 \pm 0.02 \pm 0.54) \times 10^{18}$	>460
^{116}Cd	7.49	$(2.9^{+0.4}_{-0.3}) \times 10^{19}$	>170
^{130}Te	34.1	$6.1 \pm 1.4^{+2.9}_{-3.5} \times 10^{20}$	>3000
^{136}Xe	8.87	$> 8.1 \times 10^{20}$	>1200

Table 2.1: Current $2\nu\beta\beta$ and $0\nu\beta\beta$ half-lives and limits, adapted from [1][2]&[3]. Limits are 90% confidence level. Ge^{76} is listed twice to reflect contentious claim of $0\nu\beta\beta$ discovery of Klapdor-Kleingrothaus et al. [4].

refined, the differences between the two models have been shrinking. Whether they have been trending toward the true matrix element values remains to been seen. For this reason, in order to obtain a measurement of neutrino mass, $0\nu\beta\beta$ needs to be measured in at least two isotopes. Information on nuclear matrix element calculations can be found in [28] and references therein.

Table 2.1 lists both a limit and value for the $0\nu\beta\beta$ half-life of ^{76}Ge. A claim for evidence of $0\nu\beta\beta$ in ^{76}Ge has been made by what is only a portion of the Heidelberg-Moscow collaboration [4], and has subsequently been challenged by much of the community, including other members of that collaboration [29]. Though this claim has been updated with increased statistics [30], its legitimacy remains in doubt, and confirmation or rejection of this claim is a goal of the current generation of 100-kg-scale $0\nu\beta\beta$ experiments.

In order to subsequently reach the interesting mass regime of 10 meV, half-life sensitivities must be further pushed to the 10^{28} year scale. In order to reach these exceedingly long half-lives, tons of source material must be acquired, experiments need long run-times, and novel approaches to elimination of radiological backgrounds need to be explored.

2.3 Neutrinoless double beta decay in ^{136}Xe

The Enriched Xenon Observatory for double beta decay (EXO) is a proposed $0\nu\beta\beta$ detector, currently in a research and development phase, with a ton-scale volume of ^{136}Xe as its source material. As a source, ^{136}Xe offers several advantages, chief amongst these the possibility of tagging the Barium ion daughter of the decay spectroscopically for the purposes of background elimination [22][23].

The selection of ^{136}Xe as a source for a $0\nu\beta\beta$ experiment makes good sense for a number of reasons. As an inert gas, it is easy to chemically purify. Because it is a fluid, that purification can be performed repeatedly, and perhaps continuously, over the lifetime of an experiment. In either gas or liquid phase, the Xenon serves as both the source and detector material in a time projection chamber (TPC). This prevents degradation of the energy resolution due to slowing in the source material, as is seen in detectors measuring energies of electrons leaving solid sources. Additionally, there are no long-lived cosmogenic isotopes which can be activated in Xenon. As can be seen in Table 2.1, most $0\nu\beta\beta$ candidate isotopes have natural abundances of less than 10%, and enrichment of the source may be required to keep detector sizes manageable and limit backgrounds. As a gas, and the heaviest isotope of Xenon, ^{136}Xe is easily isotopically enriched by ultra-centrifuge with relative ease.

The unique advantage of the use of ^{136}Xe is that the product of its double beta decay, ^{136}Ba, has rather strong optical atomic transitions when singly charged. Ba^{+} ions can be stored for extended periods of time in radio-frequency traps, and laser-induced resonance fluorescence can be used to detect single stored ions with high sensitivity. With this in mind, it is the goal of the EXO collaboration to demonstrate that the Ba-ion daughter of a candidate double beta decay event can be extracted from a Xenon TPC, stored in an ion trap, and positively identified as Barium. A positive detection of the Barium ion would confirm that a double beta decay event occurred, and rule out radiological backgrounds as the cause of candidate events. It would not, however, differentiate between the $0\nu\beta\beta$ and $2\nu\beta\beta$ decay modes. A detector with sufficient energy resolution is required to to remove the $2\nu\beta\beta$ background.

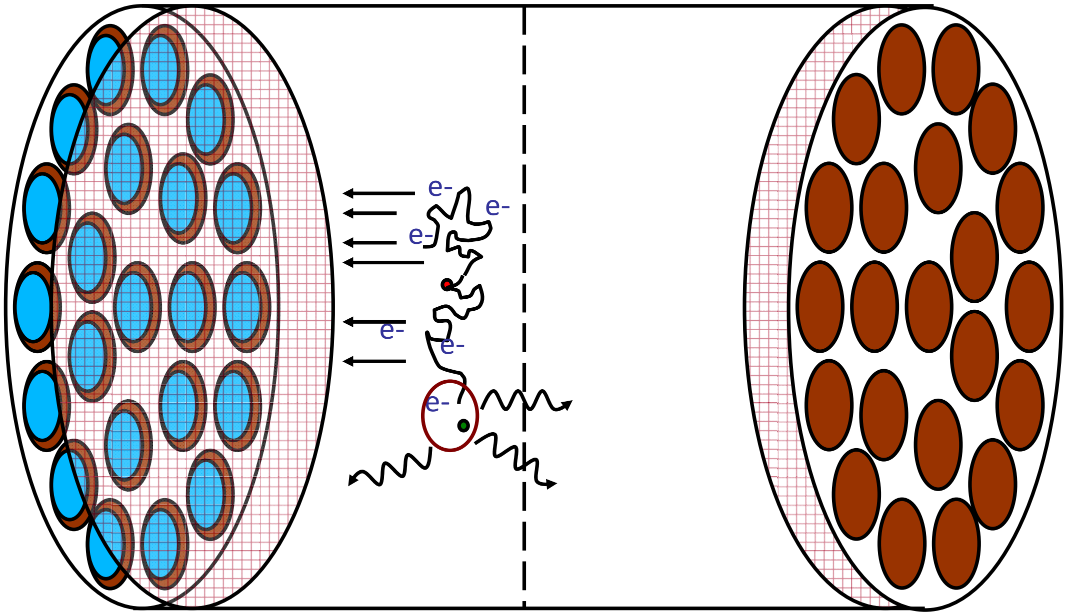

Figure 2.5: A liquid Xenon TPC. An event ionizes some of the surrounding Xenon, creating region of ionization. Recombination of some of this ionization produces scintillation, detected by APDs at either end. The rest is drifted to crossed-wire cathodes for collection.

2.3.1 Energy resolution in liquid Xenon

For the work in this thesis, a liquid Xenon TPC is considered, though the option for a high-pressure gaseous TPC exists. The EXO collaboration is researching both possibilities, and it would even be possible to construct first one, then the other, and reuse the same enriched ^{136}Xe source. A liquid Xenon TPC is shown schematically in Figure 2.5. When a double beta decay occurs, the electrons ionize the surrounding Xe. Some of the resulting ionization recombines into excited dimers, which emit 175-nm scintillation light with a lifetime of 4.3-nsec and 22-nsec, for the dimer singlet and triplet decays, respectively. The prompt detection of these scintillation photons by suitable photo-detectors provides a time stamp for the event, and provide the first component of the measurement of the event energy. The scintillation photons are in the vacuum ultraviolet, and as a result photodetectors with sensitivity at 175nm need to be used. The remaining electrons, those not recombined, are drifted by the high voltage of the TPC to a crossed-wire anode, where they're collected. The distribution of charge on the electrodes yields a two-dimensional localization of the initial event, and the total amount of charge collected, when combined with the scintillation collected, gives a precise measurement of the total event energy. The drift time of the electrons in the TPC field gives the event localization along the axis orthogonal to the crossed wires of the anode, completing the three-dimensional event reconstruction.

As the ionization electrons produced by the energy of the event are shared between the scintillation and ionization channels, in order to most accurately measure the energy of an event, both of these channels need to be sampled. This is seen most clearly when these two channels are plotted against each other on an event-by-event basis, as seen in the 2D histogram shown in Figure 2.6 In Conti et al. [8], the 570-keV and 1064-keV decays of ^{207}Bi were measured in a small liquid Xenon TPC, to demonstrate the capabilities of liquid Xenon as a detector medium. The anti-correlation between the scintillation and ionization channels were observed in each peak, demonstrating that better energy resolution can be obtained by combining the two channels. The energy resolution obtained in this study was 3% at 570 keV, translating to 1.6% at the ^{136}Xe double beta decay endpoint; this is sufficient for separating the $0\nu\beta\beta$ events from the $2\nu\beta\beta$ up to a $0\nu\beta\beta$ half-life of 2×10^{28} years, given the present limit on the $2\nu\beta\beta$ half-life listed in [3].

The EXO collaboration has built and is currently commisioning a liquid Xenon TPC which is to use 200kg of Xenon enriched to 80% in ^{136}Xe, which it has named EXO-200. As a precursor to a ton-scale EXO experiment, EXO-200 seeks to more fully understand the performance of a large liquid Xenon TPC. EXO-200 will have an increased scintillation light collection yield over the chamber studied in [8], through the use of 468 high quantum efficiency large area avalanche photodiodes (LAAPDS) [31].

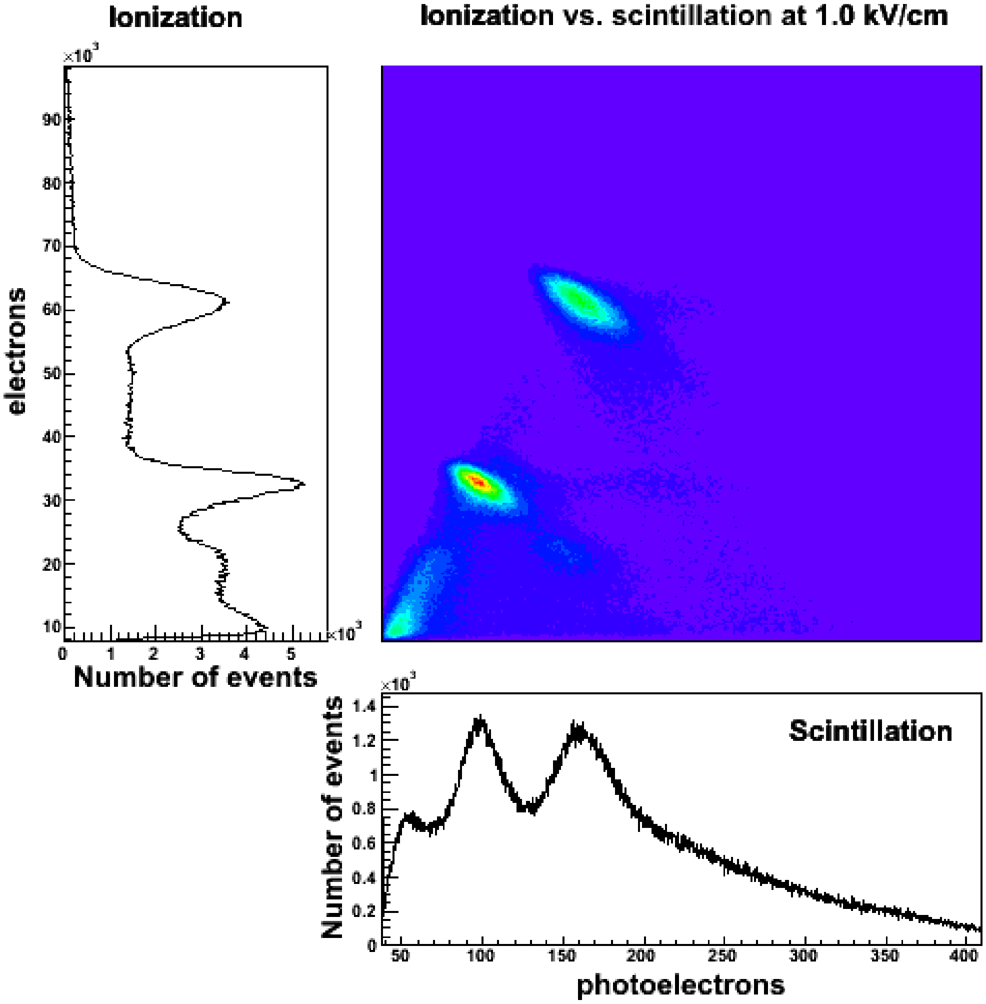

Figure 2.6: 2D histogram of scintillation and ionization in liquid Xenon from a ^{207}Bi source. 2D peaks are narrower than scintillation and ionization peaks when measured alone. Figure credit: [8]

This is expected to lead to an improved energy resolution in EXO-200, perhaps approaching 1%. As a stand-alone project consisting of the largest enriched mass of double beta decay source material ever assembled, it seeks to set new effective neutrino mass limits, and make a statement about the Klapdor-Kleingrothaus et al. claim [30]. Toward this end, as EXO-200 does not involve Barium tagging, the experiment has been constructed using low radioactivity background methods, which has included a comprehensive evaluation of radioactive contamination of every material used in detector construction, and a wide variety of others as well [32].

2.3.2 Ton-scale EXO

One scheme proposed (and the one which will be discussed in the remainder of this dissertation) for the detection of the Barium ion daughter, and its verification of the occurrence of a double beta decay event, involves the extraction of the Barium ion from the liquid Xenon volume by means of an extraction probe, transport into a radio-frequency ion trap, and its spectroscopic detection there. The 3D event reconstruction by the TPC will give the event location, and by application of high voltage to an extraction probe that ion can be collected. The probe itself can be robotically driven through a set of load-locks to a waiting ion trap, where the ion can be released and captured. Cooled by collisions with a background gas, the ion will settle in a region where it can be excited by resonant lasers, and the spontaneously emitted fluorescence light can be detected by CCD. This signal can not be faked by the product of a radiological background, and so confirms the initial event in question as a double beta decay.

With an energy resolution capable of separating the $0\nu\beta\beta$ candidate events from the $2\nu\beta\beta$ background, and the effective implementation of a Barium-ion tagging system for elimination of radioactive backgrounds, a ton-scale EXO experiment would have a sensitivity to effective Majorana masses approaching or exceeding 10 meV, as shown in Table 2.2. In the calculation of these sensitivities, two cases are listed which could be considered to represent a conservative and aggressive implementation of a ton-scale detector. In the conservative case, one ton of Xe enriched to 80% in ^{136}Xe

Case	Mass	Eff.	Time	σ_E/E	2ν Bknd	$T_{1/2}^{0\nu\beta\beta}$	$\langle m_{\beta\beta}\rangle$
Conservative	10^3 kg	70%	5 yr	1.6%	1 event	2×10^{27} yr	24-33 meV
Aggressive	10^4 kg	70%	10 yr	1.0%	1 event	4.1×10^{28} yr	5.3-7.3 meV

Table 2.2: Projected EXO sensitivity for conservative and aggressive resolution and exposure estimates.

is used as source for a period of five years. An energy resolution of 1.6% is assumed in this conservative case; this resolution has been demonstrated in a liquid Xenon TPC. In the more agressive case, 10 tons of enriched Xenon are observed over the course of 10 years. An energy resolution of 1% is substituted. This is the resolution expected in a large detector with improved scintillation light collection efficiency. In both cases, a $0\nu\beta\beta$ detection efficiency of 70% is assumed, and the uncertainties in the $\langle m_{\beta\beta}\rangle$ sensitivities arise from the uncertainties in the calculations of the nuclear matrix elements.

Chapter 3

Radiofrequency ion trapping

While *in situ* detection of single Barium ions in a Xenon time projection chamber may yet be proven possible, to this day their spectroscopic identification has only been demonstrated through confinement in radio-frequency ion traps. The Barium tagging methods explored in this work revolve around the extraction of ions from a Xenon volume using an electrostatic probe, and the release of the ion into an RF trap, where it can be slowed and stored for extended periods of time while laser spectroscopy can be performed.

3.1 Linear RFQ confinement of charged particles

The fact that electrostatic potentials obey Laplace's equation in free space implies that they alone cannot be used to confine charged particles. Local minima of the electric potential can only exist in locations where charge density is non-zero; in the absence of charge, local minima cannot simultaneously exist in all dimensions. Penning traps introduce a strong, static, magnetic field, about which ions orbit while a static electric field confines them along the magnetic field direction. While this method of confinement involves only static fields, the presence of the strong magnetic field introduces shifts in the magnetic sublevels of the ion. Radiofrequency Paul traps avoid the use of strong magnetic fields, instead oscillating an inhomogeneous electric potential in a manner that causes stable confinement of charged particles. Several seminal works and review articles have described the theory and operation of RF traps, and the key concepts pertaining to linear quadrupole traps are reproduced here [33][34][35][36].

3.1.1 The adiabatic approximation

While the motion of an ion in an RF trap is analytically solvable, it is perhaps more illustrative of the basic principles by which RF traps operate to introduce the adiabatic approximation of Kapitsa, as described in Landau and Lifshitz [37]. Consider an ion of charge q and mass m in motion in a spatially uniform, oscillating electric field $\vec{E} = \vec{E_0}\cos(\Omega t)$. Its motion is described by the following equations:

$$\begin{aligned}
\vec{a}(t) &= \frac{q\vec{E_0}}{m}\cos(\Omega t) \\
\vec{v}(t) &= \frac{q\vec{E_0}}{m\Omega}\sin(\Omega t) + \vec{v_0} \\
\vec{r}(t) &= -\frac{q\vec{E_0}}{m\Omega^2}\cos(\Omega t) + \vec{v_0}t. \qquad (3.1)
\end{aligned}$$

The field induces oscillatory motion in the ion at its driving frequency on top of its center of mass velocity v_0. The ion has a kinetic energy given by:

$$\begin{aligned}
T(t) &= \frac{1}{2}m\vec{v}(t)\cdot\vec{v}(t) \\
T(t) &= \frac{1}{2}m\left[\frac{q^2}{m^2\Omega^2}\sin^2(\Omega t)\left|\vec{E_0}\right|^2 + \frac{2q}{m\Omega}\sin(\Omega t)\left(\vec{E_0}\cdot\vec{v_0}\right) + \left|\vec{v_0}\right|^2\right] \qquad (3.2)
\end{aligned}$$

and time-averaged kinetic energy:

$$\begin{aligned}
\langle T\rangle &= \frac{\Omega}{2\pi}\int_0^{\frac{2\pi}{\Omega}} T(t)\mathrm{d}t \\
\langle T\rangle &= \frac{\Omega}{2\pi}\left[\frac{q^2}{2m\Omega^2}\left(\frac{\pi}{2}\right)\left|\vec{E_0}\right|^2 + 0 + \frac{1}{2}m\left(\frac{2\pi}{\Omega}\right)\left|\vec{v_0}\right|^2\right] \\
\langle T\rangle &= \frac{q^2\left|\vec{E_0}\right|^2}{4m\Omega^2} + \frac{1}{2}m\left|\vec{v_0}\right|^2. \qquad (3.3)
\end{aligned}$$

The second term is readily recognizable as the kinetic energy associated with the center of mass motion at velocity v_0. The first term then is the additional kinetic energy associated with the oscillating field. As the restriction to a uniform electric field is relaxed to one with a weak gradient, this energy of oscillation varies spatially with the square of the amplitude of the oscillating field. Since the oscillating field is 90° out of phase with the oscillating component of the velocity, the field can't contribute to the ion's total kinetic energy. The overall average kinetic energy remains constant, and energy is transferred from the average center of mass motion to the oscillatory motion, and vice versa. Thus the oscillation kinetic energy behaves as an effective pseudopotential, exerting an average force in the direction of decreasing RF field amplitude.

3.1.2 Linear RF quadrupole traps

Linear RF quadrupole traps are assembled from parallel rods as in the configuration shown in Figure 3.1. By applying a voltage of $\frac{V_{RF}}{2}\cos(\Omega t)$ to the electrodes positioned on the x-axis, and a voltage of $-\frac{V_{RF}}{2}\cos(\Omega t)$ to those on the y-axis, an oscillating hyperbolic potential is produced in the interior. Approximately,

$$\Phi_{RF} = \frac{V\cos(\Omega t)}{2}\left(\frac{x^2 - y^2}{r_0^2}\right) \tag{3.4}$$

To determine the effective potential, Ψ_{RF}, that this electrode configuration produces, find the amplitude of the oscillating electric field, and substitute into the first term of Equation 3.3.

$$\begin{aligned} \vec{E}_{RF} &= -\nabla\Phi_{RF} = -\frac{V\cos(\Omega t)}{r_0^2}(x\hat{x} - y\hat{y}) \\ \left|\vec{E}_0\right|^2 &= \frac{V}{r_0^4}\left(r^2\right) \\ \Psi_{RF} &= \frac{q^2V^2r^2}{4m\Omega^2r_0^4} \end{aligned} \tag{3.5}$$

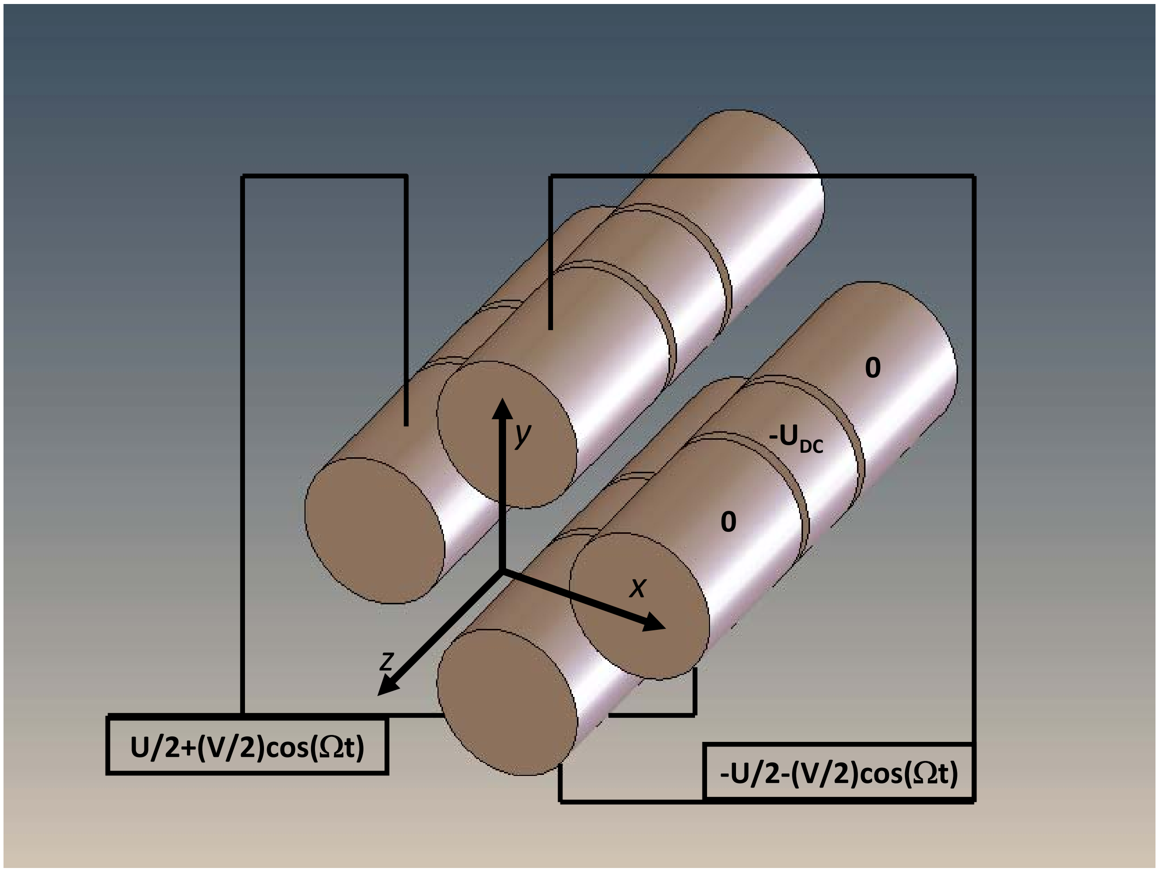

Figure 3.1: Typical electrode configuration for a linear ion trap. V is the amplitude of the AC confining potential, U is a static potential difference between x and y axes, U_{DC} is a static axial confinement potential.

The effective potential is that of a two-dimensional harmonic oscillator, with a depth given by the difference in the effective potential at the trap center ($r = 0$), and at an electrode ($r = r_0$):

$$\text{Depth} = \frac{q^2V^2}{4m\Omega^2 r_0^2}. \tag{3.6}$$

The frequency of the large amplitude motion of the ion in this harmonic well is the same along both axes:

$$\omega_x = \omega_y = \frac{qV}{\sqrt{2}m\Omega r_0^2}. \tag{3.7}$$

The symmetry between the x and y axes can be broken by the introduction of a static electric potential, U in Figure 3.1. This generates a static hyperbolic potential which is superimposed on the pseudopotential generated by the radiofrequency:

$$\begin{aligned}\Psi_{RF+DC} &= \frac{q^2V^2}{4m\Omega r_0^4}\left(x^2+y^2\right)+\frac{qU}{2r_0^2}\left(x^2-y^2\right)\\ \Psi_{RF+DC} &= \left(\frac{q^2V^2}{4m\Omega r_0^4}+\frac{qU}{2r_0^2}\right)x^2+\left(\frac{q^2V^2}{4m\Omega r_0^4}-\frac{qU}{2r_0^2}\right)y^2\end{aligned} \tag{3.8}$$

A positive U increases the frequency of the secular motion along the x-axis, while decreasing it along the y-axis. The maximum trap depth is decreased by $q\left|U\right|/2$, regardless of the sign of U, and the trap can no longer confine when this surpasses the psuedopotential, or equivalently when

$$|U| \geq \frac{qV^2}{2m\Omega^2 r_0^2}. \tag{3.9}$$

The psuedopotential formulation is only a reasonable approximation when the change in the electric field due to the ion motion is small when compared to that due to field oscillation, or equivalently when $\omega_x, \omega_y << \Omega$. In §3.1.3 the full analytical treatment of the radial confinement is detailed, and the strict conditions for ion stability in a hyperbolic radiofrequency potential will be given.

3.1.3 The Mathieu Equation

The full equations of motion for an ion in the combined static and oscillating fields described in §3.1.2 and shown in Figure 3.1 are the following:

$$\begin{aligned} m\ddot{x} &= -\frac{q}{r_0^2}\left[U + V\cos(\Omega t + \phi_{RF})\right]x \\ m\ddot{y} &= \frac{q}{r_0^2}\left[U + V\cos(\Omega t + \phi_{RF})\right]y \end{aligned} \tag{3.10}$$

Each of these uncoupled differential equations are seen to be instances of the Mathieu Equation:

$$\frac{\mathrm{d}^2u}{\mathrm{d}\tau^2} + \left[a_u - 2q_u\cos(2\tau)\right]u = 0, \tag{3.11}$$

when the judiciously chosen change of variables,

$$\begin{aligned} u \in x, y \quad \tau &= \frac{1}{2}\left(\Omega t + \phi_{RF}\right) \\ q_x = -q_y &= \frac{2qV}{m\Omega^2 r_0^2} \\ a_x = -a_y &= \frac{4qU}{m\Omega^2 r_0^2} \end{aligned} \tag{3.12}$$

is applied [33]. The stable solutions of the Mathieu Equation take the following series form

$$u(\tau) = Ae^{i\beta_u\tau}\sum_{n=-\infty}^{\infty} C_{2n}e^{i2n\tau} + Be^{-i\beta_u\tau}\sum_{n=-\infty}^{\infty} C_{2n}e^{-i2n\tau}, \tag{3.13}$$

where the coefficients A and B are chosen to satisfy ion initial position and velocity conditions, and the C_{2n} depend only on q_u and a_u, which are defined by the trapping potential. By differentiating Equation 3.13 twice and inserting into Equation 3.11, values of the C_{2n} can be obtained recursively:

$$C_{2n+1} - D_{2n}C_{2n} + C_{2n-2} = 0, \tag{3.14}$$

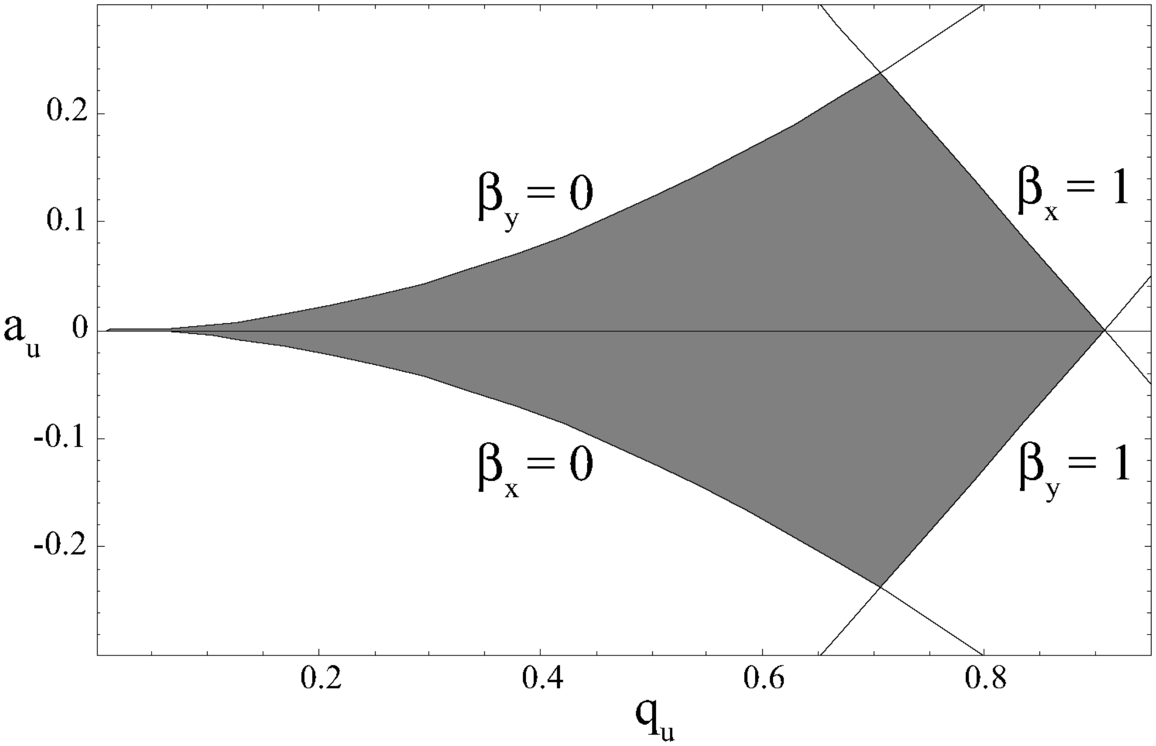

Figure 3.2: Stability conditions for a linear RF ion trap in q_x, a_x. The shaded region denotes stability.

where the D_{2n} are constants defined in the following way:

$$D_{2n} \equiv \left[a_u - (2n + \beta_u)^2\right] / q_u. \tag{3.15}$$

Bound solutions to the Mathieu Equation exist for parameters q_u and a_u that yield values of β_u between 0 and 1. A linear RF trap is confining when β_x and β_y satisfy this condition simultaneously. The boundaries defined by $\beta_x = 0, 1$ and $\beta_y = 0, 1$ then encompass a region of stability, as shown in Figure 3.2. The calculation of β_x and β_y can be simplified by truncation of the series solution of the Mathieu equation to the terms $n = 0, \pm 2$, and setting all others to zero. This is the lowest-order approximation that includes ion behavior at the RF frequency. In this case the ion's equations of motion reduce exactly to those found by the procedure prescribed in §3.1.1, and the

$\beta_{x,y}$ are approximately:

$$\beta_u \approx \sqrt{a_u + q_u^2/2}. \tag{3.16}$$

3.1.4 Axial confinement

Due to the symmetry of the radiofrequency field along a linear trap's longitudinal (z) axis, confinement along this axis must be achieved by other means. This is done by overlaying a static potential, with minimum at the trap center. In the configuration shown in Figure 3.1, this is done by dividing each of the rod electrodes into segments, and placing the same AC but differing DC potentials on the different segments of the same rod. A one-dimensional minimum is produced in segment 2, with depth somewhat less than U_{DC}, as Laplace's equation requires the minimum of the potential to be found on the electrodes, and not in the trap volume. Since the total effective potential for the trap is the sum of the effective potential given in Equation 3.8 and the potential generated for the axial confinement, Φ_{DC}:

$$\Psi_{TOT} = \Psi_{RF+DC} + \Phi_{DC}, \tag{3.17}$$

the potential difference between the trap center and the electrodes reduces the effective radial trap depth, and breaks the rotational symmetry around the z-axis. Whereas the analytical form of Ψ_{RF+DC} is generally easy to derive, derivation of a general form for Φ_{DC} is difficult to impossible. Numerical solutions for a particular geometry are easily obtained, however, using a variety of finite element analysis tools.

SIMION8, a numerical electric field and particle trajectory simulation package[38], has been used extensively throughout this work for the purposes of testing ion confinement and tuning trapping parameters. Figure 3.3 depicts the trajectory of a mass 138 ion confined in the trap of Figure 3.1, with $V = 200$V, $\Omega_{RF} = 2\pi \times 2.2$MHz, $U = 1$V, $U_{DC} = 5$V. The low amplitude motion of the ion at the RF drive frequency, known as the micromotion, is clearly visible on the projections of the ion's motion on the x and y axes, and is absent on the ion's z motion. The ion's motion is independent along each of the axes, and the simulated ion trajectory has equal energy in each of it's three degrees of freedom. The effect of U is seen in the ion's tighter

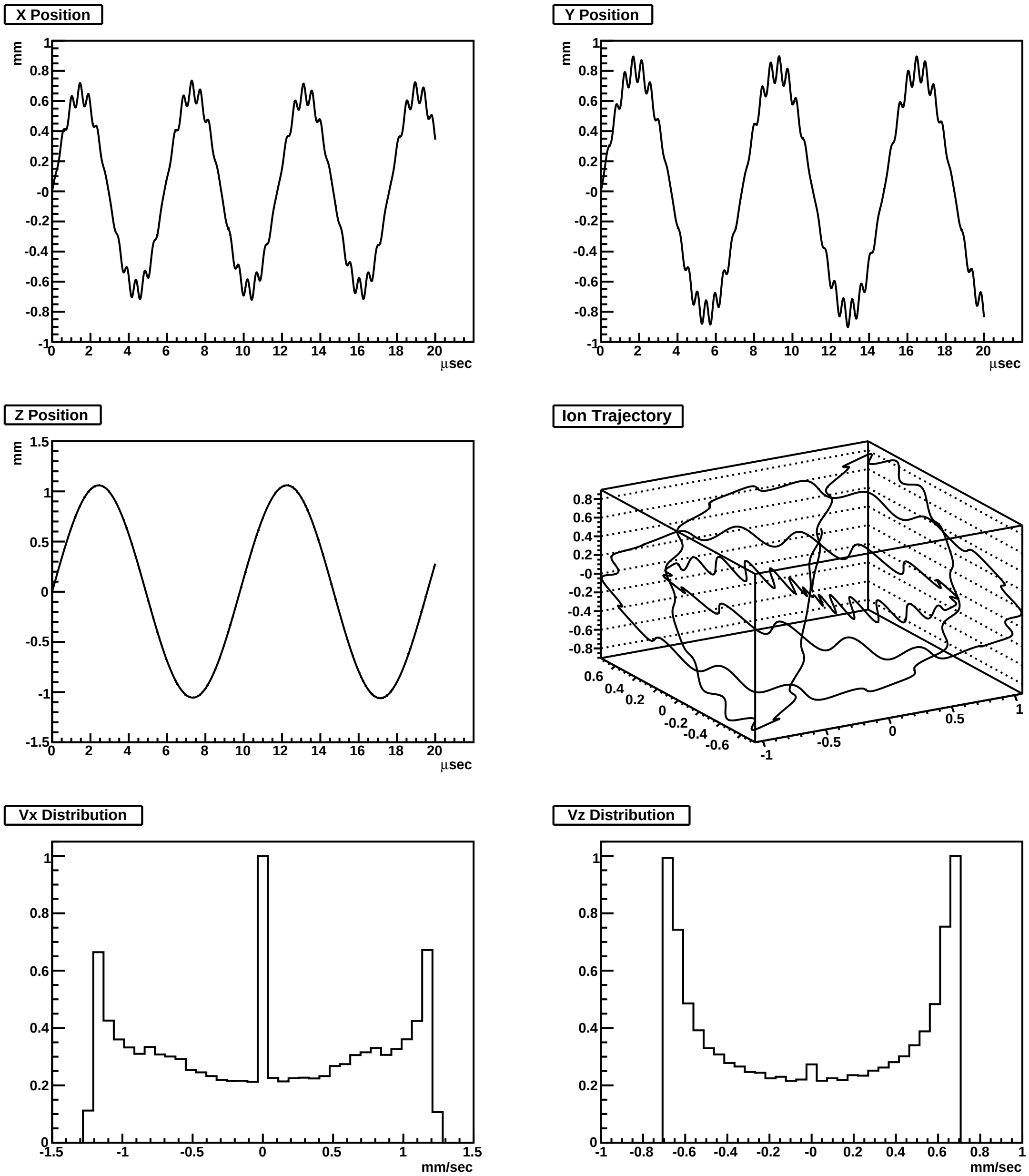

Figure 3.3: Simulated trajectory of a trapped ion. The x- and y-positions as a function of time exhibit the micromotion due to the RF drive. The z-position, lacking RF drive, does not. The combined motion is a modified Lissajous pattern. The RF drive creates a peak at zero in the x-velocity distribution, absent from the z-velocity distribution, due to frequent direction changes.

confinement along the x-axis than that along y, increasing the frequency of oscillation along x. The distributions of the velocity projections along x and z are also shown in Figure 3.3. While the v_z distribution is that of a classical harmonic oscillator, the $v_{x,y}$ distributions include a peak at $v = 0$, the result of frequent direction changes associated with the RF-induced micromotion present along those axes. In both cases the separation of the sidebands is a measure of the ion's energy, and the cooling of an ion will collapse these distributions to zero. In §4.3.2, the relationship between the ion's velocity profile and optical spectroscopy will be examined in detail.

3.2 Simulation of ion collisions with inert gases

Thus far only completely isolated trapped ions have been considered. Background gases play a significant role in this work as ion-consuming chemical impurities, cooling media and destabilizing contaminants. The EXO experiment intends to capture Ba^+ ions that have been expelled from an ion extraction probe, and in order to trap and detect them effectively they must be slowed and cooled. An extended linear trap with more than the three minimum segments and increased length is a suitable tool for this purpose. In order to dissipate the energy imparted to the ion upon injection to the trap, an inert buffer gas at room temperature is allowed to fill the trap, collisions with which will cool the ion until it is in thermal equilibrium with the gas.

In order to understand the effects of a background gas on the confinement of a trapped ion, we must first develop an appropriate model for ion-neutral collisions to be used in simulations. The highly reactive nature of the Barium ion limits acceptable buffer gas species to inert noble gases, which, in addition to not bonding chemically with the Barium, also have simplified interaction potentials, due to the lack of rotational degrees of freedom. Previous work has relied on the fact that the dominant long range interaction is the attractive $1/r^4$ potential generated by the dipole moment induced by the charged ion on the neutral atom to define a "hard-sphere" cross-section [39], wherein a test is performed to determine if a collision occurs in a given time-step, and if so, the scattering angle in the center of mass (CM) frame is taken from a uniform distribution. This is done both for speed of calculation and because direct integration of the scattering angle requires knowledge of the full interaction potential, but this technique, by its nature, underestimates the frequency of collision and gives an incorrect distribution of scattering angles. Both of these factors may influence estimations of cooling rates and ion stability in buffer gas environments. New *ab initio* calculations of the interaction potentials between Barium ions and the rare gases have been recently published [9], and are used in this work to perform ion trajectory simulations.

3.2.1 Ion scattering calculations with a realistic potential

For a given interaction potential $V(r)$ between two particles of masses m_1 & m_2, the scattering angle in the center of mass frame can be classically calculated as a function of the impact parameter of the collision, and the CM collision energy:

$$E = \frac{1}{2}\frac{m_1 m_2}{m_1 + m_2}\left|\vec{v_1} - \vec{v_2}\right|^2, \tag{3.18}$$

by performing the following integration:

$$\Theta(b, E) = \pi - 2b\int_{r_o}^{\infty}\left[1 - \frac{b^2}{r^2} - \frac{V(r)}{E}\right]^{-1/2}\left(\frac{1}{r^2}\right)\mathrm{d}r, \tag{3.19}$$

where the lower-bound of the integral, r_0, is the minimum separation distance between the ion and the neutral atom during the collision [40]. The distance of closest approach can be found by obtaining the radial component of the ion's momentum as a function of r,

$$p_r(r) = \pm p_0\left[1 - \frac{b^2}{r^2} - \frac{V(r)}{E}\right]^{1/2}, \tag{3.20}$$

and solving for $p_r(r_0) = 0$, selecting the most positive root as the lower bound of the integration in Equation 3.19.

In order to perform the integration in Equation 3.19 (or indeed calculate the integral's lower bound in Equation 3.20) an analytical form for $V(r)$ must be sought. McGuirk et al. calculate the interaction potential between Ba^+ ions and rare gas atoms for discrete separation distances between 1.5 and 50 Angstroms, but do not

Gas Species	C_{12} (eV Å^4)	D (eV)	a (Å^{-1})	r_0 (Å)
Helium	2.14×10^2	2.70×10^{-3}	8.79×10^{-1}	5.04
Neon	1.41×10^2	8.72×10^{-3}	8.06×10^{-1}	4.24
Argon	2.20×10^3	9.33×10^{-2}	1.10	3.59
Krypton	4.82×10^3	1.45×10^{-1}	1.12	3.63
Xenon	5.82×10^3	2.16×10^{-1}	1.13	3.76
Radon	1.12×10^4	2.58×10^{-1}	1.10	3.80

Table 3.1: Parameters resulting of fitting *ab initio* Ba^+-rare gas interaction potentials to the empirically selected function form given in Equation 3.22

provide a well-fitting analytical model [9]. A popular choice of interaction potential model, the n-6-4 model, fails to simultaneously fit the short-range repulsion and the depth of the intermediate region where the repulsion gives way to the attraction due to the induced dipole. A Morse potential,

$$V(r) = D\left(1 - e^{a(r_0 - r)}\right)^2 \tag{3.21}$$

models the intermediate and long-range potentials well, but fails to model the short-range repulsion. A hybrid model, which includes a C_{12}/r^{12} term from the n-6-4 model, and the Morse potential, however, improves the fit, though in the cases of Helium and Neon the fit potential is harder than that predicted by the *ab initio* calculations:

$$V(r) = \frac{C_{12}}{r^{12}} + D\left(-1 + \left(1 - e^{a(r_0 - r)}\right)^2\right). \tag{3.22}$$

For the purposes of fitting, each point is assumed to have a relative error of 10%. The values calculated by McGuirk et al. [9], with fits applied, are shown in Figures 3.4 and 3.5, and the fit parameters are summarized in Table 3.1.

The scattering angle is plotted as a function of impact parameter and collision energy for Helium, Neon, Argon, and Xenon in Figure 3.6, using the potential model in Equation 3.22, and fit parameters listed in Table 3.1. At high energies (>10eV) the collision approximates a hard-sphere scattering. As the collision energy is reduced,

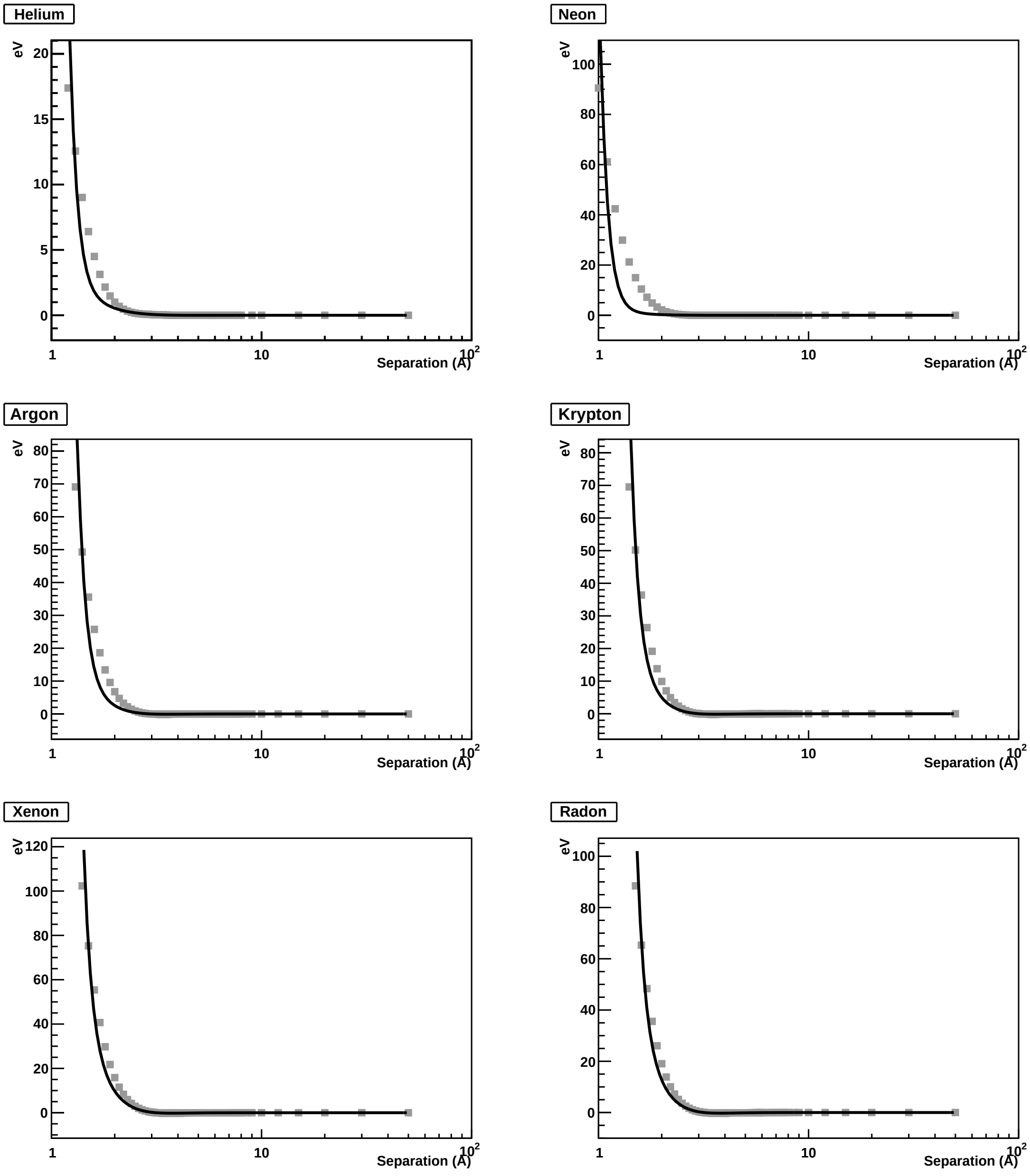

Figure 3.4: Calculated ion-rare gas interaction potentials, fit to an empirically chosen analytical model. Grey boxes denote calculated values from McGuirk et al. [9]; black curves are associated fits.

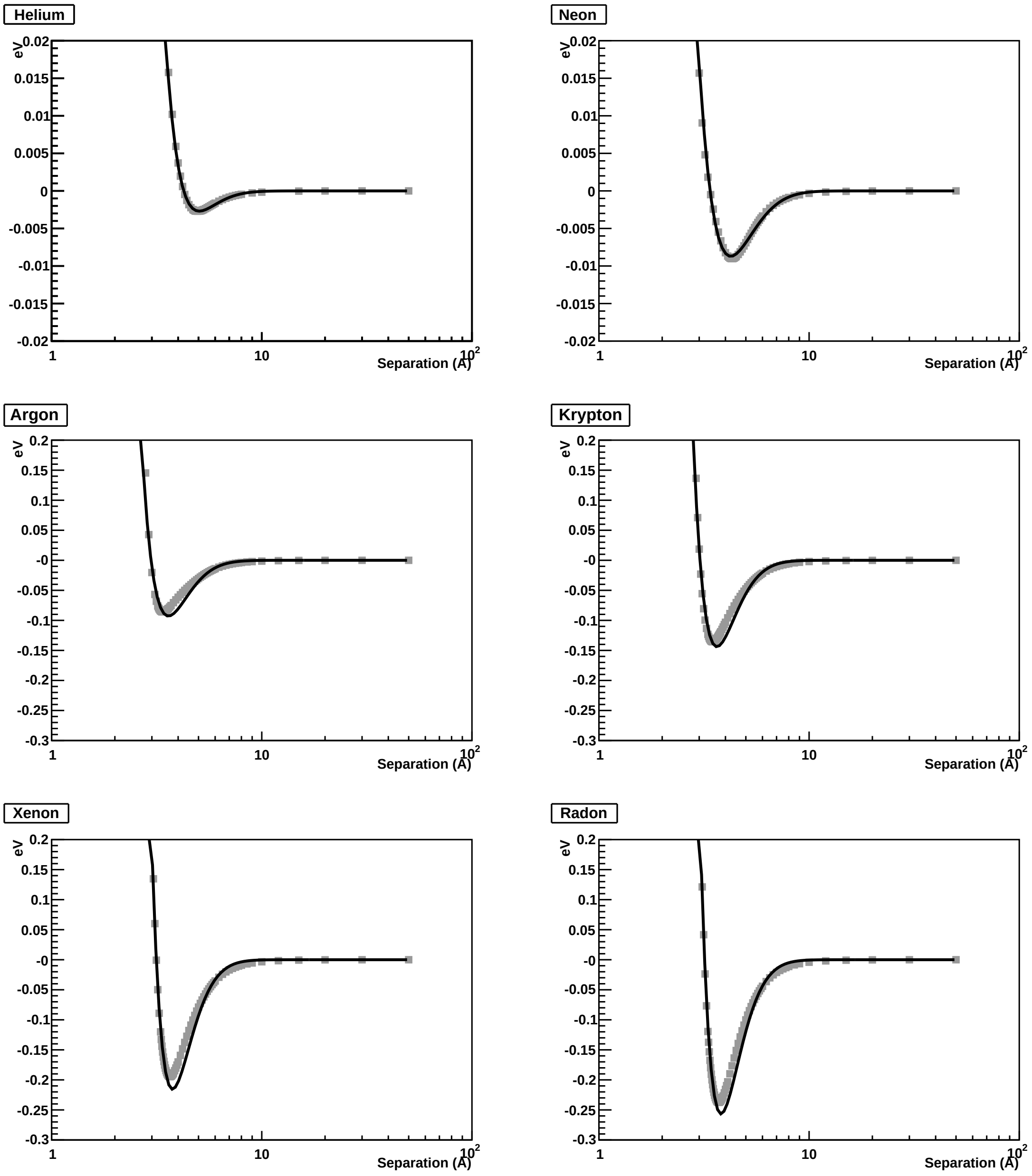

Figure 3.5: Same as Figure 3.4, with Energy axis expanded. Grey boxes denote calculated values from McGuirk et al. [9]; black curves are associated fits. The model of eqn 3.22 approximates well the calculated interaction potentials at low energies.

the attractive potential is capable of producing large-angle deflections at impact parameters that would be "glancing" in a hard-sphere case. Over the full energy range plotted, $E = 10^{-3} - 10^{3}$ eV, the scattering angle is negligible ($< 1.5 \times 10^{-7}$ rad) for impact parameters greater than 25 Å; this will produce a scattering cross section to be used in ion trajectory simulations.

3.2.2 Simulation of ion-neutral collisions in SIMION8

Unfortunately, the scattering angle integral in Equation 3.19 is not in general analytically solvable, and computationally expensive numerical integration methods must be used. In order to reduce simulation time, we follow the example of Kim [41], and compute scattering angles for a range of energies and impact parameters in advance, and place these values into a look-up table which is accessible by SIMION8 at run-time. The strategy for simulating a collision event is as follows:

Computing the mean free path

As mentioned in the previous section, the scattering angle is negligible above 25Å for energies above 10^{-3}eV in collisions involving each rare gas species. This value can then be used as a maximum interaction radius from which a cross-section can be defined:

$$\sigma = \pi r_{max}^2 = 1.96 \times 10^{-13}\text{cm}^2. \tag{3.23}$$

The calculation of the mean free path in the gas is complicated by the thermal motion of the buffer gas molecules. The mean free path is the ratio of the ion's speed c_{ion} and the frequency of collisions, f_{col}:

$$\lambda = c_{ion}/f_{col}. \tag{3.24}$$

The frequency of the collision is given as the product of the mean collisional speed c, the collision cross-section, and the number density of scatterers:

$$f_{col} = c\sigma n, \tag{3.25}$$

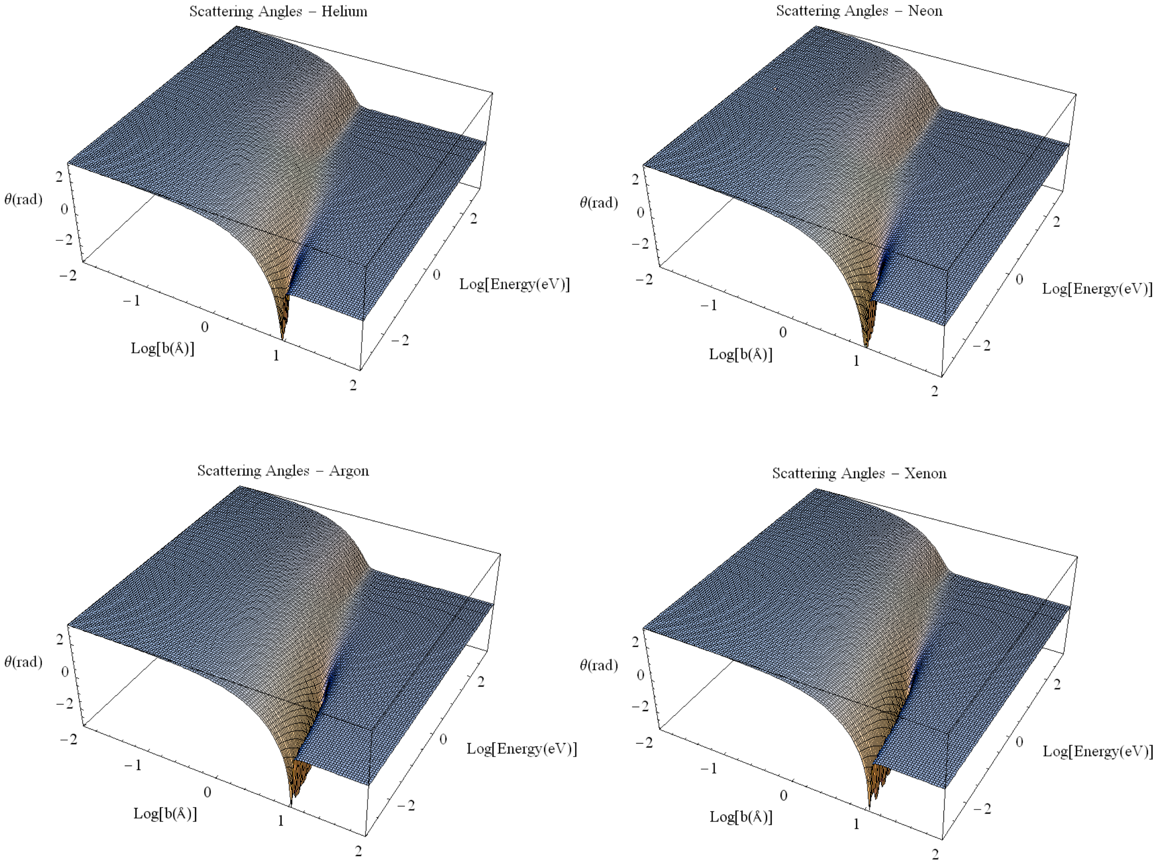

Figure 3.6: Angle of deflection in the center of mass frame as a function of impact parameter and collision energy for Barium ions on Helium, Neon, Argon and Xenon. High-energy collisions resemble hard-sphere scatterings, low-energy collisions can result in large-angle scatterings even at “glancing” impact parameters.

where the mean collisional speed must be calculated by integrating the magnitude of the relative ion-gas velocity over all possible buffer gas velocities, weighted by their probabilities, as given by the Maxwell-Boltzmann distribution:

$$c = \int_V |\vec{v}_{ion} - \vec{v}_{gas}|\, P(\vec{v}_{gas}) d^3\mathrm{v}_{gas}; \tag{3.26}$$

$$P(\vec{v}_{gas}) = \left(\frac{m_{gas}}{2\pi kT}\right)^{3/2} \exp\left(\frac{-m_{gas}\left|\vec{v}_{gas}\right|^2}{2kT}\right). \tag{3.27}$$

Testing for collision

The mean free path is calculated at every time-step of the simulation, and is used to determine the probability for collision in that time-step:

$$P_{col} = 1 - \exp\left(-c_{ion}\delta t/\lambda\right). \tag{3.28}$$

A random number is generated from a uniform distribution between zero and one, and if it is less than P_{col}, a collision is generated. The velocity of the gas molecule is chosen by selecting a velocity at random from a three-dimensional Maxwell-Boltzmann distribution, and then accepting that velocity with a likelihood proportional to the magnitude of the relative velocity.

Calculating scattering angles

With the ion and gas molecule velocities determined, the frame is translated so that the gas molecule is stationary, rotated so that the ion motion is along the z-axis, and then translated along the z-axis into the center of mass frame. The collision energy is calculated using the formula in Equation 3.18, and the impact parameter is the distance from center of a random point on a circle with a 25 Angstrom radius. The probability density function for a randomly chosen impact parameter b should be linear in b, as it is proportional to the area of a ring of radius b and width $b+\delta_b$. This is a special case of the Triangular Distribution [42]. Taking randomly generated numbers from a uniform distribution between 0–1 and applying the inverse of the cumulative distribution function will yield random numbers with the desired distribution [43]:

$$\begin{aligned} \text{PDF} &: \frac{2b}{(25\ \text{Å})^2} \\ \text{CDF} &: \frac{b^2}{(25\ \text{Å})^2} \\ b &= \sqrt{rand(0,1)} \times 25\ \text{Å}. \end{aligned} \tag{3.29}$$

With the collision energy and impact parameter selected, the polar CM scattering angle is chosen by interpolating between the calculated points in the look-up table, and an azimuthal angle is assigned from a uniform distribution between zero and 2π. With the ion's center of mass motion determined, the system is translated back into the laboratory frame by undoing the transformations above.

3.3 Ion slowing and storage in inert buffer gases

For the purposes of this work, the effect of buffer gases on ions are examined in two regimes: first, the ability of a buffer gas to cool an ion injected from an external probe will be studied, and second, the effect on a cooled and stored ion will be investigated. In both cases the behavior of the confined ion varies significantly as a function of buffer gas mass.

3.3.1 Buffer gas cooling of injected ions

Extended linear traps, such as the one shown in Figure 3.7, have been used by a number of groups for the purposes of ion cooling and bunching[44][45]. Ions are injected axially, and make repeated traversals of the trap's length while collisions with a room-temperature or cooled buffer gas dissipate the ion's kinetic energy. The "ski-jump" DC potential configuration guides ions to a minimum where they're confined and released as a cooled bunch as in [41], or as is the case in this work, counted through resonant fluorescence spectroscopy. The simulated cooling of an ion injected into a linear trap filled with 1.0×10^{-3} Torr Helium buffer gas is shown in Figure 3.8.

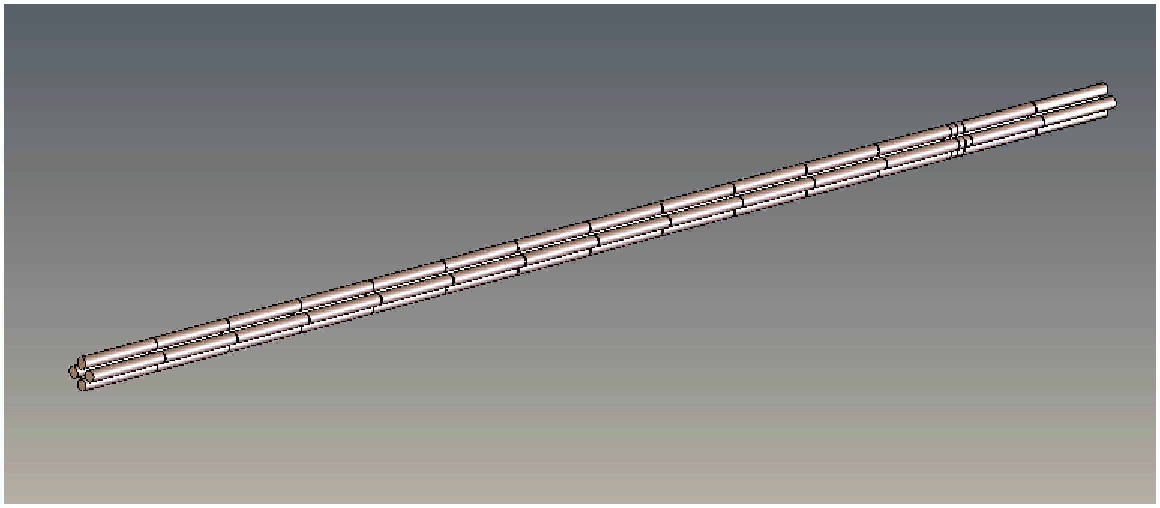

Figure 3.7: An extended linear trap for ion cooling by an inert buffer gas

The simulated linear trap (a SIMION8 model of the trap to be detailed in Chapter 5) is divided into 16 segments over its 70 cm length, with the following DC potentials applied, in volts:

$$U_{DC} = 0, -0.25, -0.50, -0.75, ... - 2.75, -3.0, -10, -3.0, +10. \tag{3.30}$$

The ion's kinetic energy is plotted as a function of time in (a), and axial position in (b). Collisions on the room-temperature He atoms cause instantaneous drops in the ion's energy until it is cooled enough to be captured in the potential minimum at the fourteenth segment. Helium's relatively small mass compared to that of the Barium limits its capacity to effect a large momentum or energy change in the Barium ion, and so a large number of collisions (~ 2500 in the case of the ion shown in Figure 3.8) are required to cool the ion to confinement. Simulation of 25 injected ions with 5 eV initial kinetic energy shows an average time for cooling and confinement in the detection region of 7600 μsec at $1{\times}10^{-3}$ Torr. Once captured, the ion is cooled further, approaching thermal energies over the course of several msec.

The same simulation is repeated for Argon buffer of the same pressure in Figure 3.9. The kinematics of collisions on the heavier Argon cause a more rapid dissipation of the energy of the injected ion. More of the ion's energy is lost in each collision,

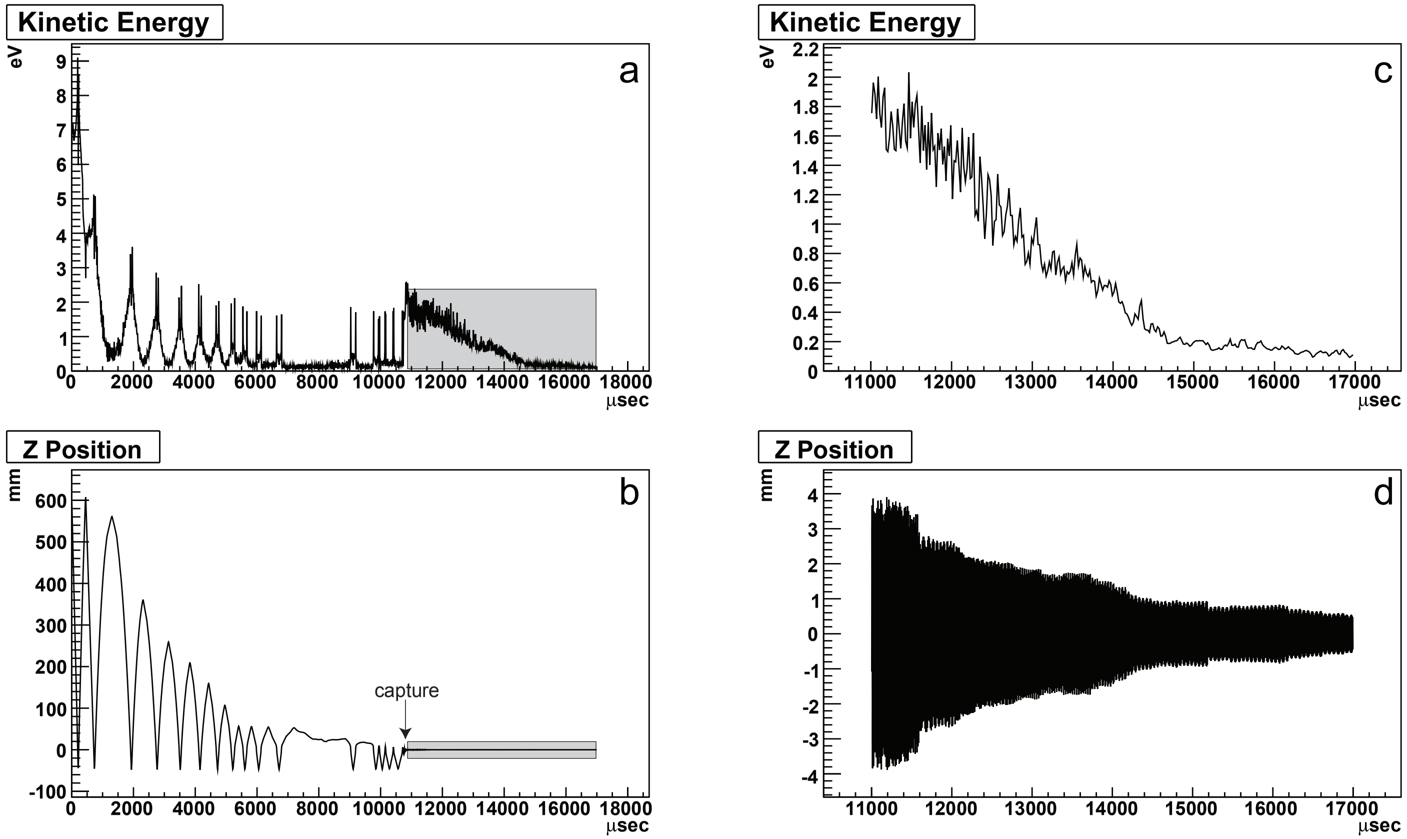

Figure 3.8: Simulated cooling of an injected ion in $1{\times}10^{-3}$ Torr Helium gas. The ion's kinetic energy is plotted as a function of time in (a), and axial position in (b). The ion is cooled as it makes several traversals of the trap, until it is captured in segment 14. Plots c) and d) show the further cooling of the captured ion, with the ion approaching thermal energies over the course of several msec

and the frequency of large angle scattering collisions is increased relative to that of the Helium buffer due to the Argon's larger polarizability increasing the strength of the attractive potential. Repeated simulated injection of 25 5 eV injected ions show and average time to capture in segment 14 of 1850 μsec, over 4 times faster than in Helium of the same pressure.

An ion is injected into a linear trap filled with 1.0×10^{-3} Torr of Xenon gas in Figure 3.10. The Xenon atom's near-equal mass to that of the Ba ion should make it an efficient cooling medium, and in fact the ion's kinetic energy from injection is dampened in less than a single pass. In fact, repeated simulations of injected 5 eV ions show an average settling time of 3200 μsec, longer than in Argon due to the fact that the ions are cooled quickly, and so take longer to actually reach segment 14. There is a risk, however, of imparting a large momentum change to the ion which can redirect the ion's axial kinetic energy component into the radial direction. As the radial confinement is weaker, this can potentially eject the ion. The ion in Figure 3.10 is cooled successfully, but is subsequently unloaded by a series of heating collisions with the Xenon. Buffer gases with molecular masses approaching or exceeding that of the injected ion are thus not suitable for cooling, and even a limited presence in a buffer gas dominated by another species may reduce capturing efficiency.

3.3.2 Ion storage in a buffer gas

While the cooling of ions injected into a linear RF trap is a relatively rapid process on laboratory timescales, detection of confined ions may take several seconds or more, undergoing tens of thousands of gas collisions per second. For a classical 3-dimensional harmonic oscillator[1] of mass m in thermal equilibrium with a gas of temperature T, the positions and velocities along each axis are be distributed according to the

---

[1] $kT \gg \hbar\omega$, $T \gg 10$ μK for the parameters of §3.1.4

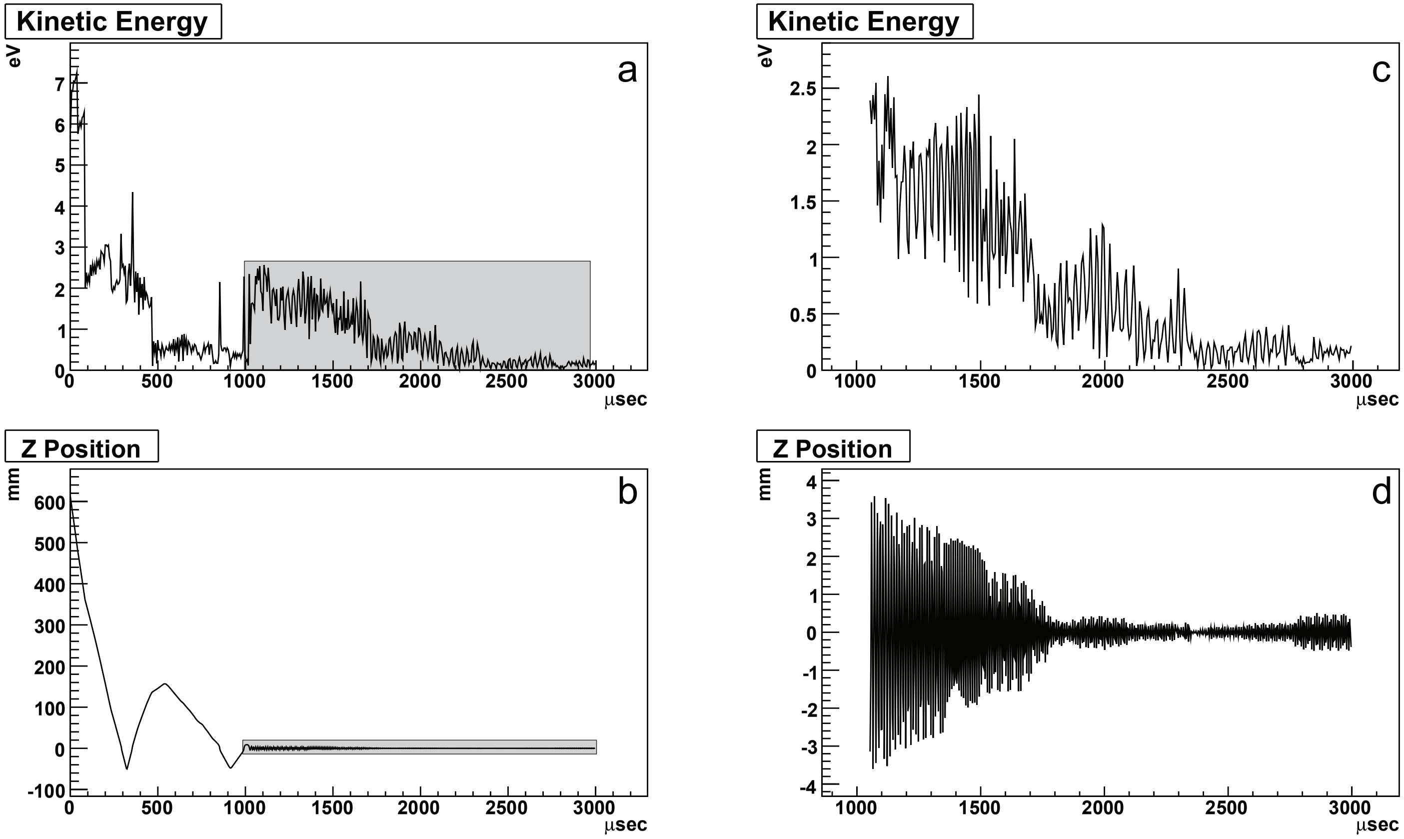

Figure 3.9: Longitudinal position and ion kinetic energy vs time for a Ba^+ ion in the presence of Argon buffer gas. This ion is cooled in less than two passes, much faster than in Helium.

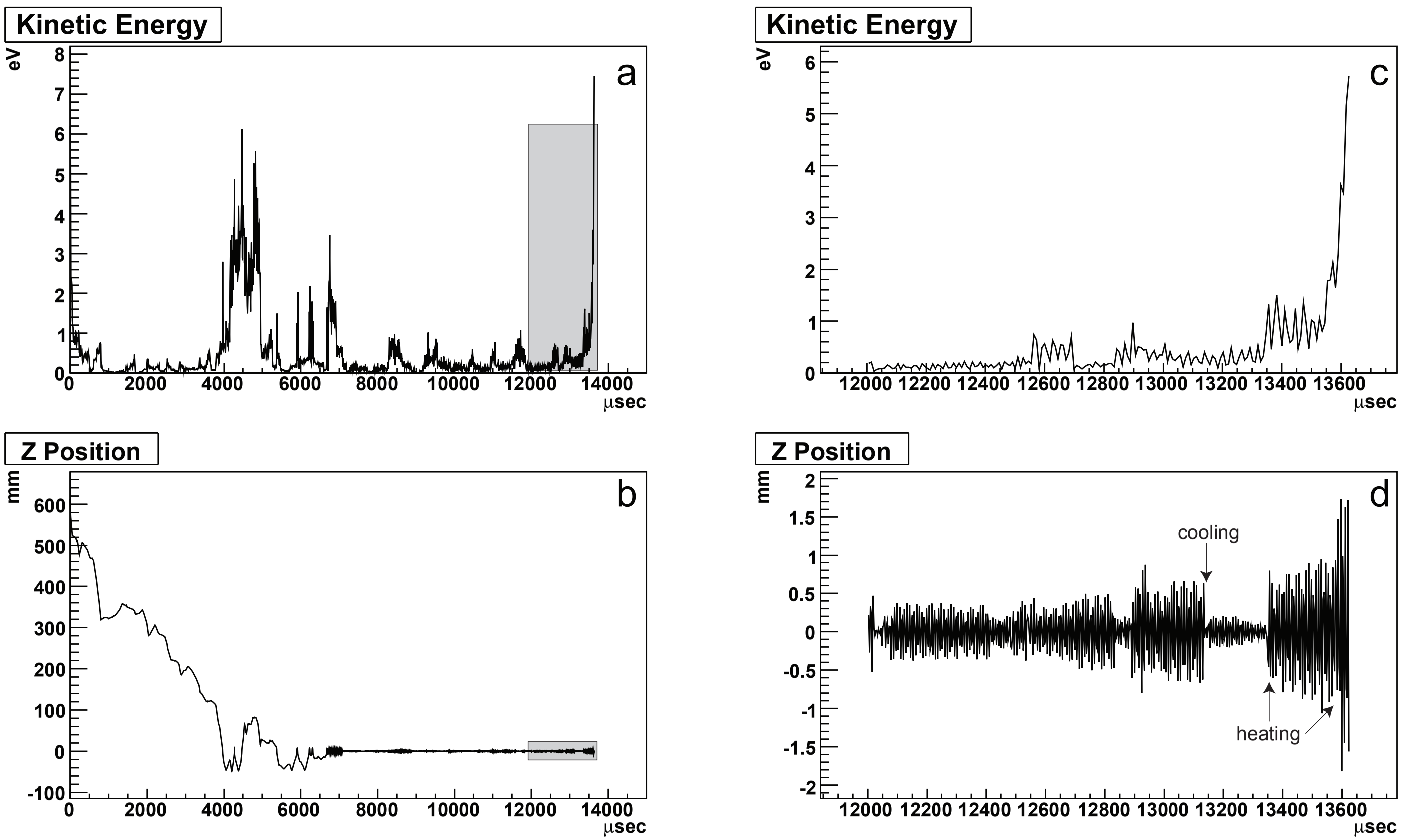

Figure 3.10: Longitudinal position and total ion kinetic energy vs time for a Ba^+ ion in the presence of Xe buffer gas. The ion is slowed quickly, but collisions with neutral Xe cause large velocity changes, leading to the unloading of this cooled ion. Heating can be seen in d), where single collisions can cause energy changes of $\sim$1 eV.

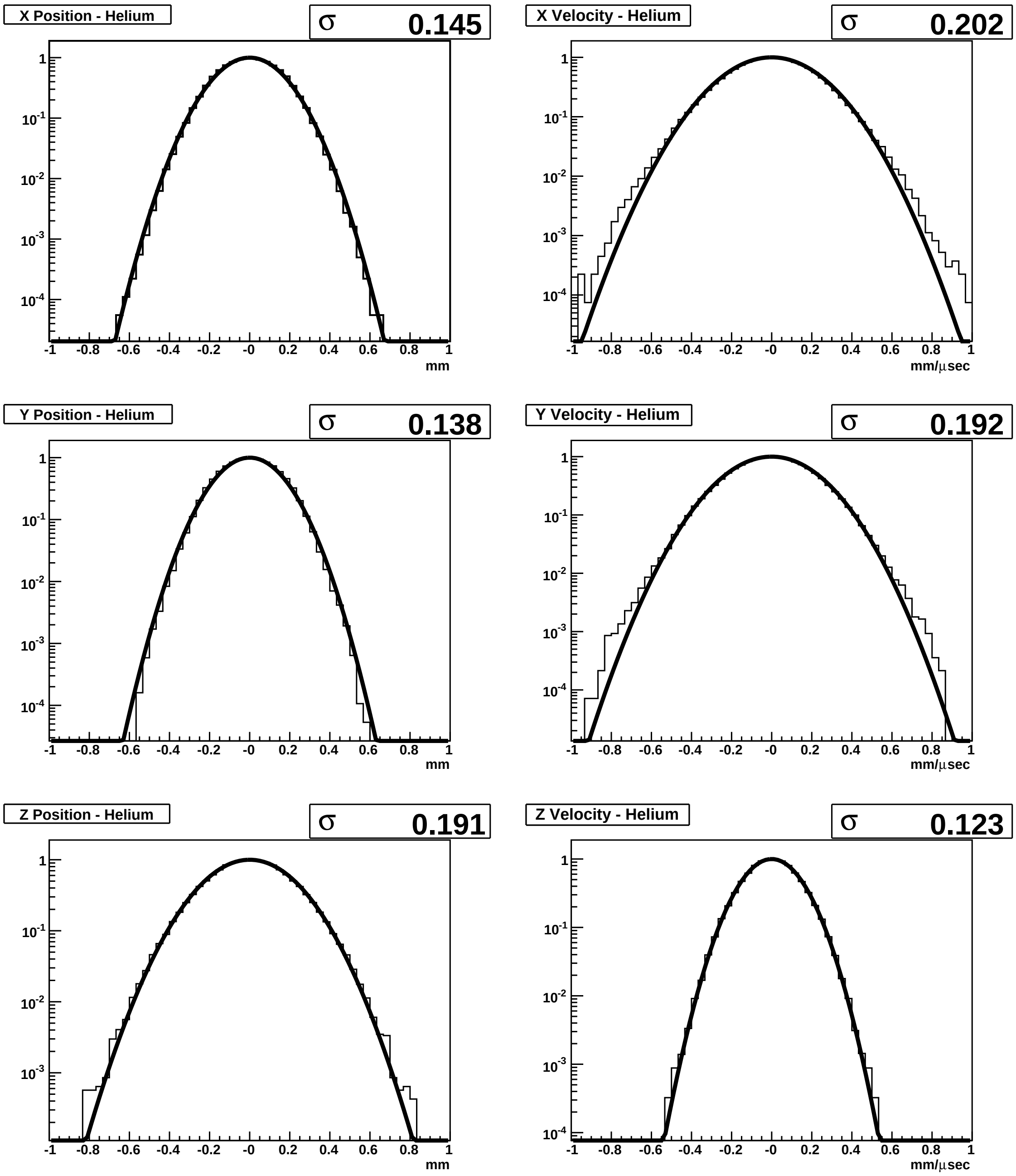

Figure 3.11: Simulated position and velocity distributions for Helium buffer gas cooled ions in a linear trap, generated using SIMION8. The ion's micromotion leads to a deviation from a Gaussian velocity profile along the x- and y-axes, not present in the z-axis motion.

Maxwell distribution:

$$f(x) = \sqrt{\frac{m\omega_x^2}{2\pi kT}} \exp\left(\frac{-m\omega_x x^2}{2kT}\right) \tag{3.31}$$

$$f(v_x) = \sqrt{\frac{m}{2\pi kT}} \exp\left(\frac{-mv_x^2}{2kT}\right). \tag{3.32}$$

These are simply Gaussian distributions with widths $\sigma_x = \sqrt{\frac{kT}{m\omega_x^2}}$; $\sigma_{v_x} = \sqrt{\frac{kT}{m}}$, and while the position distributions depend on the confining potential of their respective axes, the velocity distributions are identical, and depend only on the oscillator mass and the temperature of the buffer gas [46].

An RF quadrupole trap is, however, not the static conservative potential of a 3-dimensional harmonic oscillator. Major and Dehmelt first described the exponential "RF Heating" of ions in the presence of a buffer gas with mass greater than that of the trapped ion [47]. Loss of ions trapped in the presence of a heavy buffer gas have been believed to be due to the tails of the Boltzmann distribution [48]. Recent computational simulations have disagreed with this view, however [49][50]. In the course of a collision, ions are capable of extracting energy from the RF field by instantaneously changing even just the direction of their velocity. To put it another way, ions which originate at the same location, with the same speed, at the same RF phase can follow orbits of significantly differing total energies, if they begin by traveling in different directions. In the course of a collision with a buffer gas molecule, there is an effectively instantaneous (on the time scale of an RF period) velocity change. For light buffer gases ($m_{gas} < m_{ion}$), the change in velocity brought about by any given collision is small. In the case of buffer gas molecules whose mass is comparable to, or exceeds that of the ion ($m_{gas} \sim m_{ion}$, $m_{gas} > m_{ion}$), the instantaneous velocity change can be significant, and the instantaneous change of the ion's effective total energy can be significantly larger than kT. Additionally, it should be noted that even the presence of a light buffer gas has an effect on the region of stability shown in Figure 3.2, reducing the parameter space over which ions can be stabily confined [51].

Figure 3.12 shows the z-position and velocity distributions for ions stored in Helium, Argon, and Xenon, each buffer gas at 273 K and 1 mTorr. A Barium ion at

273 K should yield a velocity distribution with width $\sigma_{v_z} = 0.128$ mm/μsec. Ions confined in Helium and Argon gases replicate this in the simulation, while ions confined in the Xenon gas do not. Not only is the Gaussian width of the Xenon distribution larger than would be expected for an ion at 273 K, but the tails of the distribution are significantly non-Gaussian, showing the power-law drop off described by DeVoe [49]. The z-position and velocity distributions depicted to show that these non-Gaussian tails are not an effect of the RF-drive; they are present even on the axis for which motion is purely harmonic. The non-Gaussian tails of the spatial and velocity distributions cause ions confined in Xenon to spend significant time in large-radius orbits, until they collide with electrodes and are unloaded from the trap. For this particular trap configuration, in 1 mTorr Xenon, a group of 25 ions simulated concurrently were shown to have an average lifetime of just 14 msec, too brief to be detected with high fidelity using the laser-induced fluorescence methods outlined in the following chapter. The Xenon distributions are well fit by a Tsallis distribution (grey curves in figure 3.12), in agreement with DeVoe [49].

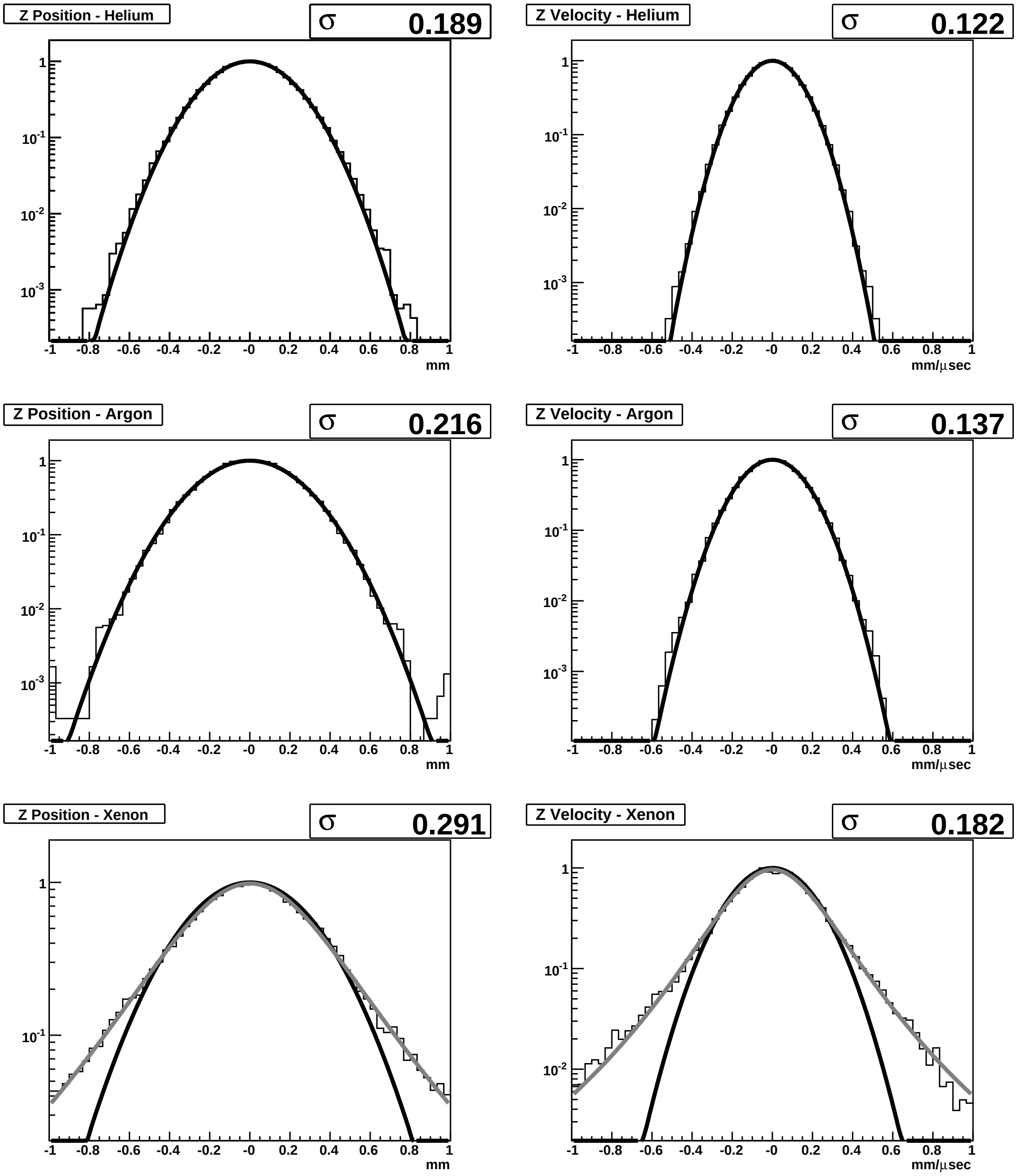

Figure 3.12: Simulated z-position and -velocity distributions for Helium, Argon, and Xenon buffer gas cooled ions in a linear trap. All buffer gases are have a temperature of 273 K and pressure of 1 mTorr, and have been fit to Gaussians (black curves). Power-law tails on the Xenon distributions lead to ion unloading; these are well fit by a Tsallis distribution (grey curves).

Chapter 4

Laser spectroscopy of Ba^+

The true power of ^{136}Xe as a double beta decay source is derived from the strength of the atomic transitions in the (singly-ionized) Ba-II system. The transition amplitudes are large enough that once trapped, single ions can be detected through laser induced fluorescence spectroscopy. The details of the spectroscopy of the Ba-II system are presented here. The level structure and isotope shifts are discussed, and the theory of the spectral lineshape is outlined. Finally, the simulated ion motion is integrated into the fluorescence model.

4.1 Ba-II

The Ba^+ ion is, electronically, a Xe core with a lone 6s electron in the valence shell, the lowest lying energy levels of which are illustrated in Figure 4.1. The n = 5 D-shell is unfilled, and due to its high angular momentum has more energy than the n = 6 S-shell. There is a dipole transition between the 6 $^2S_{1/2}$ and 6 $^2P_{1/2}$ states, at 493.545 nm [5]. The 5 $^2D_{3/2}$ and 6 $^2P_{1/2}$ states are also coupled by an allowed dipole transition at 649.869 nm. The spontaneous emission rates and natural linewidths for these two transitions are shown in Table 4.1. The total spontaneous decay rate from the $^2P_{1/2}$ state is the sum of the rates along these two transitions, and the lifetime of

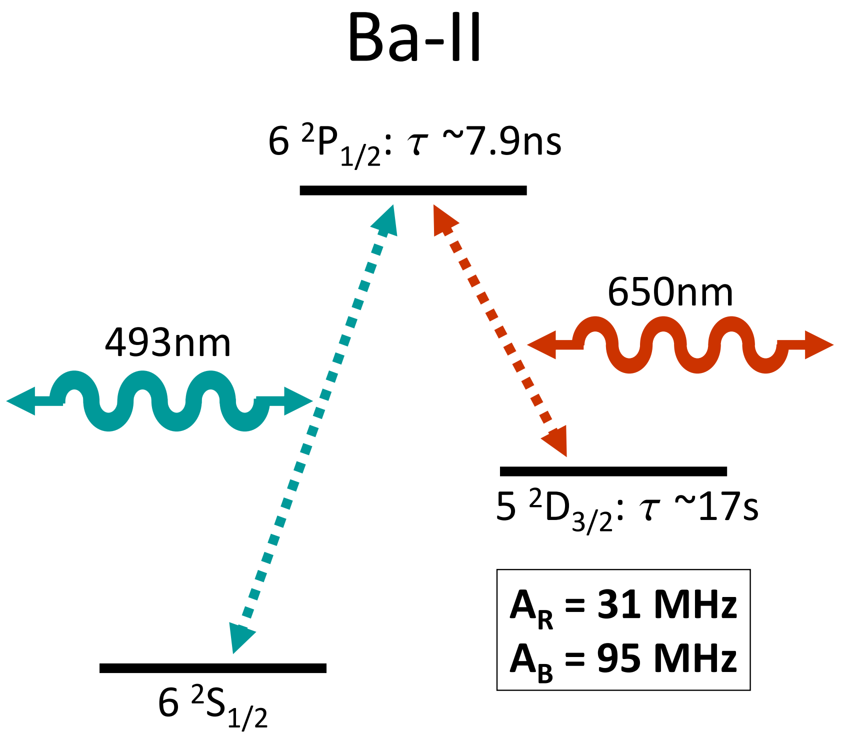

Figure 4.1: The lowest-lying energy states of the Ba$^+$ system.

Transition	λ(nm)	k (cm^{-1})	A (MHz)
$^2P_{1/2}$ - $^2S_{1/2}$	493.545	20261.561	95.3
$^2P_{1/2}$ - $^2D_{3/2}$	649.869	15387.709	31.0

Table 4.1: Ba-II lowest allowed transitions: wavelength (λ), wavenumber (k), spontaneous emission rate / linewidth (A_{ki}) [5].

this upper state is the inverse of this rate,

$$\Gamma_{\text{total}} = \Gamma_{\text{blue}} + \Gamma_{\text{red}} = 126.3 \text{ MHz} = 1/7.92\text{ns}. \tag{4.1}$$

Dipole transitions between the $^2\mathrm{S}_{1/2}$ and $^2\mathrm{D}_{3/2}$ states are forbidden, but quadrupole transitions are allowed; this leaves the $^2\mathrm{D}_{3/2}$ state meta-stable, with a lifetime of 17 seconds [52]. Fluorescence is generated by using a laser field to create an excited state population, which in the absence of magnetic field will then spontaneously emit isotropically in both wavelengths. Both transitions must be driven, else the atom will be pumped into the D state and fluorescence will cease. To fully understand the dynamics of the three level system in the bi-chromatic laser field, its quantum mechanics must be analyzed.

4.2 The three-level system

4.2.1 The Schrodinger Equation and dipole interaction

The derivation of the quantum mechanics of this three-level system presented here is an extension of the two-level formalism outlined by Metcalf & van der Straten [53]. The general quantum state of the atom is a linear superposition of its eigenstates:

$$\Psi(\vec{r}, t) = \sum_k c_k(t)\phi_k(\vec{r})e^{i\omega_k t} \tag{4.2}$$

where the $\phi_k(\vec{r})$ are eigenstates of the time-independent atomic Hamiltonian $\mathcal{H}_0$, in the absence of the laser field, with eigenvalues $\hbar\omega_k$. The presence of the laser field adds a component $\mathcal{H}'(t)$ to the total Hamiltonian, $\mathcal{H} = \mathcal{H}_0 + \mathcal{H}'(t)$. The Schrodinger Equation with this modified Hamiltonian becomes:

$$[\mathcal{H}_0 + \mathcal{H}'(t)]\,\Psi(\vec{r}, t) = (i\hbar)\left(\frac{\partial}{\partial t}\right)\sum_k c_k(t)\phi_k(\vec{r})e^{i\omega_k t}. \tag{4.3}$$

Multiplication by $\psi_j^*(\vec{r})$ and integration over $\vec{r}$ yields:

$$i\hbar \frac{\mathrm{d}c_j(t)}{\mathrm{d}t} = \sum_k c_k(t) \mathcal{H}'_{jk}(t) e^{i\omega_{jk}t}, \tag{4.4}$$

where $\mathcal{H}'_{jk}(t)$ are the elements of the matrix representation of $\mathcal{H}'(t)$, and $\omega_{jk} = \omega_j - \omega_k$. For the case of atom in an electric field $\vec{\mathcal{E}}(\vec{r}, t)$, $\mathcal{H}'(t)$ is given by the electric dipole energy,

$$\mathcal{H}'(t) = -e\vec{\mathcal{E}}(\vec{r}, t) \cdot \vec{r}. \tag{4.5}$$

In the case of a local electric field $\vec{\mathcal{E}}(\vec{r}, t) = E_0 \hat{\epsilon} \cos(\omega_\ell t)$, of amplitude E_0, polarization $\hat{\epsilon}$ and frequency ω_ℓ,

$$\mathcal{H}'_{jk}(t) = \hbar \Omega_{jk} \cos(\omega_\ell t). \tag{4.6}$$

with Rabi oscillation frequency

$$\Omega_{jk} = \frac{-eE_0}{\hbar} \langle j | \, r \, | k \rangle \,. \tag{4.7}$$

4.2.2 The density matrix

In the presence of spontaneous emission, a statistical treatment making use of the density matrix can be used to evaluate the time evolution of the system. The density operator $\rho = |\Psi\rangle \langle\Psi|$ evolves with a time dependence given by the following relation:

$$i\hbar \frac{\mathrm{d}\rho}{\mathrm{d}t} = [\mathcal{H}, \rho] \,. \tag{4.8}$$

For a pure state

$$\Psi = \sum_j c_j \phi_j, \tag{4.9}$$

the elements of matrix representation of the density operator are evidently

$$\rho_{jk} = \langle \phi_j | \, \rho \, | \phi_k \rangle = \langle \phi_j | \, \Psi \, \rangle \langle \, \Psi \, | \phi_k \rangle = c_j c_k^*, \tag{4.10}$$

and so for the three-level system the density matrix takes the following form:

$$\rho = \begin{pmatrix} \rho_{ss} & \rho_{sp} & \rho_{sd} \\ \rho_{ps} & \rho_{pp} & \rho_{pd} \\ \rho_{ds} & \rho_{dp} & \rho_{dd} \end{pmatrix} = \begin{pmatrix} c_s c_s^* & c_s c_p^* & c_s c_d^* \\ c_p c_s^* & c_p c_p^* & c_p c_d^* \\ c_d c_s^* & c_d c_p^* & c_d c_d^* \end{pmatrix}. \tag{4.11}$$

The diagonal elements of the density matrix, ρ_{jj} give the probability of finding the system in state j, while the off-diagonal elements ρ_{jk}, called the coherences, encode the relative phases between states. The matrix is Hermitian, and probability conservation requires

$$\mathrm{Tr}\ \rho = \sum_j \rho_{jj} = 1. \tag{4.12}$$

To evaluate the time-dependent behavior of the system, we need to calculate the time evolution of the elements of ρ. Differentiating Equation 4.11 with respect to time gives

$$\frac{\mathrm{d}\rho_{jk}}{\mathrm{d}t} = \frac{\mathrm{d}c_j}{\mathrm{d}t} c_k^* + c_j \frac{\mathrm{d}c_k^*}{\mathrm{d}t}. \tag{4.13}$$

The time derivatives of the coefficients c_j can be calculated by inserting Equation 4.6 into Equation 4.4

$$\begin{aligned} i\hbar \frac{\mathrm{d}c_s(t)}{\mathrm{d}t} &= c_p(t)\hbar\Omega_{sp}\cos(\omega_B t)e^{i\omega_{sp}t} \\ i\hbar \frac{\mathrm{d}c_p(t)}{\mathrm{d}t} &= c_s(t)\hbar\Omega_{sp}\cos(\omega_B t)e^{i\omega_{ps}t} + c_d(t)\hbar\Omega_{dp}\cos(\omega_R t)e^{i\omega_{pd}t} \\ i\hbar \frac{\mathrm{d}c_d(t)}{\mathrm{d}t} &= c_p(t)\hbar\Omega_{dp}\cos(\omega_R t)e^{i\omega_{dp}t}, \end{aligned} \tag{4.14}$$

and can subsequently be used to calculate the time-dependent behavior of the ρ_{jk}. Here, ω_B and ω_R are used to represent the frequencies of a blue and red laser, respectively. As an example, consider the following calculation of the evolution of one element of the density matrix, ρ_{sp}:

$$
\begin{aligned}
\frac{\mathrm{d}\rho_{sp}}{\mathrm{d}t} &= \frac{\mathrm{d}c_s}{\mathrm{d}t}c_p^* + c_s\frac{\mathrm{d}c_p^*}{\mathrm{d}t} \\
&= \left[-ic_p\Omega_{sp}\cos(\omega_B t)e^{i\omega_{sp}t}\right]c_p^* \\
&\quad + c_s\left[c_s^*\hbar\Omega_{sp}\cos(\omega_B t)e^{-i\omega_{ps}t} + c_d^*\hbar\Omega_{dp}\cos(\omega_R t)e^{-i\omega_{pd}t}\right] \\
&= i\frac{\Omega_{sp}}{2}\left(\rho_{pp}-\rho_{ss}\right)e^{-i\delta_B t} + i\frac{\Omega_{dp}}{2}\rho_{sd}e^{-i\delta_R t} \qquad (4.15) \\
\frac{\mathrm{d}\tilde{\rho}_{sp}}{\mathrm{d}t} &= i\frac{\Omega_{sp}}{2}\left(\rho_{pp}-\rho_{ss}\right) + i\frac{\Omega_{dp}}{2}\rho_{sd} - i\delta_B\tilde{\rho}_{sp}, \qquad (4.16)
\end{aligned}
$$

where $\delta_B = (\omega_B - \omega_{ps})$ and $\delta_R = (\omega_R - \omega_{pd})$, terms oscillating at double the optical frequency have been dropped, and $\tilde{\rho}_{sp}$ is substituted for $\rho_{sp}e^{-i\delta_R t}$. Similar calculations can be made for the other elements of the density matrix.

4.2.3 The Optical Bloch Equations

Up to this point, the quantum mechanical calculations for the time evolution of this system have omitted the effects of spontaneous emission; the density matrix describes a pure quantum mechanical state for the atom. To introduce spontaneous emission, one needs only insert by hand the terms that describe the exponential decay of the excited state along the two branches, with their appropriate rates; the coherences decay with a rate half that of the excited state:

$$\begin{aligned}
\left(\frac{\mathrm{d}\rho_{ss}}{\mathrm{d}t}\right)_{\text{spont}} &= \rho_{pp}\Gamma_B \\
\left(\frac{\mathrm{d}\rho_{pp}}{\mathrm{d}t}\right)_{\text{spont}} &= -\rho_{pp}\left(\Gamma_B + \Gamma_R\right) \\
\left(\frac{\mathrm{d}\rho_{dd}}{\mathrm{d}t}\right)_{\text{spont}} &= \rho_{pp}\Gamma_R. \\
\left(\frac{\mathrm{d}\tilde{\rho}_{sp}}{\mathrm{d}t}\right)_{\text{spont}} &= -\rho_{sp}\frac{\Gamma_B}{2} \\
\left(\frac{\mathrm{d}\tilde{\rho}_{dp}}{\mathrm{d}t}\right)_{\text{spont}} &= -\rho_{dp}\frac{\Gamma_R}{2} \\
\left(\frac{\mathrm{d}\tilde{\rho}_{sd}}{\mathrm{d}t}\right)_{\text{spont}} &= 0.
\end{aligned} \tag{4.17}$$

The combined set of differential equations are known as the Optical Bloch Equations (OBEs) for the the three-level system:

$$\begin{aligned}
\frac{\mathrm{d}\rho_{ss}}{\mathrm{d}t} &= i\frac{\Omega_{sp}}{2}\left(\tilde{\rho}_{sd} - \tilde{\rho}_{ds}\right) + \Gamma_B\rho_{ss} \\
\frac{\mathrm{d}\rho_{pp}}{\mathrm{d}t} &= i\frac{\Omega_{sp}}{2}\left(\tilde{\rho}_{ds} - \tilde{\rho}_{sd}\right) + i\frac{\Omega_{dp}}{2}\left(\tilde{\rho}_{dp} - \tilde{\rho}_{pd}\right) - \left(\Gamma_B + \Gamma_R\right)\rho_{ss} \\
\frac{\mathrm{d}\rho_{dd}}{\mathrm{d}t} &= i\frac{\Omega_{dp}}{2}\left(\tilde{\rho}_{pd} - \tilde{\rho}_{dp}\right) + \Gamma_R\rho_{ss} \\
\frac{\mathrm{d}\tilde{\rho}_{sp}}{\mathrm{d}t} &= i\frac{\Omega_{sp}}{2}\left(\rho_{pp} - \rho_{ss}\right) + i\frac{\Omega_{dp}}{2}\rho_{sd} - i\delta_B\tilde{\rho}_{sp} - \frac{\Gamma_B}{2}\rho_{sp} \\
\frac{\mathrm{d}\tilde{\rho}_{dp}}{\mathrm{d}t} &= i\frac{\Omega_{dp}}{2}\left(\rho_{dd} - \rho_{ss}\right) + i\frac{\Omega_{sp}}{2}\rho_{ds} - i\delta_R\tilde{\rho}_{dp} - \frac{\Gamma_B}{2}\rho_{dp} \\
\frac{\mathrm{d}\tilde{\rho}_{sd}}{\mathrm{d}t} &= i\frac{\Omega_{dp}}{2}\tilde{\rho}_{12} - i\frac{\Omega_{sp}}{2}\tilde{\rho}_{23} + i\left(\delta_R - \delta_B\right)\tilde{\rho}_{13}
\end{aligned} \tag{4.18}$$

The unity trace and hermiticity of ρ limit the number of free parameters to 8, with $\rho_{kj} = \rho^*_{jk}$. The Equations 4.18 can be solved in the steady-state by setting time derivatives to zero, as is done by Janik et al. [54], or can be numerically integrated for arbitrary light intensity sequences (pulsed laser excitation, etc.).

4.3 Spectroscopy of trapped ions

4.3.1 Fluorescence lineshapes

The rate of 493 nm spontaneous emission from an ion at rest is given by

$$F = \Gamma_B \times \rho_{pp}. \tag{4.19}$$

If the blue laser is held at a fixed detuning while the frequency of the red laser is swept over resonance, lineshapes like those plotted in Figure 4.2 are produced. The full-width at half-maximum (FWHM) of the resonance is simply Γ_B in the low-intensity limit. Each of these lineshapes shows an extinction of the fluorescence signal when $\delta_R = \delta_B$; this is representative of optical pumping of the system into a coherent superposition of the ground and metastable states, with no excited state population; when both detunings are equal, population transitions can be made through a virtual state, bypassing the excited state entirely.

The width of the fluorescence resonance depends on the laser intensities. The Rabi oscillation frequency of a transition is related to laser intensity in the following way:

$$I/I_{\text{sat}} = 2\left|\Omega\right|^2/\Gamma^2. \tag{4.20}$$

As the laser intensity is increased past the saturation intensity, the Rabi frequency exceeds the spontaneous emission rate, and the population in the excited state cannot be increased further. The peak value of the excited state population is plotted as a function of blue intensity for several red laser intensities (different values of Ω_R) in Figure 4.3. For laser intensities much above I_{sat}, there is negligible increase in excited state population, and the subsequent fluorescence. As the main source of background in resonance fluorescence experiments is often scattered laser light, which scales linearly with laser power, operating with a laser intensity much above I_{sat} will reduce detection sensitivity. Off resonance, a beam with intensity greater than I_{sat} no longer saturates the transition; increasing the power continues to increase the excited state population off-resonance while the peak intensity remains fixed, widening the peak. This is known as power broadening, and can be seen in Figure 4.4. Fluorescence

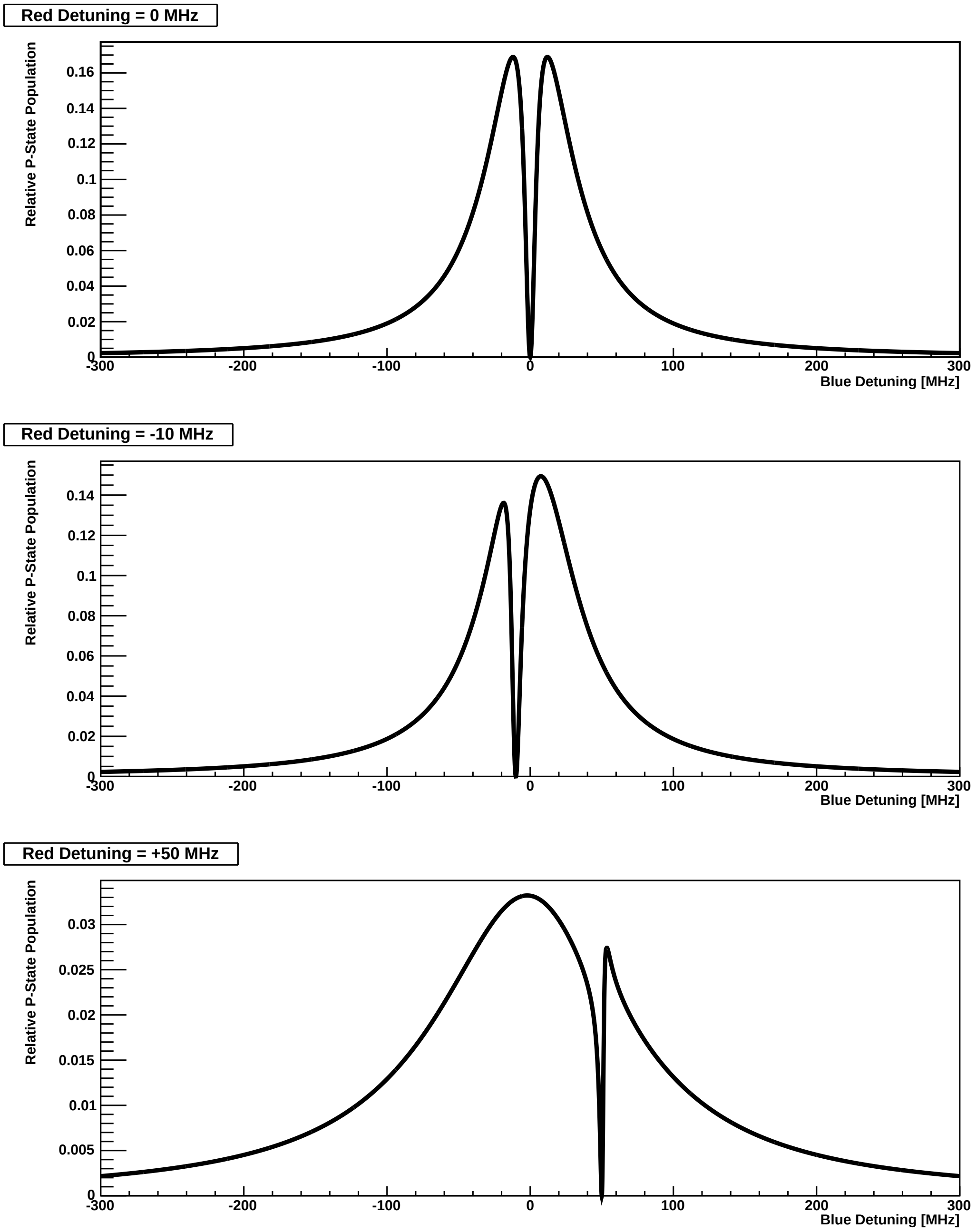

Figure 4.2: Fluorescence lineshapes of Ba$^+$ ions at rest for: a) $\delta_R = 0$; b) $\delta_R = -10MHz$; c) $\delta_R = +50MHz$. Fluorescence extinction occurs when $\delta_B = \delta_R$.

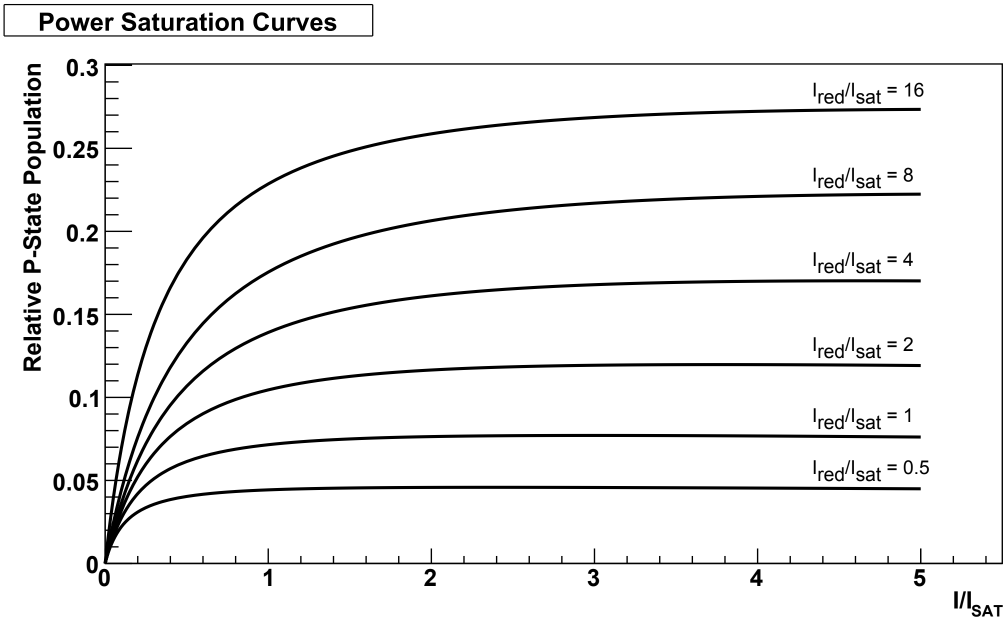

Figure 4.3: The relative excited state population as a function of blue laser intensity for several red laser intensities (differing values of Ω_{dp}). As the intensity exceeds I_{sat} further increase of peak fluorescence is suppressed.

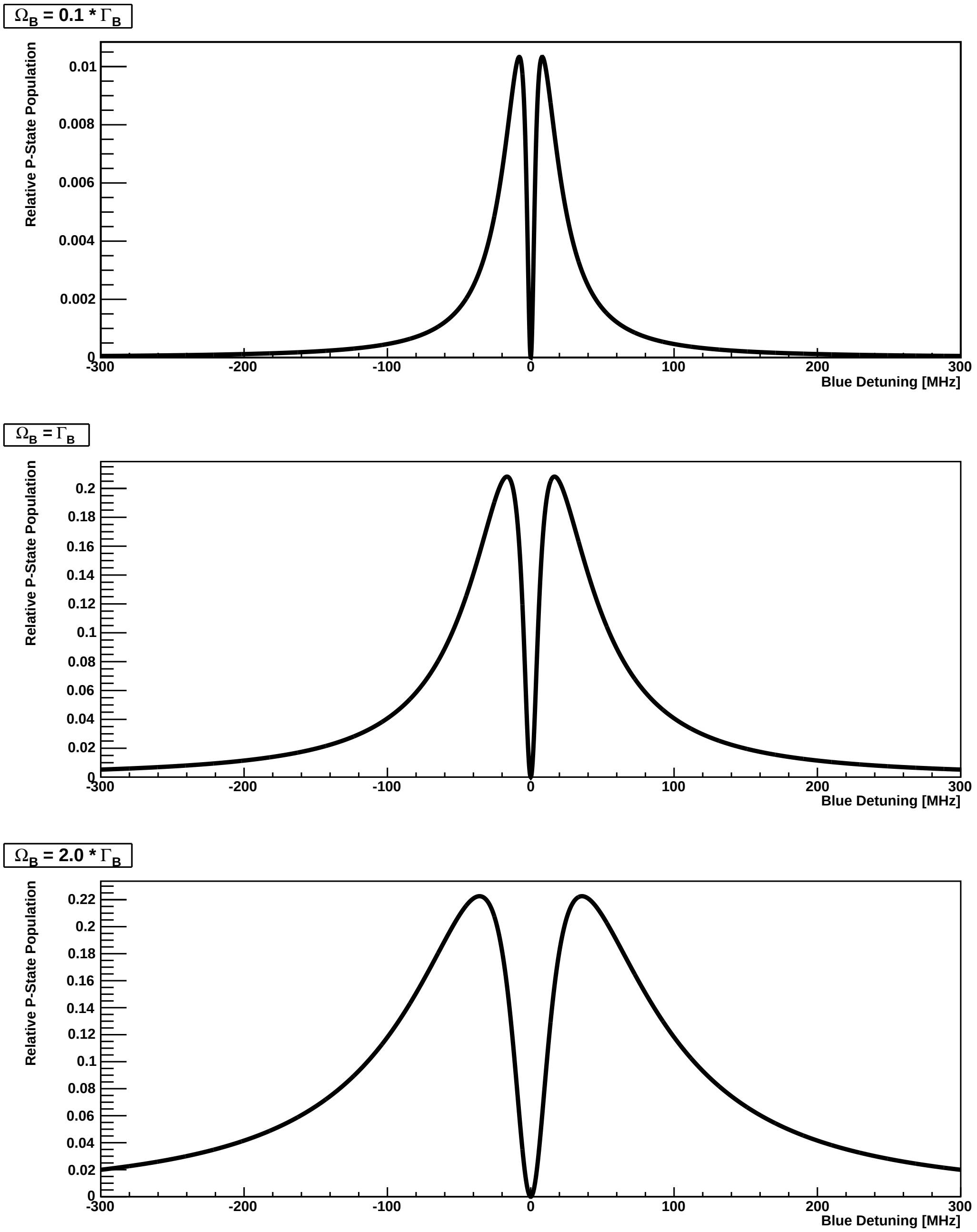

Figure 4.4: Power-broadened lineshapes. As the intensity of the blue laser is increased, so is the width of the blue resonance. For each lineshape $\Omega_{dp} = 2\pi \times 10$ MHz & $\delta_R = 0$.

spectra are plotted for different blue laser intensities, at a fixed red laser intensity such that $\Omega_{dp} = 2\pi \times 10$ MHz with a detuning of $\delta_R = 0$. As the intensity of the blue laser is increased, the width of the lineshape increases from it's natural linewidth of 93 MHz at low intensity ($\Omega_{sp} = 0.1 \times \Gamma_B$) to over 200 MHz as the intensity is increased ($\Omega_{sp} = 2 \times \Gamma_B$).

4.3.2 Doppler broadening

The lineshapes and fluorescence rates calculated so far have been for ions stationary with respect to the laser fields driving them. For an ion in motion, the classical Doppler shift formula describes the modulation of the laser frequency as observed by the ion:

$$\omega_i = \omega_\ell \left(1 - \frac{\vec{v}_i \cdot \hat{k}}{c} \right), \tag{4.21}$$

where ω_ℓ is the laser frequency in the lab frame, $\hat{k}$ is the unit vector along the direction of laser propagation, and $\vec{v}_i$ is the instantaneous velocity of the ion. An intentional red-detuning of either laser from resonance will cause a preferential absorption of photons from the field as the ion is traveling counter to the beam's propagation direction. The momentum of the absorbed photon, $\hbar\vec{k}$, is imparted to the ion, slowing it. Spontaneously emitted photons are distributed isotropically, and so a net cooling of the ion is produced. Doppler cooling is capable of reducing the energy of trapped ions to that of the ground state of the confining potential [55][54].

In the case of ions undergoing frequent collisions with a buffer gas, any effects of Doppler cooling are overwhelmed by the thermal bath of gas molecules in which they reside. Ions are maintained at the temperature of the gas. The ion motion, however, still modulates the frequency of the laser according to Equation 4.21. In order to see the effect this has on the ion fluorescence, the steady-state ion fluorescence equation must be convolved with the ion's velocity distribution along the laser axis, noting that as the ion moves along the z-axis *both* lasers are Doppler shifted, applying Equation 4.21 for the different laser frequencies. If the steady-state ion excited state population is described by a function $\mathcal{F}_{nat}(\delta_B, \delta_R) = \rho_{pp}$, and $P(v_z)$ is the ion velocity's probability distribution function, then the Doppler-broadened excited state population can be calculated by performing the following integral:

$$\mathcal{F}_{dopp}(\delta_B, \delta_R) = \int_{-\infty}^{+\infty} F_{nat}(\delta_B - \frac{\omega_B}{c} v_z, \delta_R - \frac{\omega_R}{c} v_z) P(v_z) dv_z. \tag{4.22}$$

In the case of an ion confined in a harmonic potential at a temperature T, the velocity distribution along the laser propagation axis (here labeled the z-axis) is given by the Maxwell-Boltzmann distribution:

$$P(v_z)\mathrm{d}v_z = \sqrt{\frac{m}{2\pi kT}} \exp\left(\frac{-mv_z^2}{2kT}\right) \mathrm{d}v_z, \tag{4.23}$$

a Gaussian distribution centered at $v_z = 0$, of width $\sigma = \sqrt{(}kT/m)$. Combining Equations 4.21 & 4.23, and noting that

$$\mathrm{d}v_z = (\mathrm{d}v_z/\mathrm{d}\omega_i)\,\mathrm{d}\omega_i = \left(\frac{c}{\omega_\ell}\right) \mathrm{d}\omega_i, \tag{4.24}$$

yields the following probability distribution of laser frequencies observed by the ion:

$$P(\omega_i)\mathrm{d}\omega_i = \sqrt{\frac{mc^2}{2\pi kT\omega_\ell^2}} \exp\left(-\frac{mc^2\left(\omega_i - \omega_\ell\right)^2}{2kT\omega_\ell^2}\right) \mathrm{d}\omega_i. \tag{4.25}$$

The Doppler-broadened lineshape is calculated using this distribution, and effects of differing laser powers and ion temperatures are shown in Figure 4.5. The first thing to note is that while the ion's motion yields a frequency probability distribution (Equation 4.25 that is a Gaussian with a width of 271 MHz for the blue laser (607425.5 GHz), the combined lineshape is significantly narrower than this. This is an effect of the simultaneous Doppler shifts of both lasers; if the convolution of Equation 4.25 is performed without varying both frequencies (as in [50] & [6]) the combined lineshape is broader than the gaussian distribution as expected. The simultaneous detuning of both lasers by the ion motion, by different absolute detunings ($\delta'_R = \omega_R/\omega_B \times \delta'_B$) ensures that both lasers can only address the same ion if it is

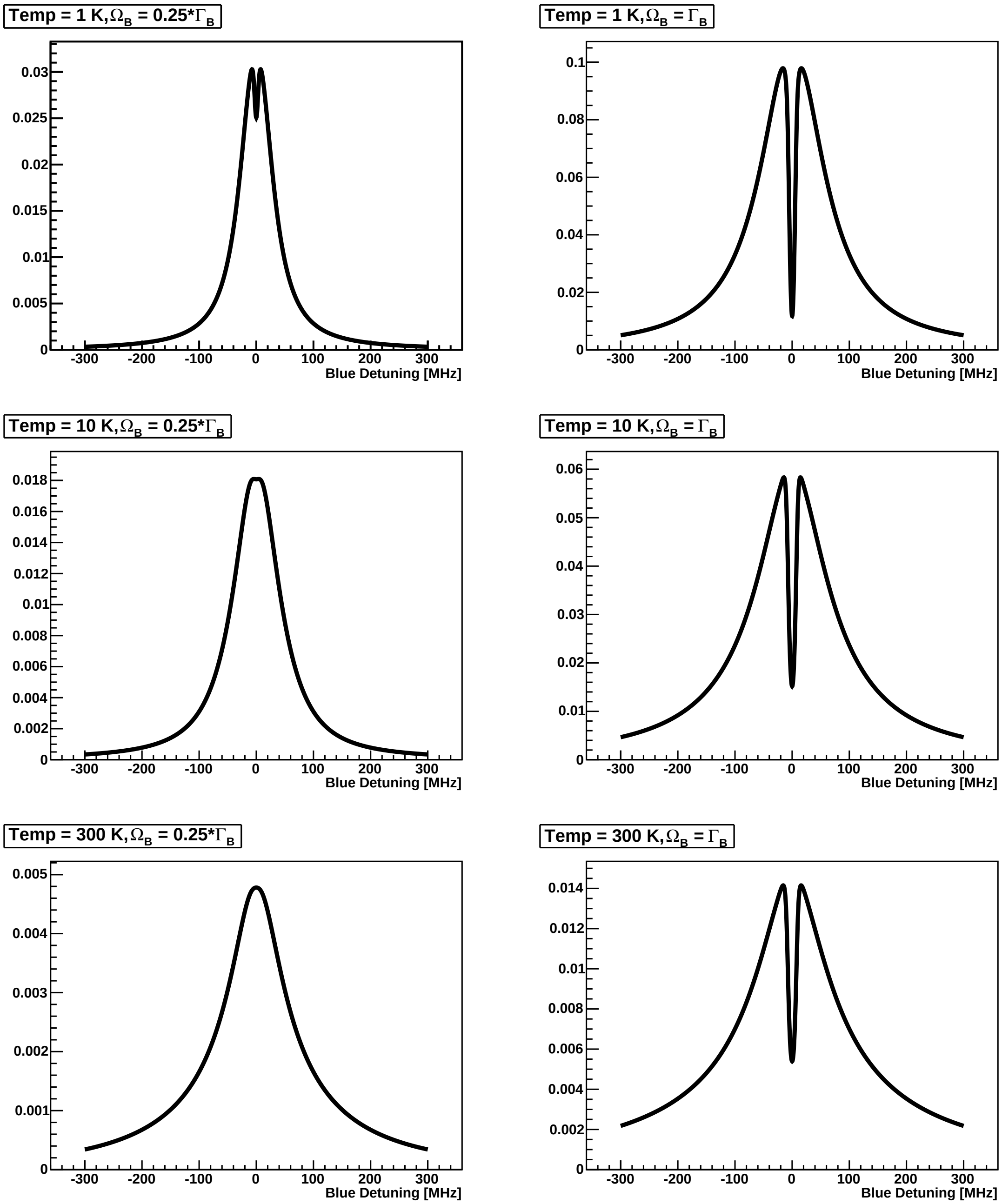

Figure 4.5: The Doppler- and power-broadened lineshapes for a single Ba$^+$ at different laser powers and temperatures. The modulation of both lasers simultaneously by the ion's motion keeps the Doppler widths narrow.

stationary, to within the natural linewidth. This causes a narrowing of the Doppler-broadened shape to a width not much larger than the natural linewidth, albeit with substantially reduced excited state population.

The fluorescence lineshape expected from an ion confined in the linear RF trap described in §3.3.2 can be calculated by substituting simulated trapped ion velocity profile shown in Figure 3.12 for the Maxwellian distribution of Equation 4.23. In the cases of ions stored in Helium and Argon, this would be nearly equivalent to substituting the widths of the simulated velocity distributions shown in Figure 3.11 for the prescribed width of $\sqrt{(kT/m)}$ in Equations 4.23 & 4.25. In the case of ions stored in the heavier Xenon buffer gas, however, the velocity distribution is significantly non-Maxwellian, and the simulated distribution must be used in the convolution directly. The results of the linewidth calculations using the simulated ion velocities are plotted in Figure 4.6. There is little change in the widths of the spectra, owing to the mechanism described above. There is, however a significant reduction in excited state population for ions trapped in Xenon, due to the ion's higher likelihood of being found with large velocities.

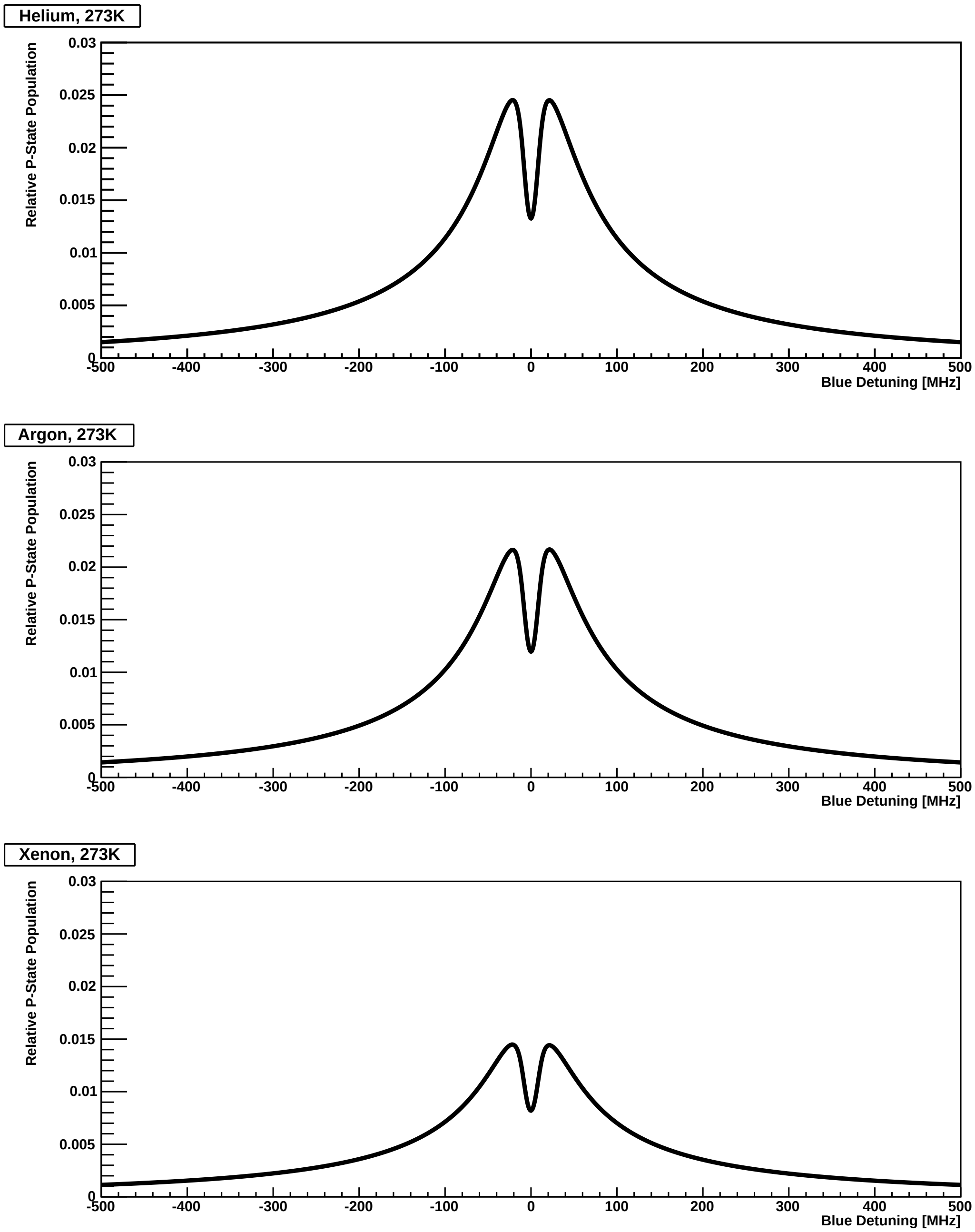

Figure 4.6: The combined lineshape for a simulated single Ba$^+$ ion trapped in 273-K Helium, Argon, and Xenon. The widened non-Gaussian velocity distribution of an ion trapped in Xenon reduces its fluorescence.

Chapter 5

Ion trapping and detection systems

5.1 Linear traps for EXO

5.1.1 The first-generation linear trap

The first-generation linear trap for EXO Ba-tagging research and development has been described in detail in [10] & [56]. An axial length of 66 cm was chosen for this linear RFQ based on ion cooling simulations, and a trap radius of 2.66 mm was selected a compromise between large trapping volume/good optical access and keeping RF drive voltages, which scale with the square of the trap radius, manageable. 6 mm diameter rods with 2 mm spacing (as shown in Figure 5.1) produce a maximally ideal hyperbolic potential with $r_0 = 2.66$ mm. One of the major considerations driving the trap's design was the minimal use of insulating material in view of the trapping region. Surface charge build-up on insulators can produce large static potentials in vacuum, and to shield against these potentials the trap electrodes and insulating spacers are stacked on a supporting rod, as seen in the inset of Figure 5.1. This stacked structure ensures complete shielding of the material insulating adjacent electrodes by nesting it inside of the electrodes themselves. This design, however, suffers from an inherent lack of rigidity, which necessitated the use of an insulating support structure in the middle of the trap in addition to insulating mounting structures at either end. Additionally, the stacking of electrodes and insulators along trap rods compounds

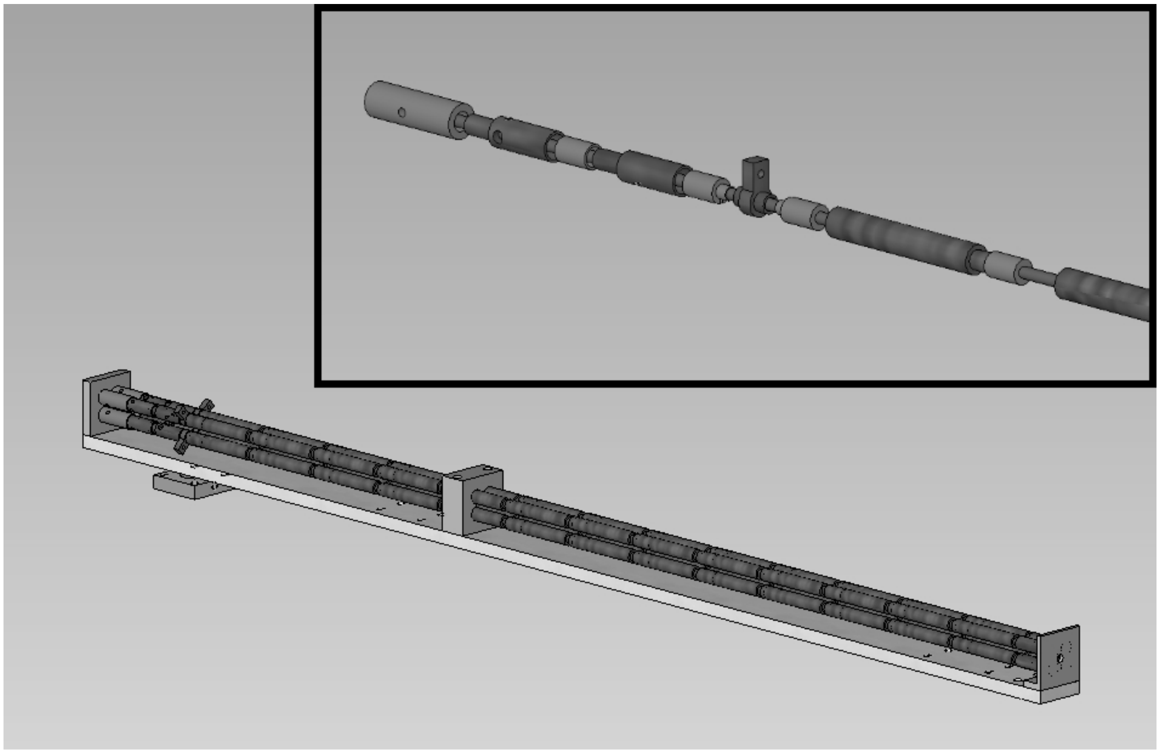

Figure 5.1: The first-generation linear trap, designed to minimize exposed insulators. Inset: The nested electrode and insulator structure in exploded view.

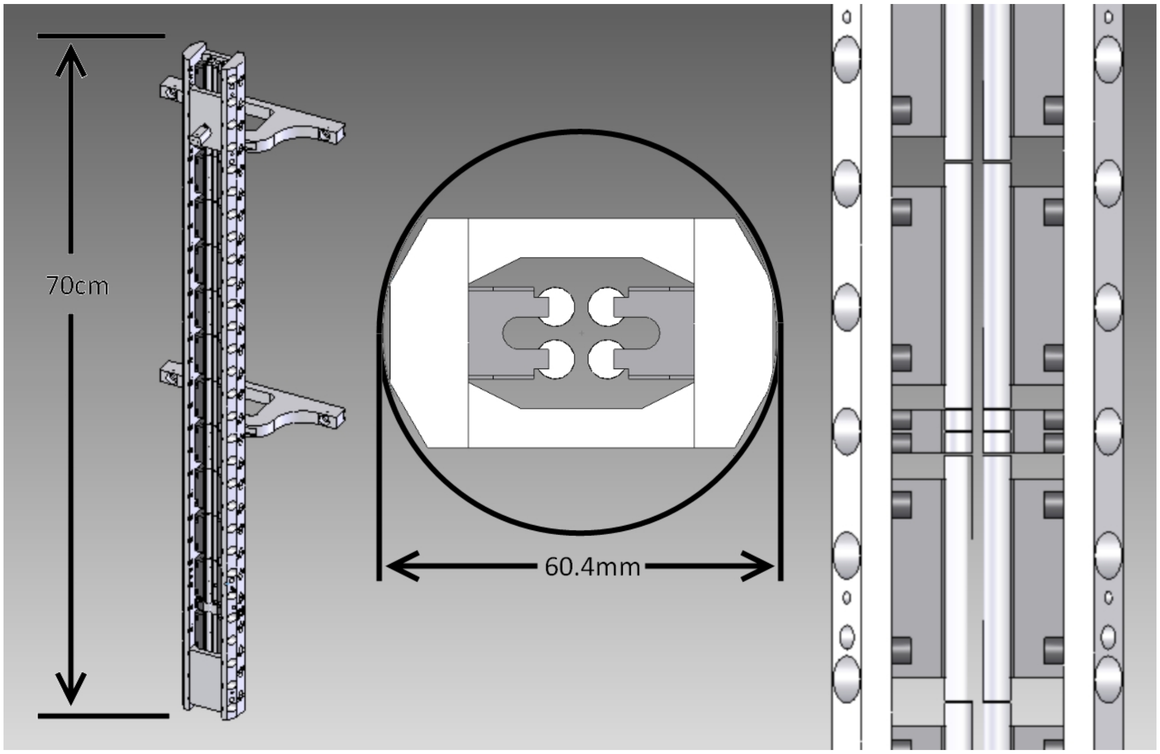

Figure 5.2: The second-generation linear trap. Left: Assembled ion trap, diametric view. Center: overhead view. Right: close up frontal view of the detection region. Detection region segments are smaller for tighter spatial confinement.

electrode position errors due to fabrication tolerancing. This trap successfully stores ions, has yielded valuable lifetime information, and can detect single ions stored in a buffer gas as described in [10], but fails when attempts are made to move cooled ions along the trap length, as will be discussed in §6.2. This is attributed to perturbations in the trapping potentials due to the misalignment of trap electrodes arising from the limited accuracy of the mechanical assembly.

5.1.2 The second-generation linear trap

Difficulties in the spatial manipulation of ions in the first-generation linear trap necessitated a re-design, with particular attention paid to rigidity and mechanical tolerances; the re-designed trap is shown in Figure 5.2. While the electrode diameter and rod spacing were taken directly from the first-generation trap, the overall length of the trap was extended to 70 cm by increasing the length of the cooling segments to 5 cm. The gaps between adjacent segments have been reduced to an “as small as is reasonable” 0.5 mm, to minimize RF potential perturbations at segment boundaries. The nested electrode structure of the first-generation trap has given way to a precision-assembled rigid structure, while attention has still been paid to the minimization of exposure to insulators. Additionally, this trap needed to be inserted, fully-assembled, into the pre-existing vacuum chamber through a 4.5-inch conflat flange with the standard inner diameter of 2.5 inches.

The trap is constructed wholly of UHV compatible materials, which have been cleaned in ultrasonic baths of detergent, acetone, and isoproponol. Stainless steel electrodes are positioned on insulating macor pieces through the use of dowel pins, and are held in place by vented silver-plated stainless steel screws which also serve as an electrical connection between the trap electrodes and their leads. Silver plated screws are used wherever possible in the vacuum to avoid cold-welding of stainless screws to stainless parts. The macor insulators are designed in such a way as to provide a good position reference for the electrodes, and to maximize the distance from any insulating surface to the trap center. Each macor mount supports two trap electrodes, and is seated on a precision ground stainless steel bar. As with the electrodes, the macor block’s position is defined relative to the bar with a pair of pins, and silver-plated stainless steel screws hold each block in place. Each bar with its associated trap electrodes constitutes one half of the ion trap, and the two halves are connected via stainless supports, the positions of which are, in turn, fixed by pins between the supports and bars.

A conventional Barium ion source loads ions into the trap in segment 2. A ceramic crucible is mounted perpendicularly to the trap on a plate which both aligns it with the trap and serves as a 2 mm aperture for the neutral Barium vapor emitted by the crucible. Barium is loaded into the crucible from a length of Barium-Aluminum getter wire. When heated, Aluminum in the $BaAl_4$ alloy exothermally reacts with and bonds to Nickel in the powdered mixture, releasing the Barium in a vapor onto the crucible walls. As the Barium is quite reactive, this Barium loading must be done in vacuum, and the getter wire must be replaced every time the chamber is exposed to atmosphere. By subsequently running a reduced current through the wire, the interior of the crucible is heated, releasing a low flux of neutral Barium into the trap.

An electron gun mounted opposite the vapor source emits a beam of 500 eV electrons into the ion trap, ionizing Barium atoms in the trap interior. While the electrons are emitted at 500 eV, their energy at impact is the difference between the 500 V electron source and the instantaneous value of the RF voltage at the impact location, so electron energies can vary by as much as 200 eV. The gun thermionically emits electrons from a tungsten filament, and so glows brightly when in operation. While this often creates a background for fluorescence detection in ion traps, the large spacial separation between segment 2 (where the electron gun is located) and segment 14 (where fluorescence light is collected), and the presence of a mid-chamber bulkhead (see §5.2), limit the light from the electron gun collected in the fluorescence acquisition system. While it can be observed, it does not significantly add to the fluctuations on the background, so operation of the electron gun during ion spectroscopy measurements is possible without appreciable reduction of sensitivity.

5.2 Vacuum and gas injection systems

Operation of an ion trap in a low pressure gas of part-per-million level purity requires the use of UHV vacuum compatible materials and techniques to limit impurities emitted into the gas, and a pure gas supply to feed into the trap chamber. A 30-liter internal volume, custom-built, stainless steel vacuum chamber from Trinos vacuum houses the ion trap. 8-inch conflat ports are positioned along the length of the chamber to allow experimenter access, and numerous 4.5-inch and 2.75-inch ports are used for laser access and electrical feedthroughs. While the chamber is fitted with a number of viewports for convenience in performing mechanical tasks, all but the laser injection viewport are optically sealed with opaque neoprene to prevent room light from contributing to the ion fluorescence background. A bulkhead separates two vacuum spaces connected by a 4.5-inch conflat port inside the chamber. This was intended to serve as an orifice through which the chamber could be differentially pumped. Differential pumping along the trap length has yet to be deemed necessary,

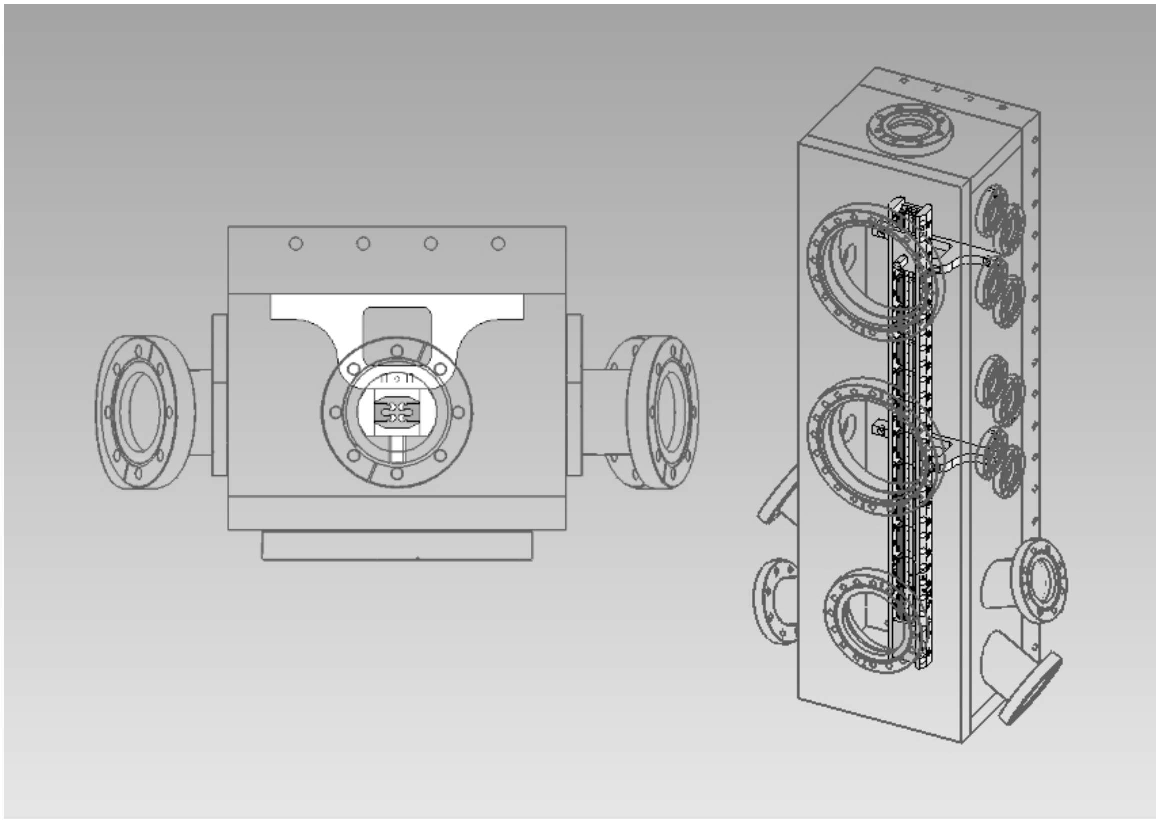

Figure 5.3: The second-generation trap in the custom stainless steel vacuum chamber.

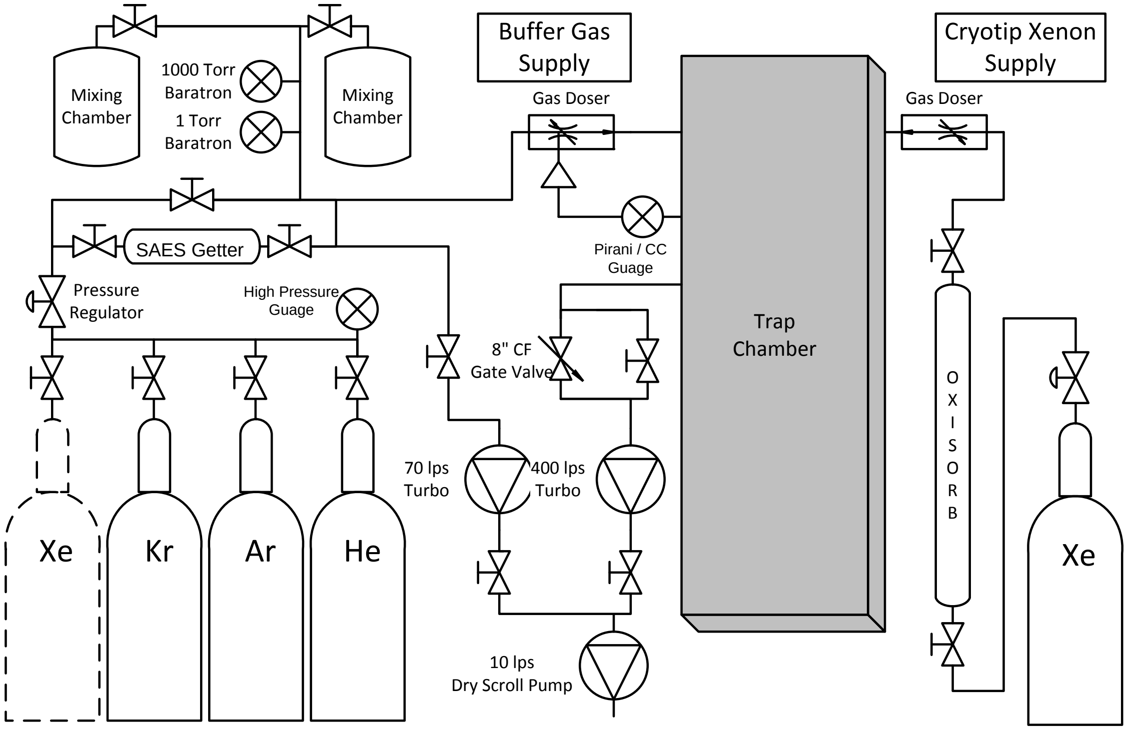

Figure 5.4: Gas supply and purification system

but the option to implement this remains. A 400-l/sec turbomolecular pump (TMP) backed by a 10-l/sec dry scroll roughing pump is used to pump the chamber to vacuum.

The gas injection system is shown in Figure 5.4. Gas bottles of different species can be simultaneously connected, so that a choice of gas or custom mixture of multiple gases can be prepared without swapping bottles. Gases are fed through a SAES Zirconium-getter gas purifier cartridge[1], and can be optionally stored in a set of chambers for mixing different species. A Pfeiffer Vacuum gas doser[2] dispenses gas to the vacuum chamber, where it is subsequently pumped out by the TMP. The equilibrium chamber gas pressure is maintained by the gas doser's control unit; pressure is sampled by a dual-range pirani/cold-cathode gauge[3], and the gas feed rate is adjusted

---

[1] SAES MonoTorr PF3C3R1

[2] Pfeiffer EVR116 with RVC300 controller

[3] Pfeiffer PKR251

accordingly to keep the pressure at a programmed setpoint.

Removable ovens encapsulate both the chamber and gas hardware, and are used to bake both systems to 135C for at least 48 hours if either have been exposed to atmosphere, to remove water from vacuum components. While this is a relatively low-temperature bakeout by UHV standards, the flushing of the system with gas improves vacuum quality substantially, and long ion storage times have been demonstrated with this procedure.

5.3 Linear trap electronics

The system of electronics for implementing the trap electrode potentials are shown in Figure 5.5. A radio-frequency (RF) function generator supplies a sinusoidal voltage signal to a 55 dB RF amplifier, the driver supplying all trap RF. This ground-referenced signal is split into opposite phases and voltage multiplied by a ferrite core transformer with a 3:30 turns ratio, and the balanced 200 Vpp, 2.2 MHz signals output from either end of the secondary coil are distributed to the trap, one phase to x-rods, the other phase to y-rods. Using Equation 3.6 it is seen that this produces an RF trapping depth and q of:

$$\begin{aligned} \text{RF Depth} &= \frac{q^2V^2}{4m\Omega^2r_0^2} = 5.2\text{ eV} \\ q_{x,y} &= \frac{2qV}{m\Omega^2r_0^2} = 0.2. \end{aligned} \tag{5.1}$$

The trap electronics and cabling have a net capacitance of 250 pF (∼15 pF per segment), and are connected in parallel with a 45-1150 pF variable capacitor used to tune resonant behavior. The 55 dB amplifier is capable of absorbing 100% reflected RF power, however, so little consideration is given to impedance matching the system to the 50Ω amplifier output imdepence. As trap RF is an experimental parameter rarely changed in the course of operation, manual operation of the function generator is sufficient for most adjustments.

DC signals, used for creating the trapping minimum and for ion manipulation, are created using a National Instruments 16-bit DAC card in a PXI crate[4], connected to a data acquisition computer via PCI bus. With an RF trap depth of only 2 eV, ions with kinetic energies greatly exceeding this number are rapidly lost, and therefore DC potentials need not much exceed this range. The -10V to +10V signals generated by the DAC are sufficient for this purpose. As the electrodes draw no DC current, the high output impedance DAC can supply these signals directly, without need for output amplifier or buffer.

The AC signals are combined with the DC voltages through a set of parallel RC filters, with 10 msec time constants to ensure unattenuated transmission of the RF signal to the trap electrodes while effectively isolating the DAC from the RF. These filters do, however, limit the rate at which trap DC levels can be changed, and if switching times faster than 1 msec are needed, a different scheme would be needed. This mixing is done immediately outside of the vacuum feedthroughs to minimize the total capacitive load of the system. Once the RF and DC signals have been summed, the signal is carried through via Kapton-insulated wires to the trap electrodes. Opposite electrodes are connected to each other directly in vacuum, and x-electrodes and y-electrodes of the same segment carry the same DC voltage, except in segment 14, the storage and observation segment. There, an optional battery-driven DC bias between x- and y-electrodes can be introduced, in order to generate a non-zero value of the a trapping parameter of Equations 3.12 and Figure 3.2. During most operations, however, this value is maintained at zero for maximal stability.

5.4 Trap acceptance simulations

The acceptance of this trap can be readily evaluated in SIMION8 using the gas collision simulation algorithm described in §3.2. The trap is operated with the following

---

[4] Model PXI6259

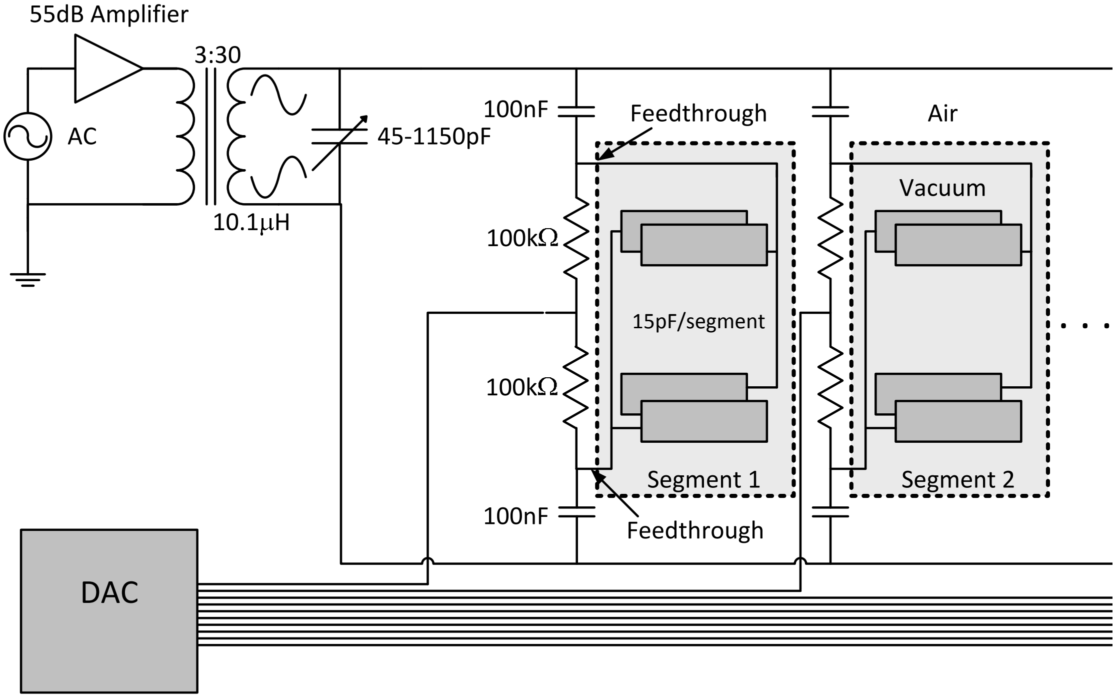

Figure 5.5: Trap electronics schematic: An amplified AC signal drives a resonant circuit composed of the secondary of a transformer, a variable capacitor, and the trap. The signal is coupled through capacitors to the segments, each of which are supplied with their own DC level from the DAC.

voltages and related parameters:

$$\begin{aligned} V_{RF} &= 200\text{ V} & q = 0.2 \\ \Omega_{RF} &= 2\pi \times 2.23\text{ MHz} & \text{Depth} = 5.2\text{ eV} \\ U_{DC} &= \{0, -0.25, -0.50, ... - 2.75, -3.0, -10, -3.0, +10\} & \end{aligned} \tag{5.2}$$

The trap acceptance is evaluated for several different ranges of initial ion kinetic energies in Figure 5.6, at a Helium buffer gas pressure of 1 mTorr. Ions are generated at the boundary of segment 1 with randomly assigned initial positions and propagation directions, and are allowed to propagate in the RF potential until they have either left the trap or survived for 6 msec, a length of time exceeding the thermalization time for the ions. Figure 5.6 shows the probability of an ion's thermalization and capture as a function of initial distance from the trap axis and the ion's initial velocity vector's angle with the trap axis. There is marked loss of acceptance with increased energy for all initial parameters, as the ion's initial kinetic energy must be completely dissipated in the first round-trip pass in order to remain captured.

5.5 Spectroscopic laser systems

5.5.1 Laser sources

The 650-nm and 493-nm spectroscopy beams are produced by a pair of tunable diode lasers from Toptica Photonics. Red laser light is generated by an anti-reflection coated 35-mW diode, mounted in a Littrow configuration in a DL-100 laser head. No laser diode yet exists at 493 nm, and so 493-nm light is generated by frequency doubling a 986-nm beam from a Littrow-mounted IR diode in a ring cavity containing a $KNbO_3$ doubling crystal. Frequency stabilization of the laser is achieved through nested feedback loops. The diffraction gratings which constitute ends of the diode laser cavities are fed back upon in such a way as to keep the the laser resonant with external adjustable Fabry-Perot cavities. These, in turn, are slaved to an opto-galvanic cell, which provides an absolute frequency reference for each laser.

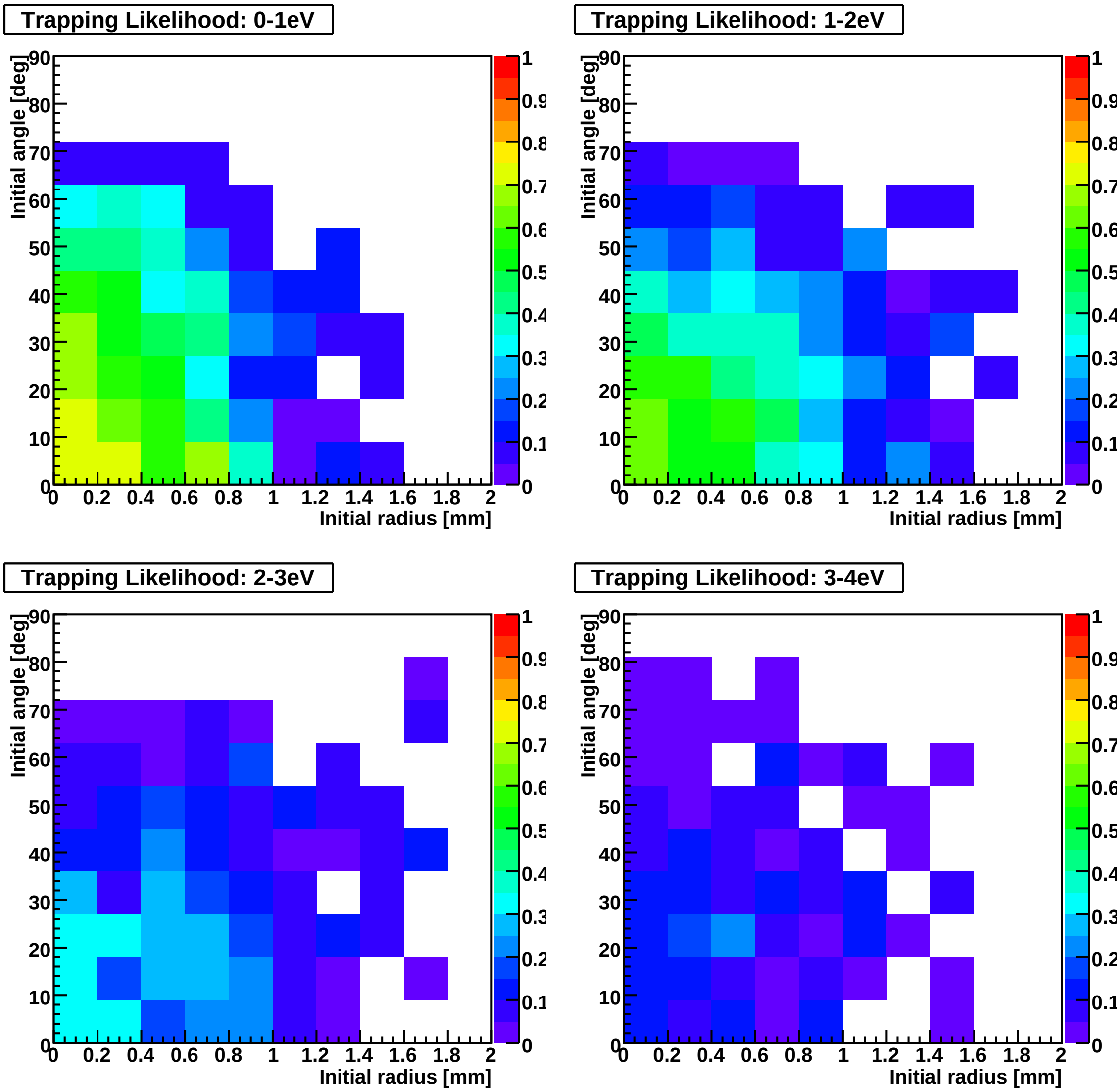

Figure 5.6: Ion survival probability as a function of initial radius and launch angle. Trap acceptance drops significantly with initial ion kinetic energy, angles greater than 45°, and at radii past 1 mm.

The opto-galvanic lock, inspired by the work of Koerber [57], works by exciting a Barium cold-cathode plasma discharge lamp[5] with resonant lasers. The excitation of the Barium ions present in the discharge reduces by a small amount the ionization potential of the ions in the plasma, causing a small enhancement of the discharge current. The effect is small, even when measured across a large resistor, and necessitates the use of lock-in detection. An optical chopper wheel amplitude modulates each beam, at different frequencies, and the lamp signal is read out by a pair of lock-in amplifiers, each looking at the reference signal of a different laser. As a result, each lock-in outputs a frequency dependent resonant signal for its respective laser, from only a single lamp. Each opto-galvanic signal is a gaussian in frequency, corresponding to the doppler width of the ions in the plasma. The lack of a zero crossing requires locking to the side of the gaussian, and as the amplitude of the signal is dependent upon the laser power, each laser must be power-stabilized to prevent frequency drift resulting from a change in signal amplitude.

Locking to the side of the peak implies that the laser entering the lamp must be detuned from resonance. The AOMs move power from an undiffracted mode into a diffracted mode with a -200 MHz frequency shift. For excitation of trapped ions, the 1st order diffracted beam is used. For the opto-galvanic cell, the undiffracted beam from a separate AOM is used. As a result, the frequency of the beams sent to the lamp are 200 MHz above those which is sent to the trap, and when the trap beams are on resonance, the lamp beams are on the side of the peak, and can be locked there. Seeing signals from the lock-in detection are enough to ensure that the lasers are close enough to resonance to detect clouds of ions trapped in gas. The final setpoint for the lock is determined at the start of a run, by maximizing fluorescence of trapped ions, and locking each laser to the values of their lock-in signals at that point.

Once frequency-stabilized, each beam is coupled to the same single-mode optical fiber[6], for transport to the ion-trap. This serves multiple purposes: First, it isolates table vibration from the trap injection optics, and avoids room-traversing beams. Second, the single-mode fiber serves as a mode cleaner for each beam, outputting

---

[5] Perkin-Elmer Lumina N305-0109

[6] Nufern S-460HP

only the $\mathrm{TEM}_{0,0}$ fiber mode. This ensures a Gaussian intensity profile, which can be easily manipulated and focused, and is fixed in all ways but intensity. Finally, that the same fiber carries both spectroscopy lasers constrains them to be co-axial at the output, allowing both lasers to be steered simultaneously without possibility of laser-laser misalignment.

Lasers output from the fiber are focused by a molded asphere and directed into the vacuum chamber along the trap's longitudinal axis. Adjustment of the beam focus is performed by adjusting the relative fiber/asphere distance. As the trap is mounted so that the longitudinal axis is coaxial with the viewport at the bottom of the chamber, a beam which is centered on that viewport and normally incident will be close to optimally aligned. As the beam is converging as it passes through the viewport, light reflected off the back viewport surface and then off the front surface will be passed into the trap, and focused at a different location, causing difficulty in beam focusing, and an increase in scattered light. To mitigate this effect the viewport is anti-reflection coated for 493-nm light on both surfaces. It is unnecessary to do the same for red light, as red fluorescence is not measured, for reasons explained in §5.6. The cleanliness of viewport surface is crucial in minimizing light scattered out of the beam.

Laser powers are stabilized through the use of a bank of acousto-optic modulators (AOMs). As scattered laser light is the dominant background for ion detection, fluctuations in the laser powers lead to a reduction of the ion detection signal-to-noise ratio. Additionally, fluorescence rates can vary if laser powers are allowed to drift. Laser power fluctuations are generally the result of temperature fluctuations influencing beam alignments, most notably affecting laser coupling into fibers. As indicated previously, the beam powers at the opto-galvanic cell must be stabilized as well. Photo-diodes sample laser powers at the trap injection optics and at the opto-galvanic cell, the signals are read out by PC through PXI data acquisition cards, and PID software feeds back on AOM RF signal amplitudes via a DAC card supplying signals to control inputs of voltage-controlled attenuators. In this way the powers can be stabilized for extended periods of time to setpoints that can be arbitrarily modified by the PC, either by the operator or by a Labview program crafted for a

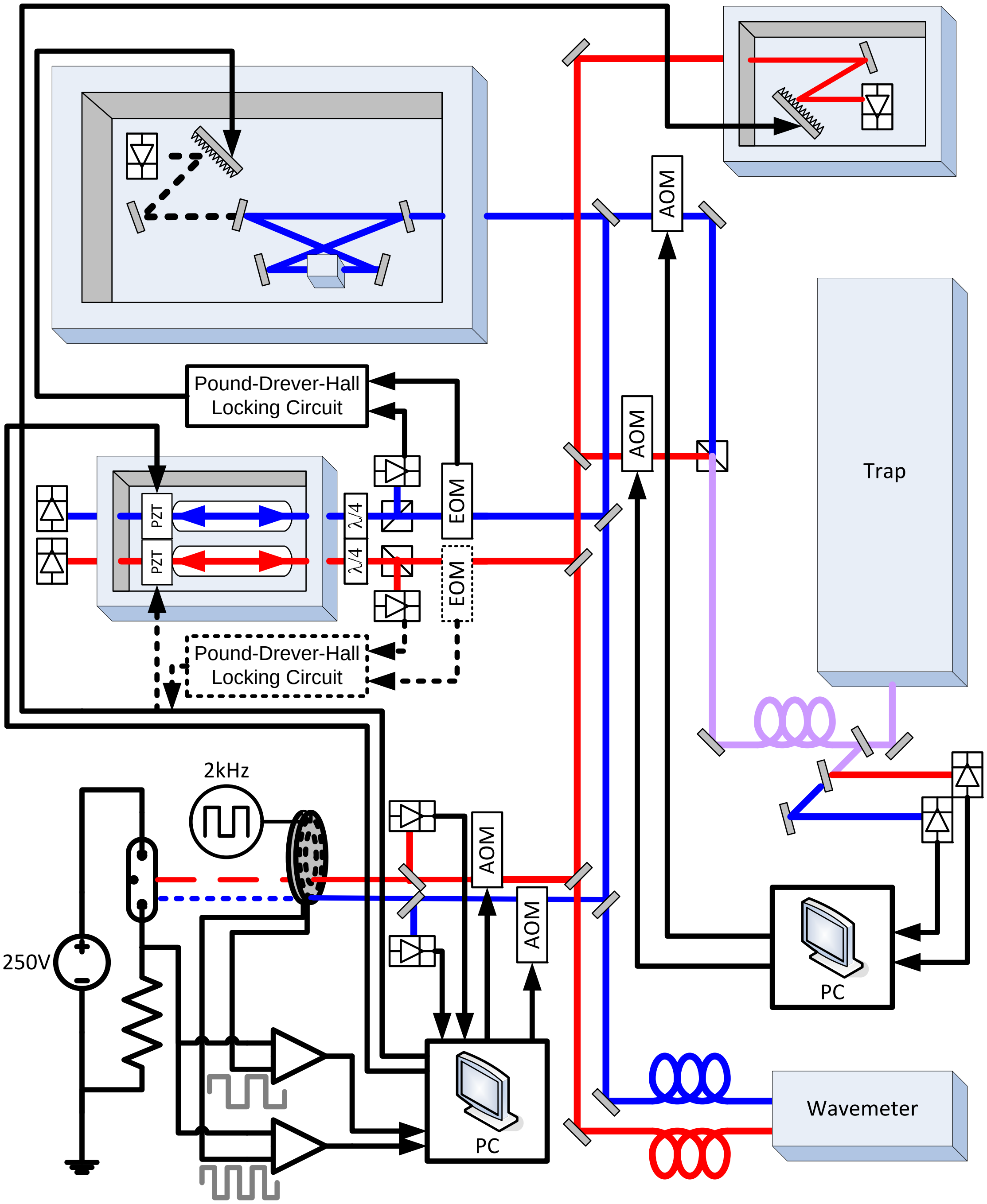

Figure 5.7: A schematic of the laser systems. Each laser is locked to a Barium plasma discharge cell for long-term stability.

particular experimental scheme.

5.6 Fluorescence acquisition

Fluorescence light emitted by trapped ions is imaged by a long working distance microscope onto a CCD for detection. A custom-fabricated re-entrant viewport allows detection optics to be positioned as closely as a few centimeters. The microscope is an Infinity Photo-Optical Company InFocus Model KC, fitted with an IF-4 objective. The IF-4 is a 25 mm diameter objective with a minimum working distance of 64 mm, capable of collecting 0.95% of fluorescence emitted from a point source.

A reflecting filter mounted inside the microscope blocks over 99.9% of red light. As both the red and blue beams propagate together through the same set of focusing optics, the difference in wavelengths forces the two beams to be focused at different locations. As a result, a focus adjustment that minimizes blue scatter will cause significant red scatter. As the spontaneous emission rate of the blue transition is three times that of the red, there is much more signal available in blue photons; better detection sensitivity can be obtained by minimizing blue scatter while removing the high red background and its associated signal.

A spherical mirror has been integrated into the trap construction, directly opposite the detection microscope, on the other side of the trap. It is mounted so that the mirror's center of curvature is exactly at trap center, so that light emitted from trap center will be reflected directly back on itself, and through the point from which it was emitted. This light will focus in the microscope identically to fluorescence light emitted into the microscope directly, and leads to a factor of $\sim$2 signal enhancement without spatially blurring the ion cloud image.

Collected fluorescence light is counted with an Electron-Multiplied CCD (EM-CCD) camera. The IXon$^+$ DUO897 from Andor Technology is built around an E2V L3Vision back-illuminated, 550 nm AR-coated sensor, with at least 90% quantum efficiency from 490 to 650nm. The CCD array is 512×512 pixels, but to maximize ion detection signal to noise, it is read out with 8×8 binning. This balances the reduction of noise that accompanies readout (reduced with more binning) with increased background arising from a less precisely defined region of interest. The electron-multiplication readout register uses large ($\sim$ 50 V) clock voltages to obtain small charge amplification at each stage as charge is moved from the CCD readout register to the digitizer. While the per-stage gain is small ($\sim$ 1.01), there are several hundred stages, allowing for overall gain factors of 1000 or more. As a result, small signals can be amplified above the read noise, allowing for single-photon sensitivity. Unfortunately, the probabilistic nature of the stochastic multiplication process adds its own noise, not unlike that seen in avalanching devices. A full discussion of function and noise of EMCCDs can be found in [58].

The microscope/camera assembly can be accurately positioned using a three-axis micrometer-driven stage. Microscope alignment is a relatively easy process, as the field of view imaged on the CCD sensor is $\sim$ 4 mm × 4 mm, allowing the entire gap between electrodes, and the electrodes' inner edges, to be imaged. Alignment in the directions perpendicular to the microscope view is trivial. Placing the microscope focus at the proper depth is done by setting the microscope variable focus to the shortest working distance (to maximize collection solid angle) and adjusting the depth until the inner edges of the closest two electrodes are well resolved. Knowledge of the trap geometry places the trap center exactly 4mm further, allowing the microscope position to be easily set by adjusting the micrometer stage.

The overall collection efficiency is obtained by combining the quantum efficiency of the camera with the efficiency of collection optics:

$$\text{Collection Efficiency} = 1.7\%, \tag{5.3}$$

ignoring reflections from the viewport and optical surfaces internal to the microscope and camera. As the spontaneous emission rate of a trapped ion along the blue transition is $\Gamma_B \rho_{pp}$, taking the peak excited state population of a room-temperature ion from Figure 4.6 leads to an expected photon counting rate of:

$$\begin{aligned}\text{Single Ion Count Rate} &= \Gamma_B \times \rho_{pp} \times \text{Collection Efficiency} \\ &= 95.3 \times 10^6 \times 0.0062 \times 1.7\% \\ &= 10000\ \gamma/\text{sec} \qquad (5.4)\end{aligned}$$

5.7 Single ion spectroscopy

Single buffer gas cooled ions have been detected with high sensitivity in both ion traps, in observation times significantly shorter than the ion storage lifetimes. The ions in thermal equilibrium with a buffer gas have significantly reduced maximum excited state populations, making single ion detection in the gases more experimentally challenging than in vacuum. The signal-to-noise ratio for an ion signal $\langle S_{ion} \rangle$ collected in a given integration time measured on top of a background signal in that same period $\langle S_{bknd} \rangle$ is:

$$S/N = \frac{\langle S_{ion} + S_{bknd} \rangle - \langle S_{bknd} \rangle}{\sigma_{bknd}}, \qquad (5.5)$$

where σ_{bknd} is the standard deviation on the measurement of the background counts.

Adjusting the system to maximize detection sensitivity is best accomplished using trapped ions. The laser beam position and focus that optimize signal are not those that minimize background from scatter. To properly tune the alignments of the optical components, ions are trapped, the laser frequencies are tuned to resonance, and the ions' fluorescence is alternately turned off and on by blocking and unblocking the red spectroscopy laser. In this way, adjustments can be made that maximize the signal-to-noise. This is often an iterative process in the various alignments.

To obtain a single ion for evaluating sensitivity, the oven and electron gun are operated briefly, with the intention of loading a small number of ions. Trapped ions have a finite lifetime, due to collisions with the buffer gas and impurities therein, and over time the ion number will drop to zero. If the experiment is sensitive to the detection of a single ion, the fluorescence signal will become discretely quantized as

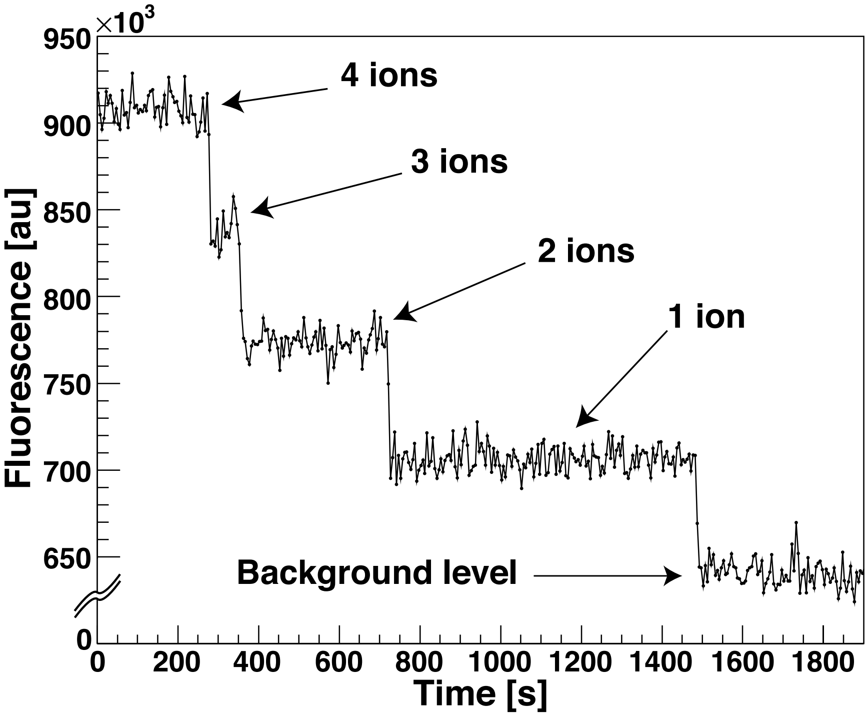

Figure 5.8: Ion fluorescence signal in the first-generation linear trap. As ions leave the trap, the signal drops in clearly quantized steps until the trap is empty.

the number of trapped ions becomes small. Figure 5.8 shows the fluorescence rate over time as ions loaded in the first-generation trap subsequently leave it, until empty. Each point in this series represents a 5-sec integration time, and each discrete step in the fluorescence corresponds to a single ion vacating the trap. By histogramming the fluorescence values in this time series, and fitting the background and one ion states to Gaussians, as is shown in Figure 5.7, a direct measurement of the system's sensitivity to single ions can be derived. Here the single ion signal = 5×10^4 CCD counts in 5 seconds of observation, yielding a signal-to-noise ratio of 10.6 for the detection of a single ion [10]. In practice, cosmic rays depositing charge in the CCD can produce a single exposure that resembles that of a single ion, so detection of a single ion entering an empty trap requires ~ 20 seconds of exposure; this guarantees at least 2 back-to-back samples during which the ion is present for the full duration

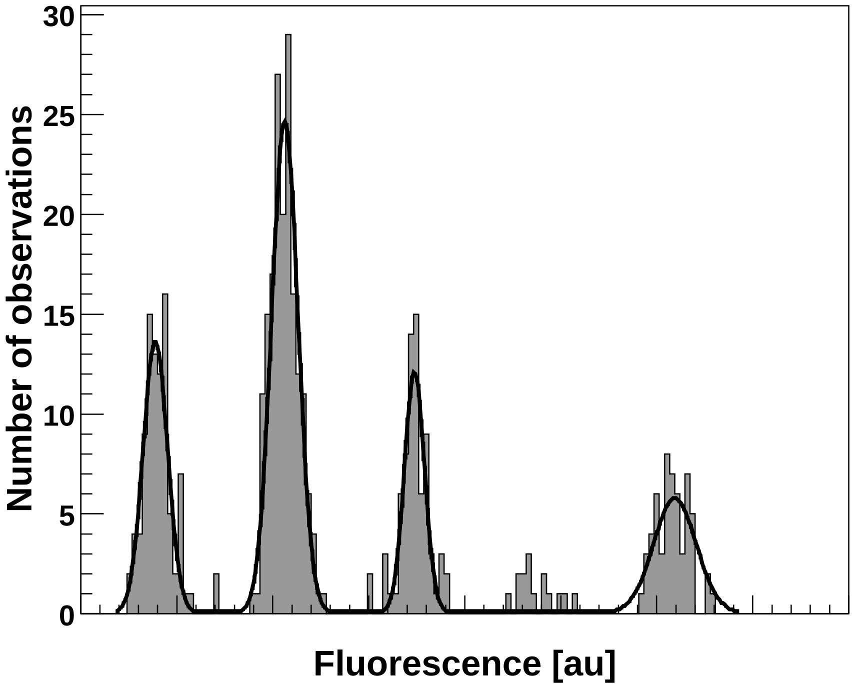

Figure 5.9: Histogram of fluorescence rates in figure 5.8. A signal-to-noise ratio of 10.6 was measured for single ion detection [10].

of the camera exposure.

5.8 Lifetimes of trapped ions

As detection of single ions requires several seconds of interrogation, it must be demonstrated that the average lifetime for a trapped ion is long compared to this time scale, and knowledge of this lifetime is essential to understanding the efficiency of ion detection. This is a quantity that cannot be practically estimated by simulation, as the simulation of one second of ion time in SIMION8 requires several hours of computing time, and the exact nature of impurities in the buffer gas is not known to the required accuracy. While one may be tempted to trap a cloud of ions and measure its decay rate, it is readily observed that the lifetime of an ion in a cloud is significantly shorter than that of a single ion in isolation; this is presumably due to Coulombic repulsion forcing a fraction of the trapped ions to large-radius orbits where they are more easily unloaded. To measure the expected lifetime of a single ion in a specific gas environment, ions are loaded and allowed to decay to zero ion number as described in §5.7, and the length of time during which the trap is populated with only a single ion is recorded. These values are then fit to an exponential distribution using a maximum likelihood method described in [6], and the decay time constant of this distribution is taken as the single ion lifetime. Average ion lifetimes in excess of 5 minutes have been observed in a range of Helium pressures in the first-generation trap, and similar values have been observed in the second generation ion trap. Plotted in Figure 5.8 is the single ion unloading rate (lifetime^{-1}) as measured in the first-generation trap as a function of varying pressures of He and Ar buffer gases. The data are fit to a model wherein the unloading rate is proportional to the gas pressure, to account for impurities inherent to the buffer gas, plus a constant, allowing for a constant source of impurities from the vacuum chamber, or a separate unloading mechanism which is unrelated to the gas pressure. Lifetimes are consistently lower for ions confined in Argon, though still sufficient for detection.

As discussed in §3.3.2, collisions with heavy Xenon atoms are destabilizing for confined Barium ions. Experimentally, the RF heating due to Xenon collisions makes

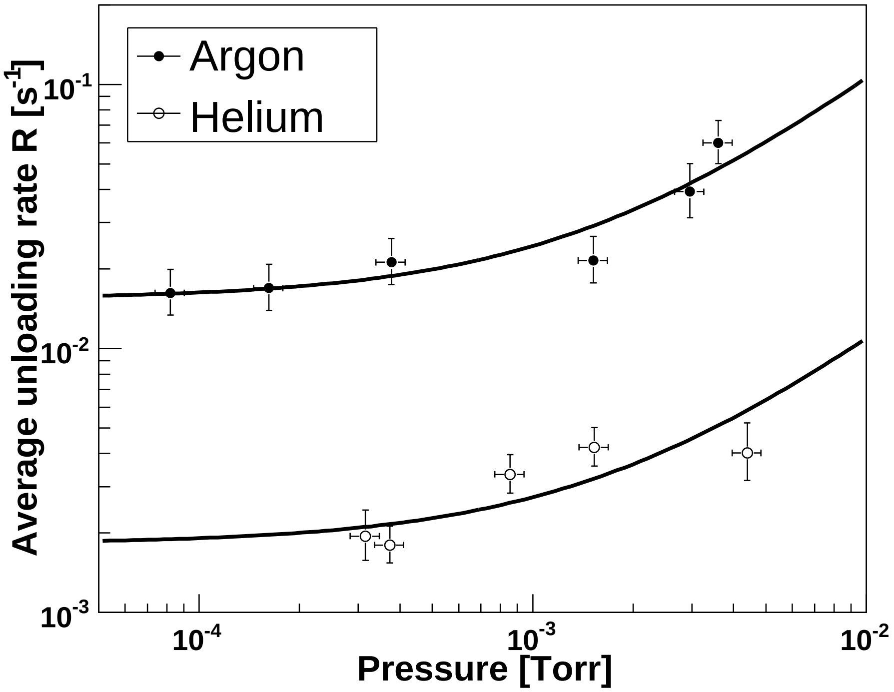

Figure 5.10: The average unloading rate (lifetime^{-}1) of single ions stored in varying pressures of Helium and Argon buffer gas. Unloading rates are fit constant plus a term proportional to gas pressure [10].

trapping in a pure Xenon environment impossible at the pressures accessible by this apparatus. In a mixed-species Helium/Xenon buffer gas, however, the cooling provided by collisions with the lighter Helium draws the trapped ion in from high-radius orbits caused by collisions with Xenon. The maximum Xenon/Helium pressure ratio for which stable confinement is still possible on lifetimes sufficient for detection is an important parameter, as some amount of Xenon contamination will follow any Barium-carrying probe that is extracted from a double beta decay detector and is brought to an ion trap.

A mixed-species buffer gas is prepared by filling one of the mixing chambers shown in the schematic in Figure 5.4 with ~ 500 Torr of Helium, and sealing that chamber, before evacuating the gas system and repeating the process, filling the other chamber with a lower pressure of Xenon. Evacuating the gas system and opening both chambers prepares approximately 5 standard liters of mixed gas, enough to supply the trapping chamber with 5×10^{-4} Torr gas for several hours. While the chamber is fitted with capacitance gauges capable of accurately determining the nature of the mixture prepared in the gas system, differences in flow impedances for the two species through the leak valve causes the Xenon pressure fraction in the trapping chamber to be significantly different. A residual gas analyzer (RGA) is used in the trapping chamber to determine the relative Xenon/Helium pressures by comparing their peak intensities. The use of an RGA sets an upper limit of 5×10^{-4} Torr on the operating pressure in the chamber. Figure 5.8 shows the average unloading rate (lifetime^{-1}) of a single ion as measured in buffer gases spanning a range of Xenon/Helium pressure ratios. A total pressure of 3.6×10^{-4} Torr is maintained throughout. The unloading rate fits well to a power law in the Xenon/Helium pressure ratio, plus a constant unloading rate due to impurities unrelated to the Xenon pressure.

$$R = C_0 + C_1 \left(\frac{P_{Xe}}{P_{He}} \right)^n \tag{5.6}$$

The fit parameters are listed in Table 5.1. This model is motivated by the physical intuition that if an ion is unloaded, on average, after n Ba$^+$/Xe collisions within a characteristic cooling time, then the ion unloading rate should be proportional to

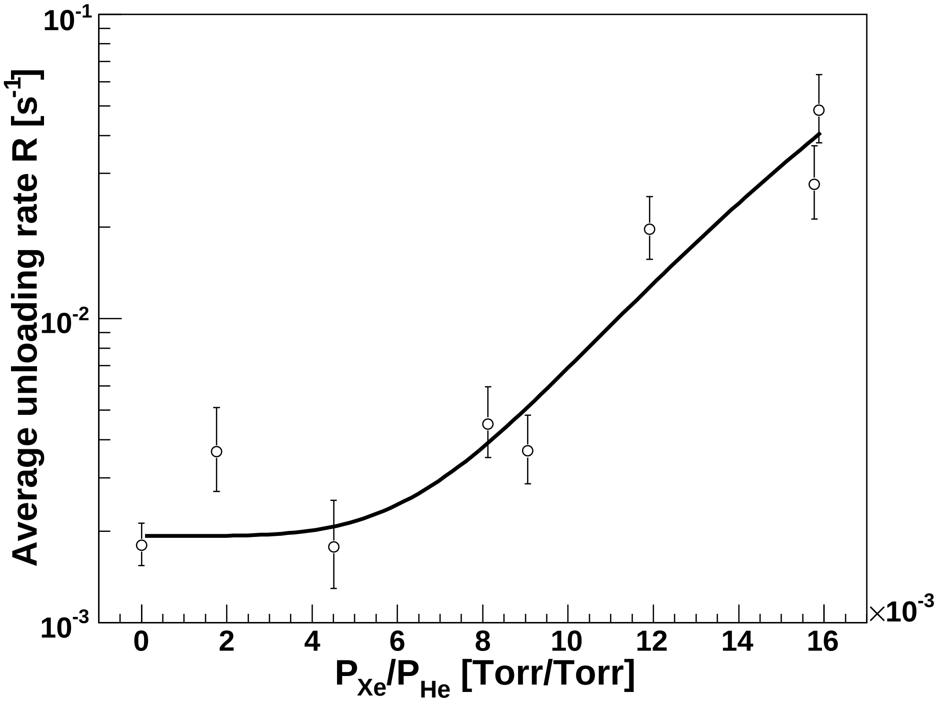

Figure 5.11: Measured average lifetimes of single ions stored in 3.6×10^{-4} gases of varying He/Xe composition [10].

Parameter	Value
n	4.5 ± 0.6
C_0	$(1.8 \pm 0.3) \times 10^{-3}$
C_1	30 ± 4
χ^2/dof	8.6/5

Table 5.1: Fit results and χ^2/dof of power-law collisional unloading model to He/Xe data [6].

the Xe pressure to the nth power. The fit value of $n = 4.5 \pm 0.6$ suggests that 4-5 successive Ba^+/Xe collisions are required to eject the Ba^+ ion from the trap.

From this plot it can also be seen that at 3.6×10^{-4} Torr a Xenon content of up to 1% can be tolerated in the ion trapping chamber while maintaining ion storage times sufficient for high detection efficiencies. This corresponds to a total load of 1 μgram of gaseous Xenon in the 30-liter trapping chamber at any given time. The 400-l/sec pumping speed of the turbomolecular pump will therefore allow a maximum 13 μgram/sec Xenon mass flow rate into the chamber, whether that be through gas injection, or solid Xenon evaporation.

Chapter 6

Manipulation of Ba$^+$ ions

The ultimate goal of the EXO ion trapping program is to demonstrate the ability to move Barium ions from a Xenon time projection chamber to an ion trap for counting, with high measured efficiency. This work focuses on efforts to extract a Barium ion from a liquid TPC, though ion trapping techniques may be applied to extraction and detection of ions in a gaseous TPC as well. As a first step toward demonstrating the probe's ability to move ions through the full transfer process, we must show that it can successfully store ions and inject them into the ion trap. To do this, a stationary probe is mounted coaxial with the trap, with the intent of moving ions back and forth between the ion trap and probe. To understand each step of this process, a number of intermediate tests are performed.

6.1 Efficiency of intra-trap movement

Experimentally verifying the trap's efficiency for the slowing and capture of single ions is challenging. Ions must be studied one at a time, to eliminate the space-charge effects multiple ions introduce. The long-range ion-ion Coulombic interaction repels ions if they are injected into the trap simultaneously, yet can have a positive effect on capture efficiency as injected ions can be slowed by cooled ions already in confinement. Uncertainty with regards to the emission rate from the neutral Barium oven and spatial distribution of ionization location from the electron beam render the conventional loading mechanism unsuitable for direct measurement of the efficiency for conveyance of ions from one end of the trap to the other.

The trap, however is a reliable source of single ions. By loading a single ion into the trap and repeatedly adjusting the segments' DC potential levels, an ion can be repeatedly transfered to the probe end of the trap and allowed to return to the detection region. By measuring the lifetime for ions cycled in this way, and comparing it to the lifetime for ions stored in the detection region, the effect that this cycling has on ion lifetime can be determined, and the efficiency for the cycling can be evaluated.

The procedure is as follows:

1. The trap is configured with DC potentials as shown in figure 6.1a.

2. A small number of ions are loaded into the detection region in segment 14 (S_{14}) in 5×10^{-4} Torr Helium gas, and observed as ions leave the trap until only one ion remains.

3. Ions are observed in S_{14} for a time t_{low}.

4. The trap DC potentials are adjusted according to the sequence shown in Figure 6.1b,c, to produce a minimum at segment 3 (S_3), and transfer the ion to that segment.

5. The ion is stored in S_3 for a time t_{up}.

6. The trap DC potentials are adjusted according to the sequence shown in Figure 6.1d,a, to return the ion to S_{14}.

7. Steps 3–6 are repeated until the ion either fails to return from S_3, or is spontaneously lost from S_{14}, and the lifetime of the ion is recorded.

The values of t_{low} and t_{up} are varied in a sequence from one ion to the next, according the the parameters listed in table 6.1. Additionally, the lifetime of 10 ions stored in S_{14} were measured to obtain a storage lifetime against which the effects of shuttling ions between S_{14} and S_3 could be compared. By summing the results over the various

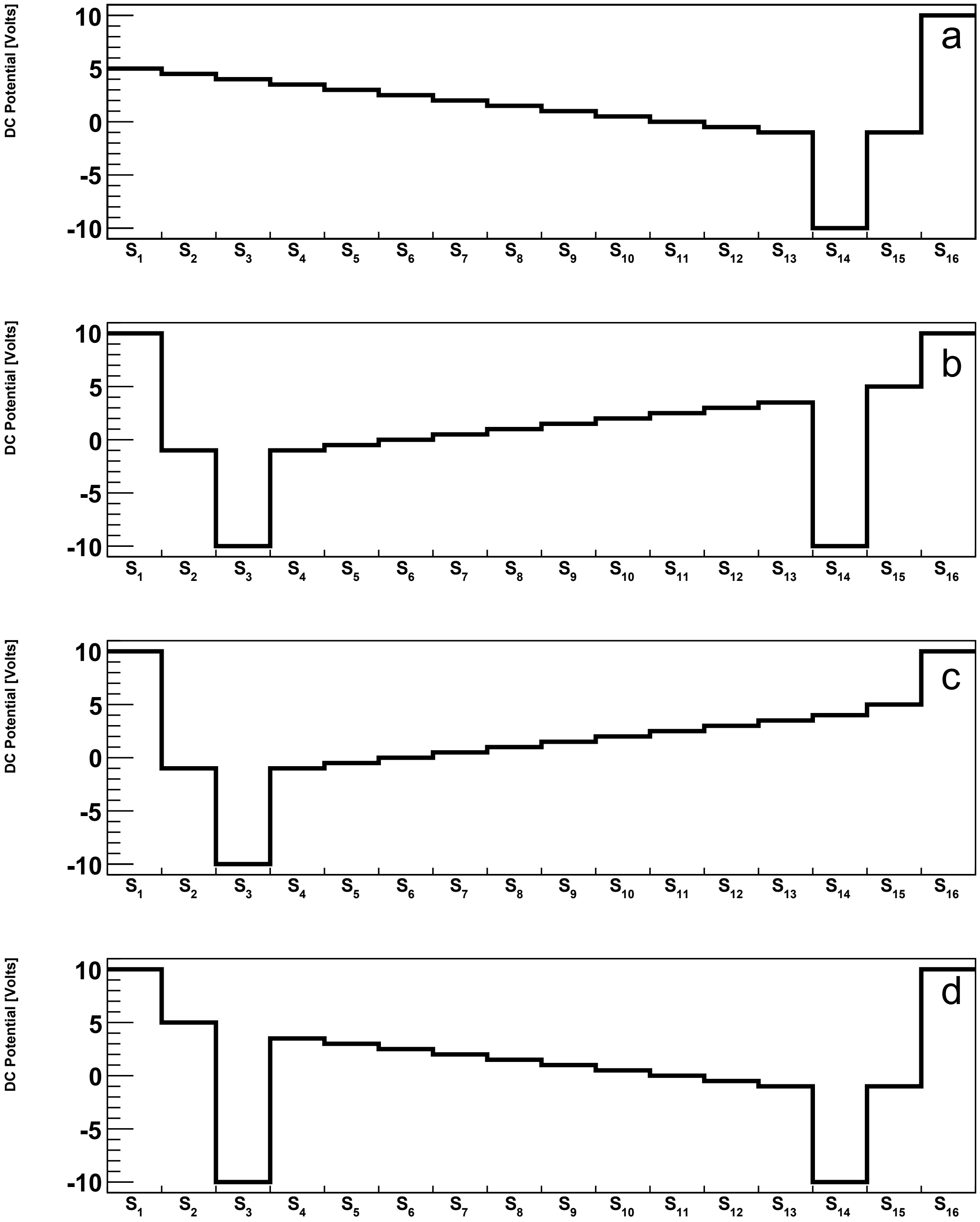

Figure 6.1: Ion shuttling potential adjustment scheme. Ions are initially loaded with DC potentials in configuration a, then potentials are cycled through b,c,d,a, moving ions from S_{14} (detection region) to S_3 (top of trap) and back.

Number of ions	t_{low}[sec]	t_{up}[sec]	Period [sec]	Attempted	Recovered
10	—	—	Stored in S_{14}	0	0
10	15	15	30	58	50
10	20	20	40	31	27
10	25	25	50	31	30
10	30	30	60	14	14
10	40	20	60	46	36
10	20	40	60	25	25

Table 6.1: Summary of attempted ion transfers. Ions are repeatedly stored in S_{14} for a time t_{low}, then transfered to S_3 for a time t_{up}, then returned, cycled with a period $t_{low} + t_{up}$. The total number of attempted and successful transfers is shown.

timing sequences, it's observed that of the 205 attempts to transfer an ion to S_3 and recover it 182 were successful, for a probability of successful transfer of:

$$P_{transfer} = 0.89 \pm 0.02, \tag{6.1}$$

which can be used as an initial estimate for the efficiency for the trap to probe transfer process. Additionally, by comparing the average lifetime of ions while in S_{14} to the lifetimes of ions while in S_3, the effect the of the shuttling of the ions on the ion survival can be determined. In order to calculate each lifetime, the total amount of time spent by ions in each segment is divided by the number ions lost while in that segment. If ions are lost from the trap while in the upper segment, they are assumed to have left the trap immediately after being transfered to S_3. The lifetimes are as follows:

$$\begin{aligned} T_{upper} &= 4400 \text{ sec } /23 \pm 4.8 \text{ ions } = 191^{+50}_{-33} \text{ sec/ion} \\ T_{lower} &= 8054 \text{ sec } /47 \pm 6.9 \text{ ions } = 171^{+29}_{-22} \text{ sec/ion} \end{aligned} \tag{6.2}$$

The errors quoted are statistical, by assuming the numbers of ions lost from each state are Poisson distributed. The data show no statistical difference in the lifetime of ions due to the shuttling, suggesting that the efficiency of the movement of the ions to the top of the trap is higher than the 89% measured; ion losses in these shuttling experiments were most likely due to the same process which unloads ions stored in the detection region.

6.2 Detection of ions ejected from trap

In order to use the ion trap as a source of ions for loading an ion probe, it must be demonstrated that ions stored in the trap can can be ejected through the probe end by adjusting the DC potentials. To do this, a channel electron multiplier (CEM) was mounted in the probe position, ions were loaded into the trap, and the DC potentials were adjusted to eject the ions.

Failure of this test led to the discovery of the first-generation ion trap's design flaws. Clouds of varying sizes were loaded in the first-generation trap's detection region, and adjustment of the potentials to eject the cloud caused the trapped ions to leave the detection region of S_{14}, but without registering counts in the CEM. By shifting the position of the microscope, it was seen that ions where only traveling as far as S_{13}, where they would reside indefinitely. This was attributed to small perturbations in the RF field caused by trap electrode shape and misalignment. The filter circuits that combine the RF and DC signals limit the rate at which the DC potentials can be changed at the trap. As the potential is raised in S_{14}, the ions move into S_{13} adiabatically, gaining no energy in the process. The room-temperature ions, possessing on average only 25 meV kinetic energy, were unable to overcome the RF barrier between S_{12} and S_{13}. It is for this reason the trap was redesigned; RF perturbations were reduced by tightening tolerances, and S_{13} was shortened to allow ions to be pushed through by raising the potential on S_{14}.

The second-generation trap was subjected to this ion ejection test immediately following its construction. Using single ions for this purpose prevents effects due to Coulombic repulsion inherent in clouds of ions. The spatial extent of a cloud increases with increasing ion number, altering the overlap of ions with the intensity profile of the laser, causing fluorescence rate to not be a linear function of ion number. Additionally, mutual repulsion of ions in the course of ejection may cause the trap to have a different emittance for clouds of ions than for singles.

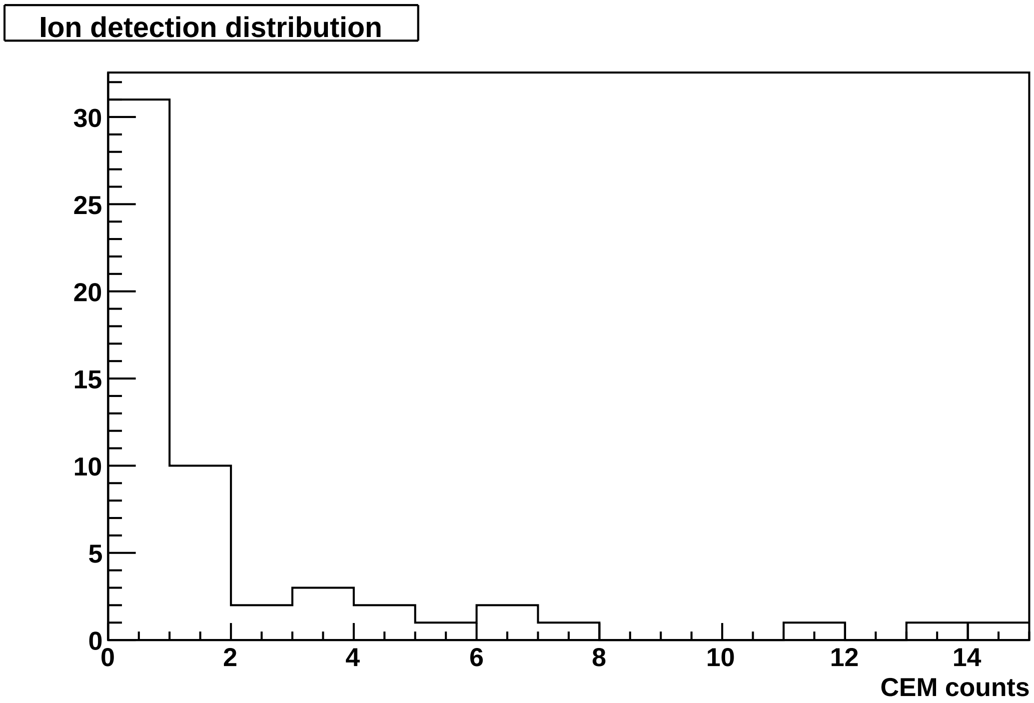

Figure 6.2: Distribution of CEM counts following the ejection of a single ion from the second-generation linear trap.

Single ions are loaded into S_{14}, in the presence of Helium, by loading a small cloud and observing as ions leave the trap until only one remains. The Helium pressure used for this is 1×10^{-5} Torr, to limit background CEM counts. The ions are then ejected from the trap by adjusting the the trap DC potentials to form a 0.5 V/segment ramp. Upon exiting the trap, ions are accelerated to the CEM by the CEM's 2 kV charge multiplication voltage. Following ejection, CEM pulses arriving within a pre-defined 10 msec time window are counted. The distribution of CEM counts for single-ion ejections is shown in Figure 6.2. From 55 ejections of single ions, counts were detected in the CEM 24 times. In the majority of these cases, however, multiple pulses were detected in the CEM. In the maximum case, 15 ions were detected, from a single ejected ion.

There are multiple potential sources for this multiplication. First, fluorescence detection as a measure of ion number is insensitive to the presence of "dark" ion species in the trap. Odd-isotope Barium ions exhibit hyperfine splittings in their spectra, and so do not fluoresce when driven by lasers tuned for the even isotopes. As Barium is nearly 18% abundant in odd isotopes, one would expect this to be the abundance of dark Barium ions in the trap; one in five ions should be trapped without being spectroscopically countable. Additionally, ionized Barium molecules or ionized buffer gas impurities could be easily trapped and stored without being counted. The inability of the CEM to differentiate between ion species causes these dark ions to be registered as counts. A second potential source for multiplication may be ionization of the buffer gas by ejected ions as they are accelerated in the CEM's 2 kV. It then becomes difficult to interpret these results in terms of transfer efficiency, except to say that in 21 of 55 trials, $38 \pm 8\%$, no ions were detected, so the efficiency of detection has an upper limit of 75% at 90% confidence. Previous work has measured detection efficiencies of Xenon ions in similar channel electron multipliers of only 30–40% [59].

6.3 The cryogenic ion probe

A prototype ion probe has been developed around the concept of an evaporable dielectric layer, with the aim of exploiting the charge state of the ion to capture it to a probe, while using an insulating layer to prevent neutralization by contact with a conductor. A cryogenic probe could potentially use solid Xenon, frozen from the detector itself, as the dielectric material. A Barium ion could be frozen into a layer of solid Xenon, for safe transport to an ion trap, where the Xenon could subsequently be evaporated, simultaneously releasing the ion for capture and detection.

While the Barium ion daughter of the double beta decay of ^{136}Xe is doubly charged immediately following the decay, it is not believed to retain its doubled charge permanently. Since the second ionization energy of Barium is greater than the band-gap energy of liquid Xenon, a doubly ionized Barium ion is thought to capture an electron from the liquid, reducing the charge state by one. The first ionization energy, however, is less than the liquid's band gap energy, leaving the ion singly charged with a long lifetime. This is as yet unconfirmed by experiment.

Also currently undetermined is the nature of the stability of the singly charged Barium ion state in solid Xenon. For the cryogenic probe to be a viable ion transport option, the singly charged state must have a lifetime that significantly exceeds the probe's transport time — at least a few tens of seconds in any probe movement scenario. While ionization energy arguments can again be made — Barium's first ionization energy of 5.2 eV is much less than the energy required to strip an electron from a Xenon atom, 12.1 eV — no experimental confirmation exists to show that a singly charged ion is stable in Xenon ice. In addition, crystal quality or temperature may play important roles in charge state lifetime. An experiment in which ions are loaded onto the cryogenic probe directly from the trap and then released back into the trap for counting was performed in order to address this question of ion lifetime in solid Xenon, and to demonstrate the viability of a cryogenic probe.

6.3.1 Cryogenic systems

As has been discussed in Chapter 3, the presence of Xenon in the buffer gas leads to the unloading of trapped ions. The design of a cryogenic probe requires cryogenic systems which limit the rate of Xenon evaporation in vacuum and also minimize Xenon released in the process of evaporation. This can be done through a combination of minimizing cryostat surface area onto which Xenon is frozen, minimizing the amount of Xenon frozen, and evaporating Xenon only from regions where required.

Maintaining a dielectric layer in an environment of low Xenon partial pressure requires a cryostat capable of reaching a temperature such that the sublimation rate is low. The rate of sublimation from a surface can be calculated by applying the Hertz-Knudson model [60], in which the flux of evaporating atoms from a surface of temperature T is given by:

$$\Phi = \alpha \frac{p_v - p}{\sqrt{2\pi m k T}}, \tag{6.3}$$

where p_v is the vapor pressure of the evaporating material, p is the ambient pressure, and α is the sticking coefficient which is typically between 0.1 and 1 [11]. The vapor pressure of Xenon as a function of surface temperature is plotted in Figure 6.3. The estimated sublimation rate in vacuum is calculated by setting $p = 0$ and choosing a sticking coefficient of 1; these values are given on the right-hand axis. Crystalline Xenon has a surface density of 2.6×10^{14} atoms/cm^2, so to keep sublimation rates

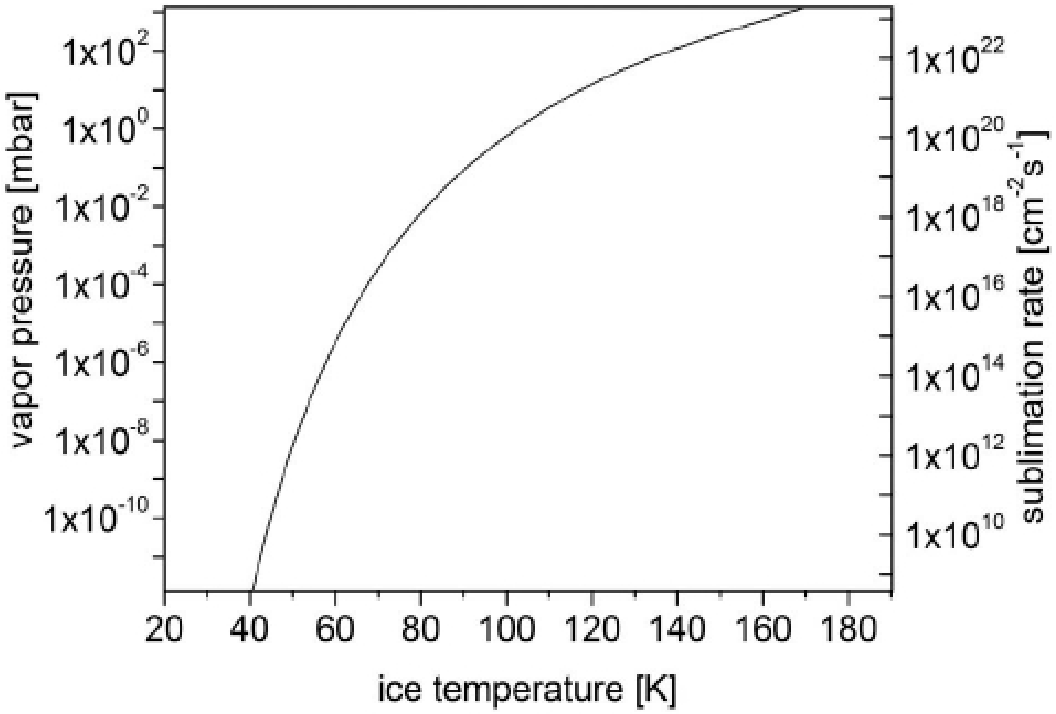

Figure 6.3: Xenon partial pressure and sublimation rate as a function of surface temperature. Temperatures below 50 K are required to suppress sublimation [11].

to much less than a monolayer during the span of an experiment, several minutes at least, the temperature of a cryogenic probe tip surface must be kept below 50 K. While multiple cryogenic technologies can access this temperature range, liquid Helium cooling is a convenient solution for testing purposes; it has a low startup cost, as there are no refrigerators to purchase, cooling power can be controlled by regulation of the Helium flow, and flexible lines can accommodate the movement of a mobile ion probe.

A cross-section of the ion probe is shown in Figure 6.4. Liquid Helium is fed from a pressurized dewar through a vacuum insulated transfer line to a copper heat exchanger. Gaseous Helium exhaust is controlled by solenoid and needle valves, the switching and adjustment of which regulate Helium flow and cooling power delivered to the heat exchanger. Super-insulating foil and a vacuum jacket surround the inlet and exhaust lines, with a threaded copper cold finger protruding. A stainless membrane serves as the thermal break between the cold finger and the warm jacket, ensuring that the only surfaces cold enough to freeze Xenon are the cold finger and copper probe tip fitted to it. The cryostat is capable of cooling a probe tip mounted in this way to as low at 20 K.

6.3.2 Capacitive ice thickness sensors

Minimizing the thickness of frozen Xenon layers while ensuring adequate ice coverage at the probe's biasing electrode requires a device capable of measuring the thickness of Xenon ice grown at that location. Toward this end high sensitivity micro-fabricated dielectric sensors have been developed which are capable of measuring Xenon ice layer thickness with nanometer-scale resolution while simultaneously serving as the electrode for ion capture and repulsion, in a 2-mm diameter package [11]. The construction of the sensors is shown in Figure 6.5.

Aluminum is deposited on a quartz substrate, and selectively etched away in a photo-lithographic process, leaving two electrically isolated aluminum electrodes with interleaved fingers. By producing a large strip density, hundreds of lines per millimeter, capacitances of tens of pico-farads can be generated in a 2-mm diameter

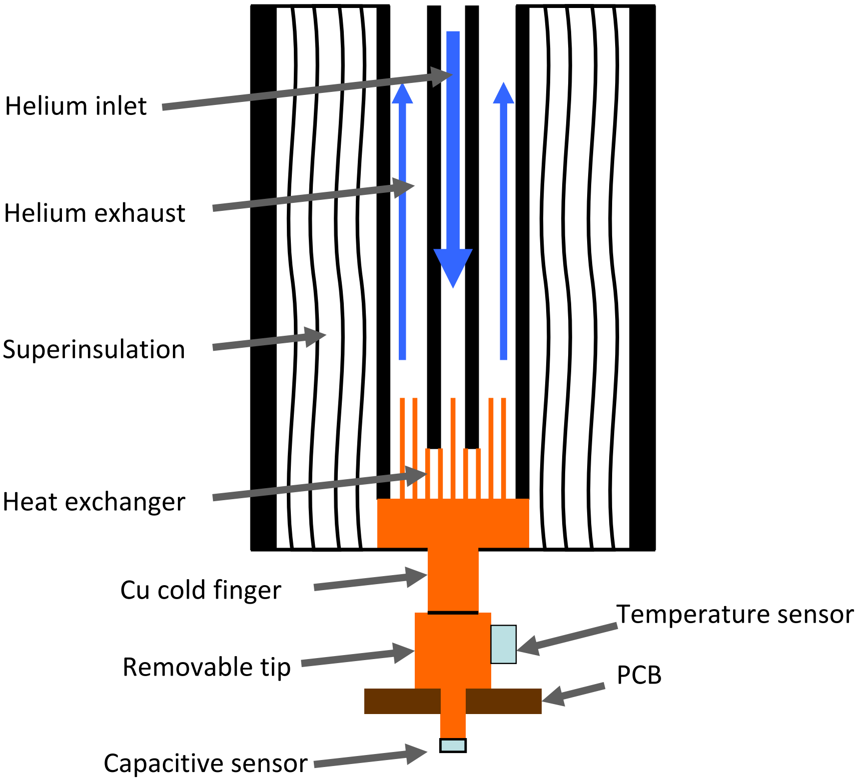

Figure 6.4: A cryogenic ion probe. Liquid Helium flow through a heat exchanger cools a copper cold finger, onto which is mounted a removable tip. A capacitive sensor serves as attractive bias for ion capture and Xenon ice thickness measurement device.

device. Measurements of the capacitance between electrodes using a capacitance bridge are linearly dependent on the average dielectric constant of the medium residing in active field region of the sensor, between the fingers and above the structure to a thickness on the order of half the finger spacing. Therefore, sensors saturate when a material thickness of ∼750 nm is frozen over them. When solid Xenon ($\epsilon_r = 2.25$) is the dielectric material, this is shown to produce a 5 pF increase in capacitance. Sensitivities have been estimated by modeling the slope of the linear regions of the capacitance vs. thickness curves. The sensitivity is dependent upon the geometry of the sensors, and for the 2-mm diameter sensors used, is on the order of 15 fF/nm of ice growth [11]. This corresponds to 0.1% of the sensor capacitance per nanometer. The Agilent LCR bridge[1] used to sample the sensors boasts a 0.2%[2] absolute accuracy, allowing Xenon thickness changes on the order of a few nanometers to be measured.

The sensors and fabrication techniques are described in detail in Fierlinger et al. [11], with the exception of some modifications implemented after publishing. Chief amongst these is the inclusion of a resistive heating element looping the sensor's active detection area, as shown in Figure 6.5. By running current through these heater loops, the Xenon ice (and any Barium ions contained within) can be preferentially evaporated from the sensor structure, while the rest of the cryostat is kept at freezing temperatures. This minimizes the amount of trap-spoiling gaseous Xenon released into the vacuum system. As seen in Figure 6.6, the single trace spirals around the sensor and then back out again. The heater's resistance is proportional to trace length (number of windings) and inversely proportional to the trace width, so a long, thin path will create a resistance that minimizes required drive current, but in practice small imperfections in the production of the sensors can produce discontinuities in narrow traces, reducing the production efficiency.

In addition to the evaporation of the frozen Xenon, the resistive loop serves another function: applying an offset voltage between the sensor's active area and the heater loop will allow the loop to act as a ring electrode. By positively biasing the ring with respect to the sensor, the ring can be used to guide ions to the center of the

---

[1] Model E4980A

[2] 40 mVpp, 1 MHz sampling signal, 220 msec sampling time

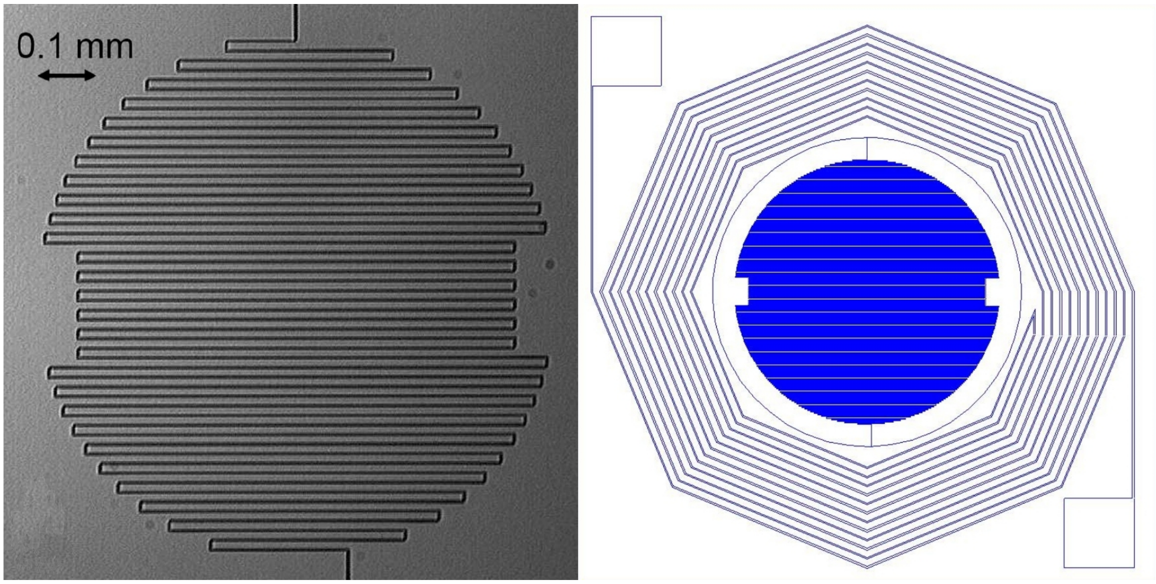

Figure 6.5: Left: Microscope image of manufactured sensor. Light regions are aluminum electrodes. Right: Drawing of a sensor with resistive heater. The capacitive sensor in the center is similar in both designs.

sensor, and can limit ion mobility on the surface of the ice, preventing ions from drifting away from the sensor electrode due to uncompensated transverse electric fields. In order to operate the heater while maintaining the bias voltage, an AC current is used for evaporation, centered on a bias voltage which follows the sensor's DC bias.

To sample the capacitance of the sensor, the LCR bridge uses an AC signal of 40 mVpp at 1 MHz . This is a sufficiently low voltage so as to be negligible compared to DC bias voltages placed on the sensor for attracting or repelling ions. Ion trajectory simulations have also shown that these RF parameters do not interfere with ion capture; the sensors do not form trap-like repulsive RF walls. To read out the sensor, the AC signal is introduced capacitively with a circuit similar to that used to couple RF to the trap electrodes, as seen in Figure 6.7. The signal is coupled through a pair of high-voltage 3.3 nF capacitors, in series with the sensor, which contribute $< 1\%$ to the measured capacitance. 1 MΩ resistors isolate the LCR bridge from a bias voltage introduced by a Trek high-voltage DC amplifier[3]. The supply is capable of amplifying

---

[3] Model 677B

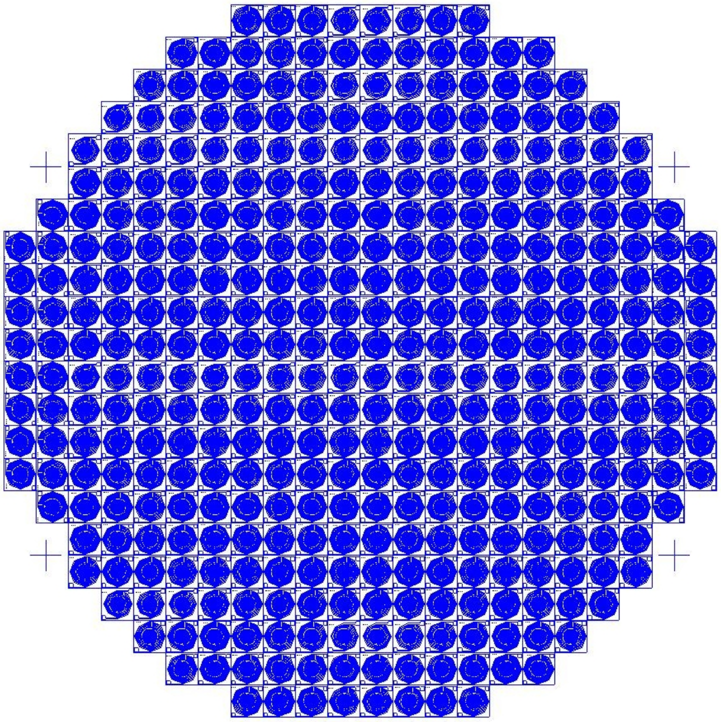

Figure 6.6: A mask for 388 capacative sensors with heaters on a 4-inch quartz wafer.

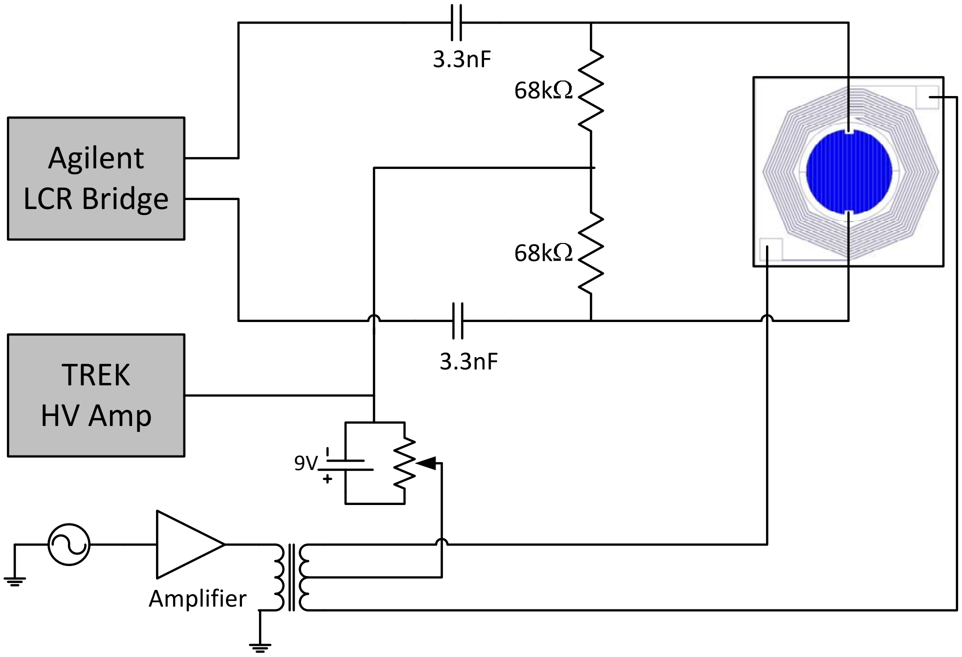

Figure 6.7: Electronics for sensor readout. The LCR bridge samples the sensor through an RC filter, allowing the sensor to be placed at arbitrary DC potential by the Trek HV amplifier. An AC signal is used to heat the resistive loop, which is set at ∼3 V above the sensor by a 9 V battery and potentiometer used to bias the center-tap of a transformer.

a -10V – +10V DAC signal to ±2 kV, with a 15 V/μsec slew rate, $\sim$ 4 times faster than the limit imposed by the 224 μsec RC constant of the isolation circuit.

The sensor is mounted onto a removable copper tip, designed to be screwed onto the cryostat's threaded copper cold finger. Small pieces of Indium enhance the thermal conductivity between the cryostat, tip and sensor. The sensor is held in place, sandwiching the Indium, by cryogenic varnish. A custom-fabricated polyimide-based PC board, mounted on the tip, is used for making electrical connections to the sensor; leads are soldered to the back side of the PC board, while wire-bonds connect the sensor and heater loop to the front. The removable tip allows the sensor to be mounted and wirebonded away from the cryostat, then merely screwed into place so that electrical leads can be soldered. A Lakeshore Silicon diode temperature sensor[4] is mounted to the side of the tip with varnish, and is used to monitor the tip temperature.

6.4 Gas phase ion ejection and recapture

To test the cryogenic probe's viability, it was immovably mounted above the ion trap (as illustrated in Figure 6.8), and attempts were made to load ions onto the probe and release them into the trap.

6.4.1 Probe preparation

Freezing of Xenon onto the probe is performed by cooling the cryostat to $\sim$40 K, and aligning the probe to the trap. The alignment of the probe must be performed when the probe is cold, as the temperature change from room temperature to 40 K causes a significant length change in the cryostat, as well as a deflection in it's axial position. The probe is cooled, then lowered into position above the trap. The distance between the trap and the sensor is limited by the bonding wires protruding from the sensor surface; typically this distance is $\sim$2 mm. Axial alignment is confirmed by imaging the probe with a CCD camera mounted below the trap, with a view along its length.

---

[4] Model DT-471-SD

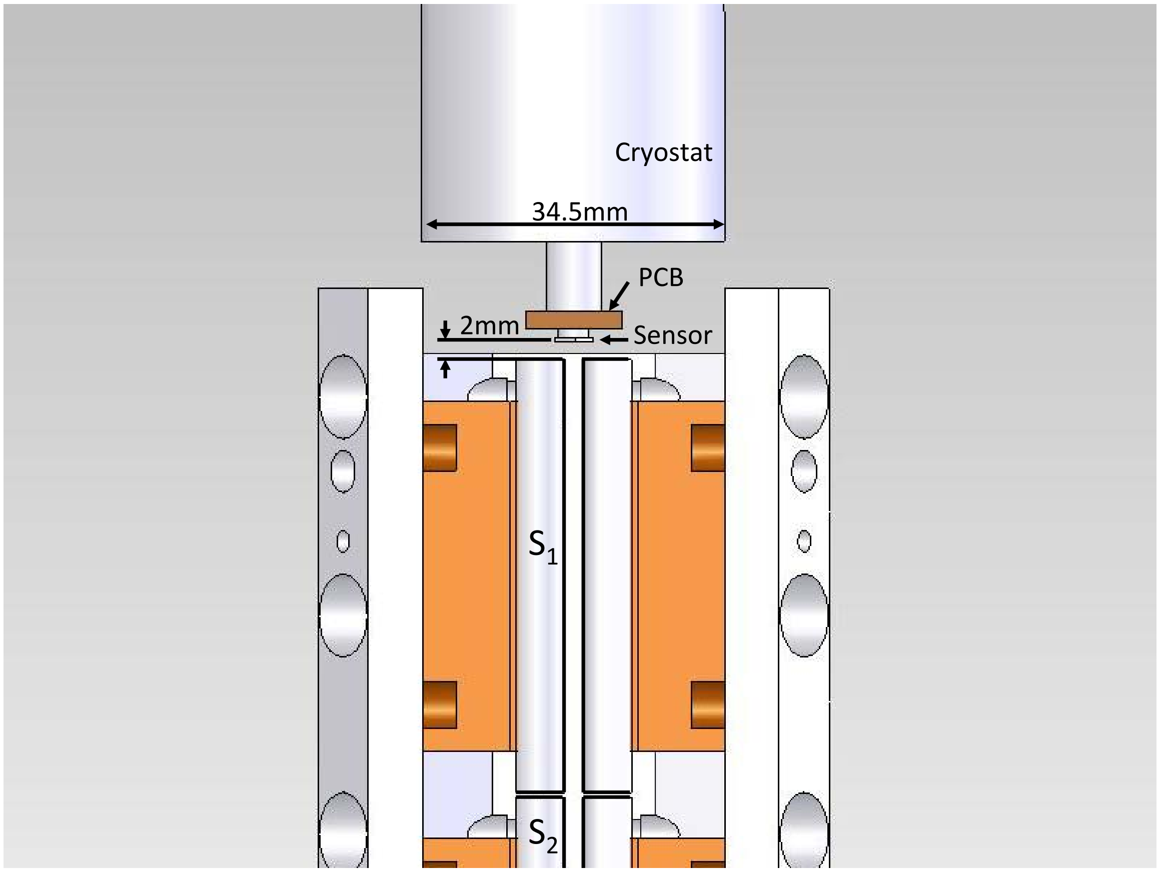

Figure 6.8: Cryogenic probe mounted above the ion trap. The sensor to trap spacing is approximate.

The sensor can be seen through the trap, and the probe is positioned so that the sensor is centered between the electrodes. It is estimated that this procedure aligns the sensor to within 0.5 mm of trap center.

Opening the Xenon gas doser to allow 1×10^{-3} Torr Xenon into the chamber begins the freezing. When the desired ice thickness has been achieved, as indicated by the capacitive sensor, the flow of Xenon into the chamber is halted, and the residual Xenon is pumped out through the 400-lps turbomolecular pump. This freezing must be performed before loading ions into the trap, as the Xenon gas required for freezing would make trapping during this process impossible. Provided the cryostat temperature remains below 50 K, as measured by the temperature sensing diode, the Xenon ice layer will maintain its thickness, in vacuum or Helium, for the 10–15 minute duration of the remainder of the trial.

6.4.2 Ion preparation

Ion clouds were loaded into the trap using the Barium oven and electron gun, in the presence of Helium buffer gas. As the stopping power of the gas, trap acceptance, and resistance to unloading from Xenon gas increase with increasing Helium pressure, trials were performed in 1×10^{-3} Torr Helium, a value at the upper-end of the trap's operating range. Once a cloud of ions is loaded, the electron gun and barium oven are shut down, to allow the neutral Barium vapor in S_2 to dissipate, and to eliminate any effect the electron gun's high voltage may have on ions in transit.

6.4.3 Ion movement

Once an ion cloud is prepared, a negative bias is applied to the probe's sensor (a depiction of the process is shown in Figure 6.9). Bias voltages spanning the range from -1 V to -1 kV are applied. Above 1 kV, the risk of electrical discharge becomes high; such a breakdown will, in most cases, damage the sensor in such a way as to render it inoperable without removal from vacuum for repair. The bias voltage is an experimental parameter which may have a profound effect on the success of ion capture and survival on the probe. As the charge state of the ion must be preserved

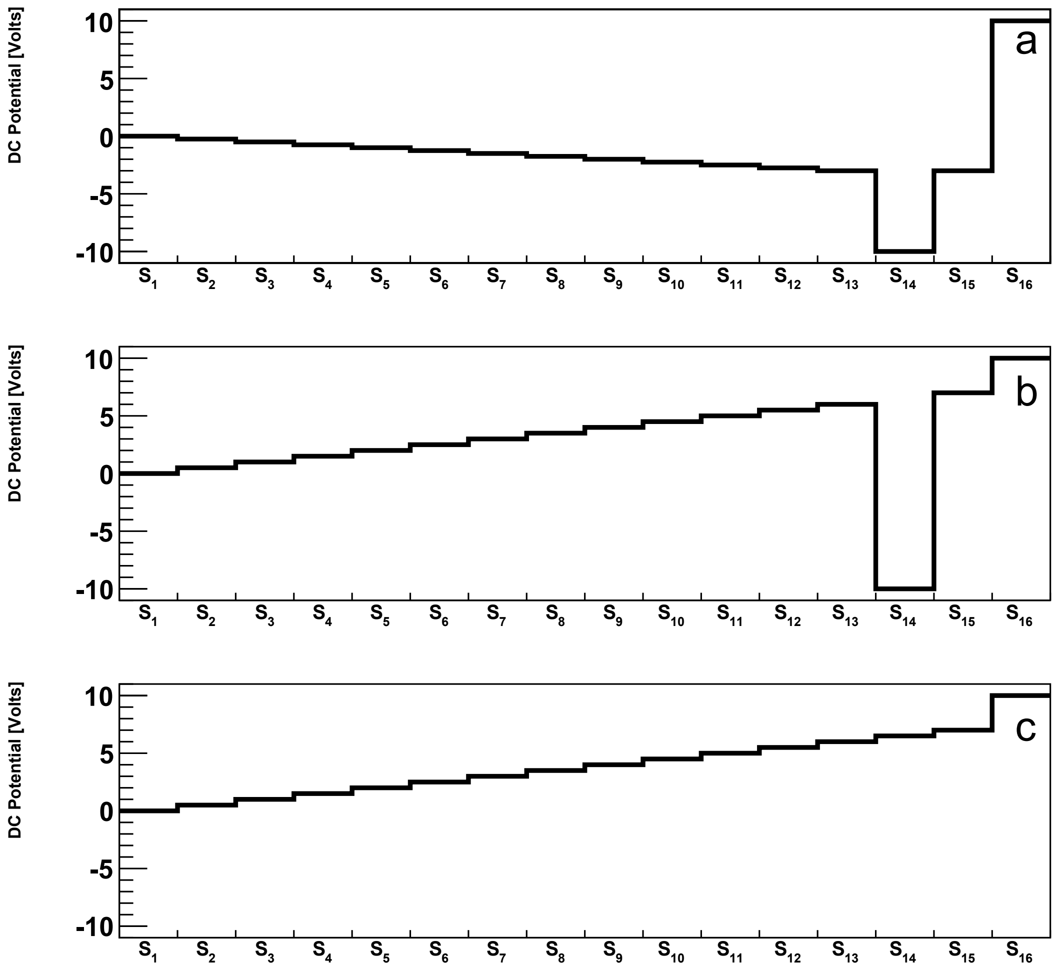

Figure 6.9: The potential configurations used in the ion transfer process. Ions are loaded into the trap in configuration a), moved to the probe through b) and c), then the trap is returned to a) for attempted recapture.

in the process of capturing the ion on the ice, unnecessarily high bias voltages, which may further ionize the Barium, should be avoided. Simultaneously, the mobility of the ion on the surface may necessitate that the ion penetrate the surface of the ice layer in order to remain captured. This would require a minimum attractive bias. Lacking knowledge of which of these processes dominate, and at what range, the entire operating regime must be sampled.

Once the bias is applied to the probe, the DC potentials are adjusted to form a ramp similar to that used to launch ions toward the CEM. The cloud is ejected from the trap, and the DC potentials are reset to the standard loading configuration. To ensure that there are no ions retained in any local minima throughout the trap, the RF trapping potential is zeroed for a moment by disabling and then re-enabling the 2.23 MHz RF signal. Once this has been done, the attractive negative bias on the probe's sensor is reversed, to a small positive repulsive one. As the plots of trap acceptance in Figure 5.6 show, trap acceptance drops dramatically as the kinetic energy of injected ions increases, so a probe bias voltage of over 5 V, giving ions more than 5 eV of kinetic energy, is unlikely to inject ions successfully. At the same time, applying too low of a repulsive voltage may result in failure to eject ions from the probe.

Once the repulsive bias is applied, the ice is evaporated from the sensor by running an AC current through the heater loop. The clearing of the ice is readily seen as a drop in capacitance on the probe's sensor. The operation of the heater does not appreciably affect the temperature reading of the cold finger. The return of ions to the detection region, as evidenced by a fluorescence signal coincident with the Xenon evaporation, would demonstrate the probe's ability to store and inject ions.

6.4.4 Results

The experimental parameters suspected to be most influential to the success of implanting ions on the cryogenic probe and returning them to the trap are the following: probe capture voltage, the voltage applied to attract ions to the probe and implant them in the ice; probe ejection voltage, the potential used to repel ions from the

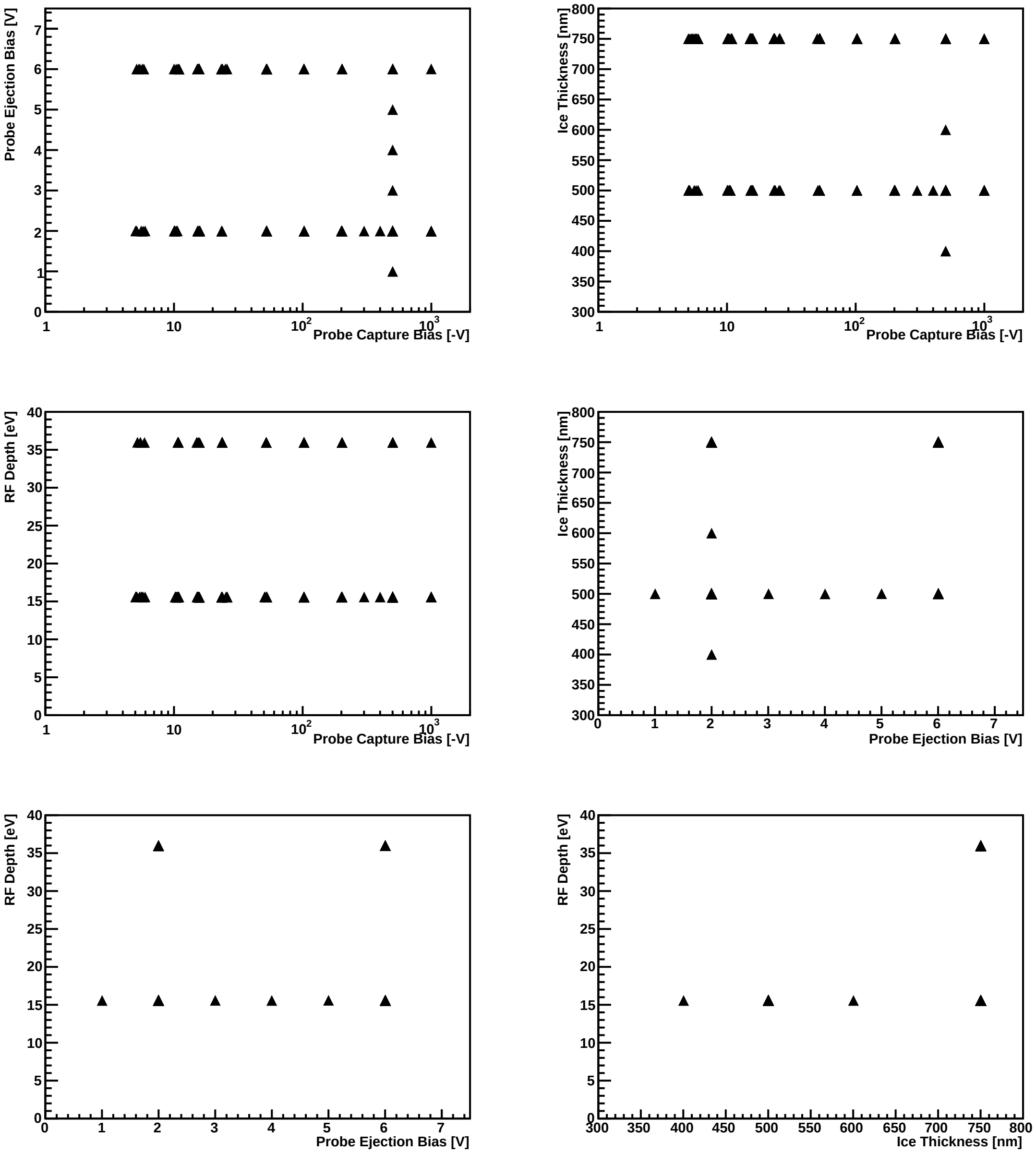

Figure 6.10: Parameter space explored in the course of cryoprobe trials.

tip as the Xenon ice is being evaporated; Xenon ice thickness; and the depth of the RF trapping potential. A summary of the different values sampled in the course of experimental trials of the cryogenic probe is depicted in Figure 6.10. In each trial, an attempt is made to transfer a large cloud (∼50) of ions to the probe and retrieve them. In no trial were any ions recovered. The spectacular failure to recover any ions suggests that for the case of every ion, there is a mechanism by which it is lost, or its charge state is changed. Future experiments in different apparatus may provide information as to the survivability of an ion in/on a solid Xenon substrate. Should they be shown to survive in the singly-charged state for extended periods of time, the failure of the cryoprobe may be best explained by the formation of “snowballs”.

6.5 On snowballs

The work of Wamba et. al demonstrated the reduced mobility of positive radioactive Thorium ions in a liquid Xenon drift cell [61]. This reduced mobility was attributed to the accumulation of Xenon around a positive ion by the attraction of the induced dipole moment of the neutral Xenon. The formation of loosely bound molecular states requires three-body collisions to remove energy from the Ba$^+$/Xe system while the ion/neutral interatomic separation is in the range where the interaction potential is negative. This could occur in liquid and solid phases, and high-pressure gas systems where average separations are small. It is suspected that the formation of heavy “snowballs” of polarized Xenon atoms bound to the Barium ions could be responsible for failure to retrieve Barium ions from the cryogenic probe, due to an inability to confine these snowballs in the trap, insensitivity of the snowballs to the spectroscopy lasers, or both.

The Ba$^+$/Xe interaction potential was introduced in Chapter 3 and is reproduced in Figure 6.11. A Barium ion should capture a polarized Xenon atom if the atom is brought to rest at a distance from the Xenon where the interaction potential is less than the thermal energy of the surroundings. At 170 K, $kT = 0.015$ eV, and atoms should remain captured out to an internuclear spacing of 7.5 Å. Measurements of Barium ion mobilities in liquid Xenon have observed this clustering of neutral Xenon

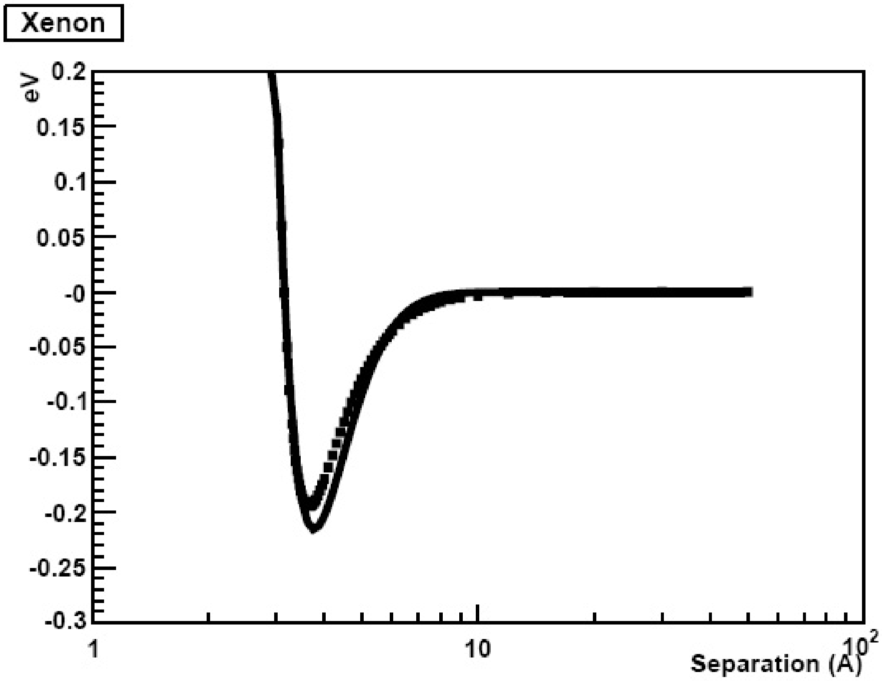

Figure 6.11: The Ba^+/Xe interaction potential.

around Barium ions, with an effective radius of 8.6Å, which nicely corresponds to the the 7.5 Å nuclear spacing, plus the 1.1Å atomic radius of Xenon [62]. An 8.6 Å radius cluster would populate a spherical shell of volume 2600 Å^3 with solid Xenon at a density of 3.4 g/cm^3, giving the cluster a mass of 5500 amu, the equivalent of 42 bound Xenon atoms. At 300 K, one would expect atoms to remain captured to a radius of 6.6 Å, causing cluster radii to be limited to 7.7 Å, with a mass of ∼3900 amu.

The stability diagram of Figure 3.2 describes the ranges of trap parameters for which isolated ions will be stably confined. As both q and a (the x- and y-axes of Figure 3.2) are inversely proportional to ion mass, changing the ion mass without changing trap parameters rescales the stability diagram, or, equivalently, different masses have q and a values lying on a line passing through the origin. For a trap that is operated at $q = 0.2$ and $a = 0$ for a mass-138 ion, any ion with mass m_{ion} heavier than 138 will also theoretically be confined, with $q = 0.2 \times (138/m_{ion})$. The trap depth, however, is also inversely proportional to ion mass. According to Equation 5.1, the ion trap, operating with 200 V_{RF} at 2.23 MHz, has a depth of 2 eV for single Barium ions, and so a 3900-amu cluster is confined in a trap with a depth of only 70 meV. Additionally, the light Helium gas has little stopping power for ions that are 1000 times heaver than Helium. Simulation of trap acceptance for 3900-amu ions in the presence of 1×10^{-3} Torr Helium gas shows a drastic reduction in the likelihood of ion capture. Figure 6.12 shows the acceptance for ions emitted into the trap with energies between 0–1 eV, as simulated in SIMION8. Only 1% of heavy ions emitted at low radius ($r <$ 1mm) in this energy range are captured. Heavy ions emitted with energies above 1 eV were not captured.

It has been suggested that illumination of the snowballs by a 405-nm diode laser could potentially dissociate the loosely-bound molecules. The 405-nm laser light could potentially drive the Ba^+ ion's 455-nm S–P transition, with the excess 1.12 eV of the absorbed photon's energy being transferred to vibrational motion of the molecule, perhaps breaking it apart. This was attempted by co-propagating a 300-μW 405nm laser with the spectroscopy lasers, in each trial of Figure 6.10, and was not successful.

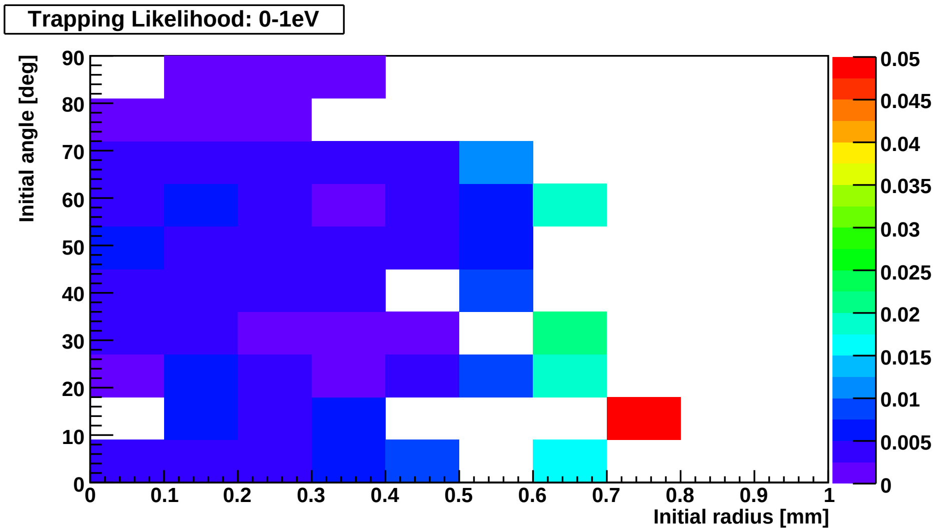

Figure 6.12: The simulated trap acceptance for 3900-amu ions emitted with energies between 0–1 eV. The acceptance is vastly reduced at all initial locations and initial directions for ions of this mass.

Chapter 7

Future directions

The inability of the cryogenic probe to return ions to the linear trap is not the end of the story for Barium tagging for the EXO experiment. The question of the nature of the failure remains to be answered, and if a conclusion can be reached, then perhaps a re-design will render the cryogenic probe fit for Barium ion extraction and tagging. In the meantime, alternate probe technologies are being developed, and may prove successful where the cryogenic probe has not. One such technology is based on the resonant ionization of neutral Barium atoms, which shall be discussed in §7.2. Finally, if a prototype ion probe is capable of capturing Barium ions from an ion trap and returning them, then a mechanism must be constructed to demonstrate the entire process, from extraction from a liquid Xenon cell to detection in a linear trap. A robotic probe mover has been designed for this purpose.

7.1 Radioactive ion implantation

A direct measurement of the survivability of Barium ions in solid Xenon would provide useful information for the future of a cryogenically-based ion extraction probe. Implanting radioactive Barium atoms into Xenon ice and tracking their locations through the processes of attraction and repulsion during evaporation could yield for the first time a measure of the lifetime of the Barium charge states.

The ATLAS accelerator facility with CARIBU at Argonne National Laboratory

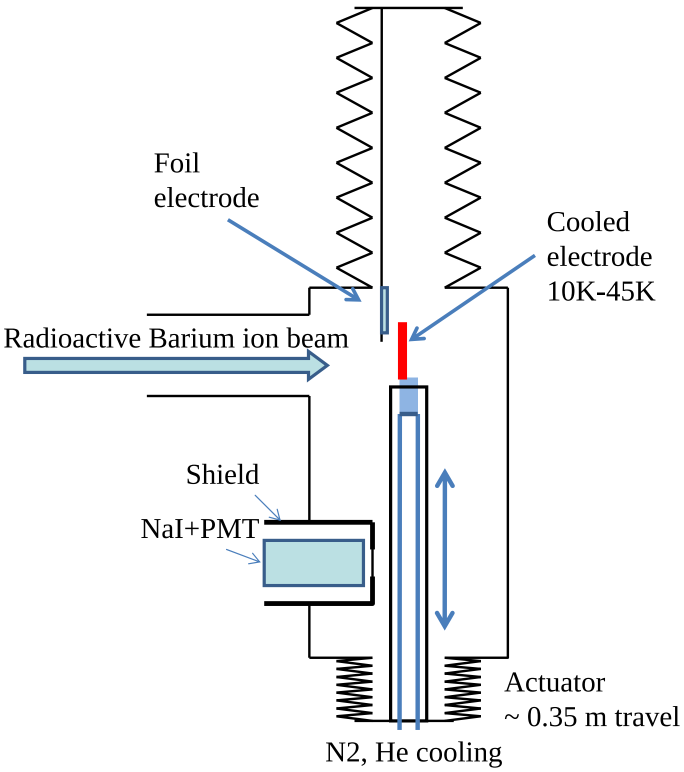

Figure 7.1: Apparatus for testing Barium ion survivability in solid Xenon with a radioactive Barium ion beam.

is capable of producing a variety of neutron-rich isotopes with high intensities and tunable energies spanning the range from MeV down to a few electron-volts. Among these is ^{139}Ba, a β-emitter with an 83-minute half life, in which 24% of the β-decays are immediately followed by a 165-keV γ-ray. ATLAS is capable of delivering 3×10^5 ^{139}Ba ions per second [63].

An apparatus similar to that shown in Figure 7.1 would be capable of manipulating delivered radioactive ions. The capacitive sensor described in §6.3.2 is attached to a cryostat mounted on a linear actuator. Xenon ice is frozen on the sensor, which is then exposed to the radioactive ion beam, collecting ions in the ice. The cryostat can then be lowered into view of a radiation detector, to confirm the activity of the

Barium-loaded Xenon ice. The cryostat is then returned to its original position, and a foil electrode mounted to its own linear actuator is placed in close proximity to the cold electrode. The foil electrode can then be arbitrarily biased with respect to the cold electrode, and then either electrode can be counted by the radiation detector. By varying the cryostat temperature, electrical bias voltages and timings, the stability of the ion state can be determined in solid Xenon, as well as any dependence the ion lifetime may have on Xenon temperature. This experiment has been devised and is being developed by EXO collaborators at the Technical University of Munich.

7.2 Resonant ionization of Barium

While the cryogenic probe was the first for which operation with a linear trap was attempted, it is not the only concept that has been in development. A second technology, based on the resonant ionization spectroscopy (RIS) of Barium, has been rapidly approaching maturity in parallel. The RIS probe circumvents the problem of maintaining the Barium charge state in the process of transport by re-ionizing upon ejection from the probe.

Once inserted into a Xenon volume, the probe will attract ions to a conductive electrode, where it will be captured, and neutralized. Once the atom is bound to the surface, it can be transported along with the probe to a trap for re-emission. With the probe in position, the electrode is illuminated with a series of laser pulses intended to desorb and then re-ionize the neutral Barium atom, so that it can be captured and confined in the trap for fluorescent spectroscopic identification (though the RIS may ultimately prove selective enough for identification without fluorescence spectroscopy). An infrared laser pulse from a 1064-nm Nd:YAG is used to locally heat the electrode to cause the evaporation of the Barium from the surface. Once liberated, the atom is exposed to pulses from a pair of lasers tuned to specific transitions in Barium, to excite the atom to first an intermediate and then an auto-ionizing state, reionizing the atom for capture. The specific transitions are shown in Figure 7.2. Neither the 553.5-nm nor the 389.7-nm photons possess enough energy to ionize an atom on their own, so only atoms with an intermediate state that can be

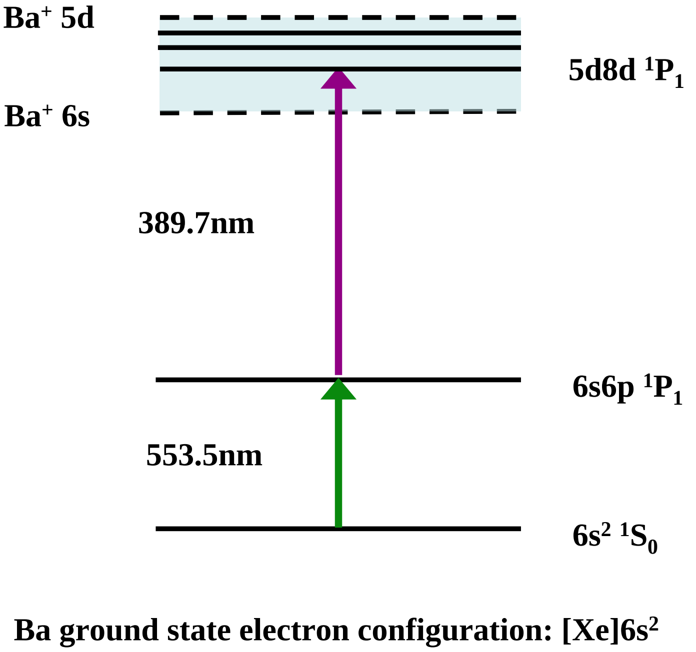

Figure 7.2: Energy levels of the Ba-I neutral atom. Excitation by 553.5-nm and 389.7-nm light can leave the atom in an auto-ionizing state.

accessed by a 553.5-nm or 389.7-nm excitation wavelength can be ionized, so while the evaporation pulse may release more free atoms than just the neutral Barium intended, the ionization pulses will only ionize Barium. While initial work has involved an opaque electrode illuminated by an external laser, a design variant under consideration involves coating an optical fiber with a semi-transparent conductive coating, and illuminating the electrode and released atoms with pulses transported through the fiber.

Desorption and subsequent resonant ionization from a doped Silicon electrode have been experimentally demonstrated and will be detailed in a future publication, and attempts to transport ions back and forth between an electrode and the linear trap through RIS will be undertaken in the near future.

7.3 A robotic probe mover

To demonstrate a candidate probe technology's viability for extracting Barium ions from a liquid Xenon TPC, and measure an efficiency for the transfer process, a robotic ion extraction probe mover is has been designed. The probe mover, shown in Figure 7.3, is designed to couple the existing vacuum chamber with second-generation linear trap to a cryogenic liquid Xenon cell. The robotic mover is able to position a probe with two degrees of freedom: linear insertion and extraction of the probe along its axis, and an angular rotation of the probe about a central hinge, allowing the probe's axis to be aligned either co-linear with the trap's axis, or with the inlet of the Xenon cell. This motion must be done entirely in a UHV compatible environment. The linear motion is driven by a servo motor and acme drive screw, with sufficient torque to expand a 2.75-inch edge-welded conflat bellows, the flexible vacuum element through which motion is accomplished, while under vacuum. The angular motion is driven by a pair of double-acting pneumatic actuators, rotating the probe assembly about a pivot point located at the intersection of the axis of the trap and the cryogenic cell access tube. Figure 7.3 shows a sectioned view of the hinge structure. An 8-inch edge-welded bellows accommodates the rotation by flexing with the hinge, automotive shock absorbers dampen the rotational motion, and expansion

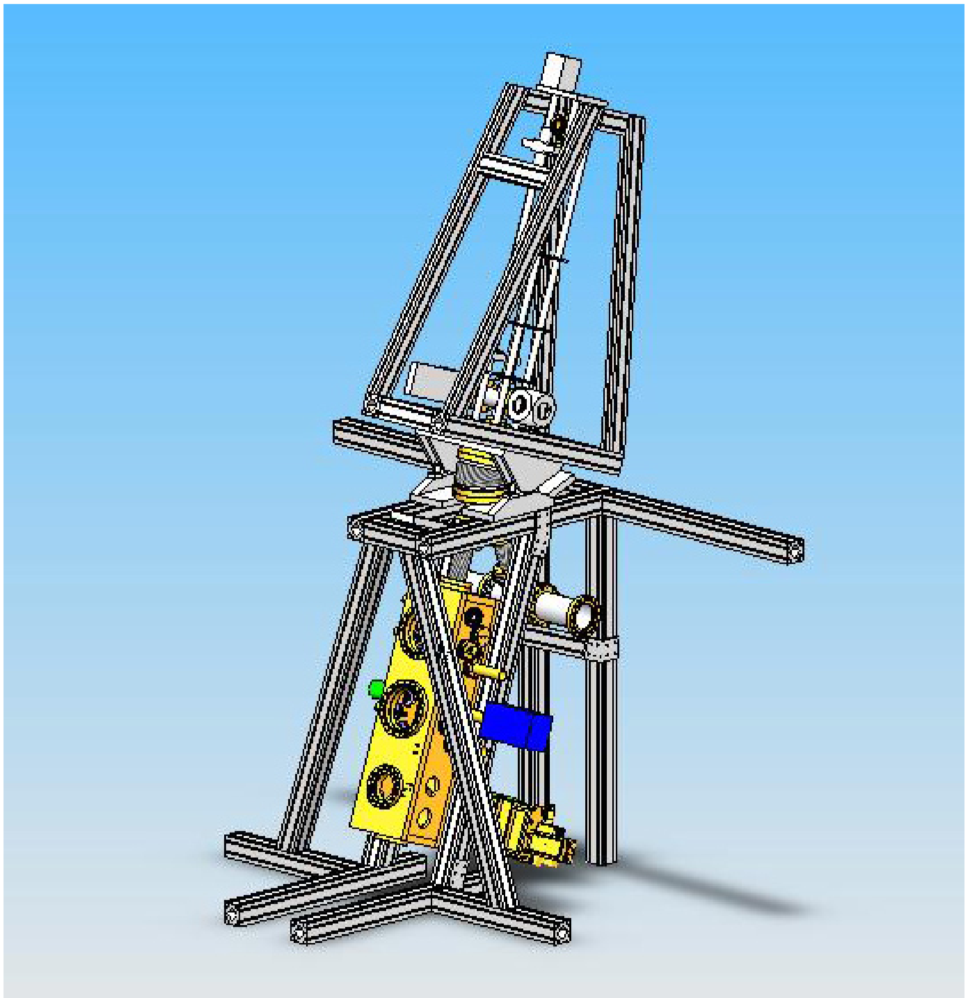

Figure 7.3: A robotic fixture for ion probe manipulation, coupling the existing ion trap and vacuum chamber to a liquid Xenon cell.

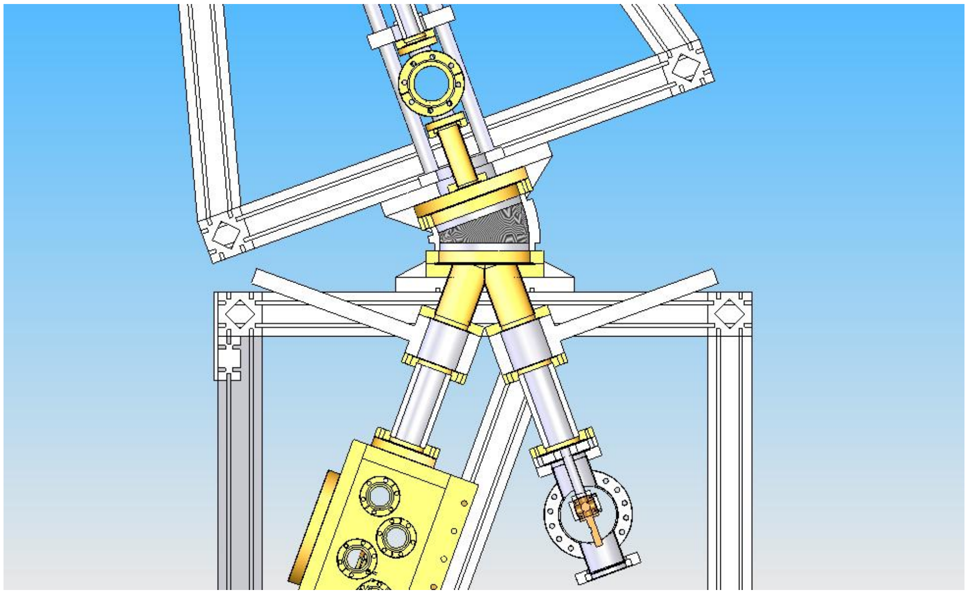

Figure 7.4: Cross-section view of probe mover hinge.

springs ensure that the stable position of the probe is vertical.

The gas handling and vacuum systems of the probe mover are illustrated in Figure 7.5. When full of liquid, the Xenon cell will contain a 1-atm Xenon vapor. As the presence of this Xenon gas in the linear trap chamber would prohibit the trapping of ions, the probe must be moved through a load-lock system. All-metal gate valves isolate the Xenon cell and trapping chamber from each other, with an intermediate volume separating the two. Once an ion in the liquid is captured to the probe, the probe is retracted into the intermediate volume, and a gate valve is closed behind it, isolating the Xenon cell. The intermediate volume is then rapidly pumped to vacuum through a 10-lps dry-scroll, and then by a 70-lps turbo once roughing vacuum has been reached. When the Xenon pressure in the intermediate volume has been reduced to 10^{-7} Torr or below, the gate valve separating the trap chamber from the intermediate volume can be opened, bringing the intermediate volume with Helium from the trapping chamber. The probe can then be inserted into the trap chamber, and release of the ion can be attempted.

The system is designed to allow the entire transfer process to be performed in less than 60 seconds, to minimize losses from the probe, and allow the procedure to be

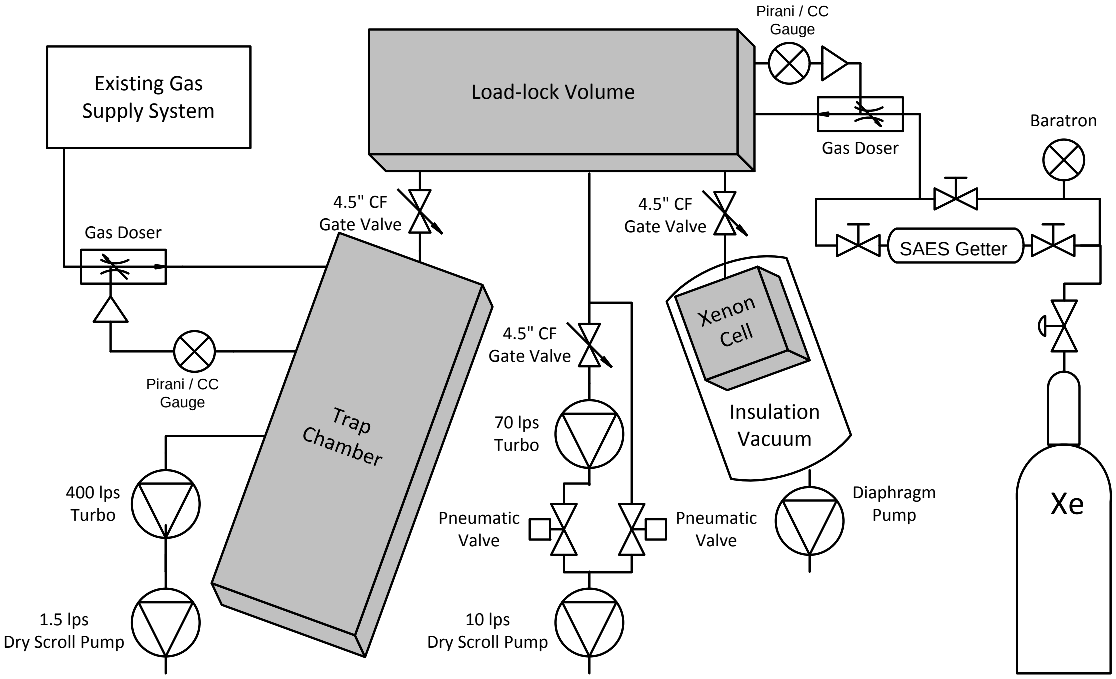

Figure 7.5: Vacuum and gas system design for the ion probe manipulator.

repeated rapidly. It is also intended to accommodate a variety of probe technologies; a cryogenic probe with a flexible Helium transfer line, an RIS probe, or a surface ionization probe could all be compatible with this mechanism, which will serve as their final test of suitability for EXO.

Bibliography

[1] W. M. Yao *et al.*, Journal of Physics G: Nuclear and Particle Physics **33**, 1 (2006).

[2] C. Arnaboldi *et al.*, Phys. Rev. C **78**, 035502 (2008).

[3] S. Elliot and P. Vogel, Annu. Rev. Nucl. Part. Sci. **52**, 11551 (2002).

[4] H. V. Klapdor-Kleingrothaus *et al.*, Modern Physics Letters A **16**, 2409 (2001).

[5] J. Z. Klose, J. R. Fuhr, and W. L. Wiese, Journal of Physical and Chemical Reference Data **31**, 217 (2002).

[6] J. Wodin, *Single ion trapping in a buffer gas and liquid Xe energy resolution studies for the EXO experiment*, PhD thesis, Stanford University, 2007.

[7] F. T. Avignone, S. R. Elliott, and J. Engel, Rev. Mod. Phys. **80**, 481 (2008).

[8] E. Conti *et al.*, Phys. Rev. B **68**, 054201 (2003).

[9] M. F. McGuirk *et al.*, The Journal of Chemical Physics **130**, 194305 (2009).

[10] M. Green *et al.*, Phys. Rev. A **76**, 023404 (2007).

[11] P. Fierlinger *et al.*, Review of Scientific Instruments **79**, 045101 (2008).

[12] Y. Fukuda *et al.*, Phys. Rev. Lett. **81**, 1562 (1998).

[13] Super-Kamiokande Collaboration, Y. Ashie *et al.*, Phys. Rev. Lett. **93**, 101801 (2004).

[14] B. T. Cleveland *et al.*, The Astrophysical Journal **496**, 505 (1998).

[15] SNO Collaboration, S. N. Ahmed *et al.*, Phys. Rev. Lett. **92**, 181301 (2004).

[16] K. Eguchi *et al.*, Phys. Rev. Lett. **90**, 021802 (2003).

[17] MINOS Collaboration, D. G. Michael *et al.*, Physical Review Letters **97**, 191801 (2006).

[18] T. Schwetz, M. Trtola, and J. W. F. Valle, New Journal of Physics **10**, 113011 (2008).

[19] E. W. Otten and C. Weinheimer, Reports on Progress in Physics **71**, 086201 (2008).

[20] U. Seljak, A. Slosar, and P. McDonald, Journal of Cosmology and Astroparticle Physics **2006**, 014 (2006).

[21] B. Kayser, Neutrino mass, mixing, and flavor change, in *Neutrino Mass*, edited by G. Altarelli and K. Winter, chap. 1, pp. 1–24, Springer, 2003.

[22] M. Moe, Nucl. Phys. B. (Proc. Suppl.) **19** (1991).

[23] M. Danilov *et al.*, Physics Letters B **480**, 12 (2000).

[24] R. N. Mohapatra and G. Senjanović, Phys. Rev. Lett. **44**, 912 (1980).

[25] M. Gell-Mann, P. Ramond, and R. Slansky, in *Supergravity*, edited by P. van Nieuwenhuizen and D. Freedman, 1979.

[26] D. H. Perkins, *Introduction to High Energy Physics* (Cambridge University Press, 2000).

[27] M. Doi, T. Kotani, and E. Takasugi, Progress of Theoretical Physics Supplement **83**, 1 (1985).

[28] E. Caurier, J. Menéndez, F. Nowacki, and A. Poves, Phys. Rev. Lett. **100**, 052503 (2008).

[29] C. E. Aalseth *et al.*, Mod. Phys. Lett., A **44**, 1475 (2002).

[30] H. V. Klapdor-Kleingrothaus *et al.*, Physics Letters B **586**, 198 (2004).

[31] R. Neilson *et al.*, Nuclear Instruments and Methods in Physics Research Section A: Accelerators, Spectrometers, Detectors and Associated Equipment **608**, 68 (2009).

[32] D. Leonard *et al.*, Nuclear Instruments and Methods in Physics Research Section A: Accelerators, Spectrometers, Detectors and Associated Equipment **591**, 490 (2008).

[33] R. Wuerker, H. Shelton, and R. Langmuir, J. App. Phys. **30**, 342 (1959).

[34] H. Dehmelt, Radiofrequency spectroscopy of stored ions i: Storage, Vol. 3, Advances in Atomic and Molecular Physics, pp. 53 – 72, Academic Press, 1968.

[35] W. Paul, Rev. Mod. Phys. **62**, 531 (1990).

[36] F. G. Major, V. N. Gheorghe, and G. Werth, *Charged Particle Traps* (Springer, 2005).

[37] L. Landau and E. Lifshitz, *Mechanics* (Pergamon Press, 1960).

[38] SIMION 8.0, Scientific Instruments Inc.

[39] P. Langevin, Ann. Chim. et Phys. **5** (1905).

[40] R. E. Johnson, *Introduction to Atomic and Molecular Collisions* (Plenum Press, 1982).

[41] T. Kim, *Buffer gas cooling of ions in a radiofrequency quadrupole ion gude: A study of the cooling process and cooled beam properties*, PhD thesis, McGill University, 1997.

[42] E. W. Weisstein, Triangular distribution, from mathworld – a wolfram web resource. `http://mathworld.wolfram.com/TriangularDistribution.html`.

[43] B. P. Roe, *Probability and Statistics in Experimental Physics* (Springer, 2001).

[44] F. Herfurth *et al.*, Nuclear Instruments and Methods in Physics Research Section A: Accelerators, Spectrometers, Detectors and Associated Equipment **469**, 254 (2001).

[45] A. Kellerbauer, T. Kim, R. B. Moore, and P. Varfalvy, Nuclear Instruments and Methods in Physics Research Section A: Accelerators, Spectrometers, Detectors and Associated Equipment **469**, 276 (2001).

[46] L. Landau and E. Lifshitz, *Statistical Physics* (Pergamon Press, 1958).

[47] F. G. Major and H. G. Dehmelt, Phys. Rev. **170**, 91 (1968).

[48] Y. Moriwaki, M. Tachikawa, Y. Maeno, and T. Shimizu, Japanese Journal of Applied Physics **31**, L1640 (1992).

[49] R. G. DeVoe, Phys. Rev. Lett. **102**, 063001 (2009).

[50] S. Waldman, *Single ion trapping for the Enriched Xenon Observatory*, PhD thesis, Stanford University, 2005.

[51] Y. Moriwaki, M. Tachikawa, and T. Shimizu, Japanese Journal of Applied Physics **35**, 757 (1996).

[52] R. Schneider and G. Werth, Zeitschrift fr Physik A Hadrons and Nuclei **293**, 103 (1979).

[53] H. Metcalf and P. van der Straten, *Laser Cooling and Trapping* (Springer, 1999).

[54] G. Janik, W. Nagourney, and H. Dehmelt, J. Opt. Soc. Am. B **2**, 1251 (1985).

[55] W. M. Itano and D. J. Wineland, Phys. Rev. A **25**, 35 (1982).

[56] B. Flatt *et al.*, Nuclear Instruments and Methods in Physics Research Section A: Accelerators, Spectrometers, Detectors and Associated Equipment **578**, 399 (2007).

[57] T. Koerber, *Measurement of light shift ratios with a single trapped* $^{138}Ba^{+}$ *ion, and prospects for a parity violation experiment*, PhD thesis, University of Washington, 2003.

[58] M. S. Robbins and B. J. Hadwen, IEEE Transactions on Electron Devices **50**, 1227 (2003).

[59] S. A. Fields, J. L. Burch, and W. A. Oran, Review of Scientific Instruments **48**, 1076 (1977).

[60] E. Kennard, *Kinetic Theory of Gases* (McGraw-Hill, 1938).

[61] K. Wamba *et al.*, Nuclear Instruments and Methods in Physics Research Section A: Accelerators, Spectrometers, Detectors and Associated Equipment **555**, 205 (2005).

[62] S. C. Jeng, W. M. Fairbank Jr., and M. Miyajima, Journal of Physics D: Applied Physics **42**, 035302 (2009).

[63] G. Savard, personal communication, 2010.